UNIVERSITAT ROVIRA I VIRGILI

NUMERICAL AND EXPERIMENTAL STUDY OF STEADY AND UNSTEADY MIXED CONVECTION FLOW IN A CUBICAL OPEN CAVITY WITH THE BOTTOM WALL HEATED

Gorg Abdelmassih Bassit Megalaa

ADVERTIMENT. L'accés als continguts d'aquesta tesi doctoral i la seva utilització ha de respectar els drets de la persona autora. Pot ser utilitzada per a consulta o estudi personal, així com en activitats o materials d'investigació i docència en els termes establerts a l'art. 32 del Text Refós de la Llei de Propietat Intel·lectual (RDL 1/1996). Per altres utilitzacions es requereix l'autorització prèvia i expressa de la persona autora. En qualsevol cas, en la utilització dels seus continguts caldrà indicar de forma clara el nom i cognoms de la persona autora i el títol de la tesi doctoral. No s'autoritza la seva reproducció o altres formes d'explotació efectuades amb finalitats de lucre ni la seva comunicació pública des d'un lloc aliè al servei TDX. Tampoc s'autoritza la presentació del seu contingut en una finestra o marc aliè a TDX (framing). Aquesta reserva de drets afecta tant als continguts de la tesi com als seus resums i índexs.

ADVERTENCIA. El acceso a los contenidos de esta tesis doctoral y su utilización debe respetar los derechos de la persona autora. Puede ser utilizada para consulta o estudio personal, así como en actividades o materiales de investigación y docencia en los términos establecidos en el art. 32 del Texto Refundido de la Ley de Propiedad Intelectual (RDL 1/1996). Para otros usos se requiere la autorización previa y expresa de la persona autora. En cualquier caso, en la utilización de sus contenidos se deberá indicar de forma clara el nombre y apellidos de la persona autora y el título de la tesis doctoral. No se autoriza su reproducción u otras formas de explotación efectuadas con fines lucrativos ni su comunicación pública desde un sitio ajeno al servicio TDR. Tampoco se autoriza la presentación de su contenido en una ventana o marco ajeno a TDR (framing). Esta reserva de derechos afecta tanto al contenido de la tesis como a sus resúmenes e índices.

WARNING. Access to the contents of this doctoral thesis and its use must respect the rights of the author. It can be used for reference or private study, as well as research and learning activities or materials in the terms established by the 32nd article of the Spanish Consolidated Copyright Act (RDL 1/1996). Express and previous authorization of the author is required for any other uses. In any case, when using its content, full name of the author and title of the thesis must be clearly indicated. Reproduction or other forms of for profit use or public communication from outside TDX service is not allowed. Presentation of its content in a window or frame external to TDX (framing) is not authorized either. These rights affect both the content of the thesis and its abstracts and indexes.

Gorg Abdelmassih Bassit Megalaa

NUMERICAL AND EXPERIMENTAL STUDY OF STEADY AND UNSTEADY MIXED CONVECTION FLOW IN A CUBICAL OPEN CAVITY WITH THE BOTTOM WALL HEATED

DOCTORAL THESIS

Supervised by

Dr. Anton Vernet

Dr. Jordi Pallares

Department of Mechanical Engineering

UNIVERSITAT ROVIRA i VIRGILI

Tarragona

2016

UNIVERSITAT
ROVIRA i VIRGILI
Department of Mechanical Engineering
Escola Tècnica Superior d'Enginyeria Química (ETSEQ)
Av. Països Catalans, 26, 43007 Tarragona, Spain

Dr. Anton Vernet and Dr. Jordi Pallares, Professors at the Department of Mechanical Engineering of Universitat Rovira i Virgili,

CERTIFY:

That the present study, entitled:

Numerical and Experimental Study of Steady and Unsteady Mixed Convection Flow in a Cubical Open Cavity with the Bottom Wall Heated

Presented by Mr. *Gorg Abdelmassih Bassit Megalaa* for the award of the degree of Doctor has been developed under our supervision at the Department of Mechanical Engineering of this university, and it is fully adequate in scope and quality as a dissertation for the degree of Doctor of Philosophy.

And, to inform you of that and in order for it to have the needed effects, we sign this certification.

Tarragona, June 2016

Dr. Anton Vernet

Dr. Jordi Pallares

"So neither he who plants nor he who waters is anything, but only God who gives the growth"

(1st, Corinthians 3:7)

I dedicate this work to my family, who offered me unconditional love and support, and have always been there for me. Thank you so much

Contents

Acknowledgements

This thesis concludes more than six years of work at ECOMMFIT laboratories (Computation and Modelization in Fluid Mechanics and Turbulence), in the department of Mechanical Engineering, Universitat Rovira i Virgili, Spain.

God is able to overcome the impossible, without God’s hand and his care; I would never have been able to do the work I did.

Without the help of many other people, it would have been impossible to finish all the work presented in this thesis. First, I would like to acknowledge my supervisors Dr. Anton Vernet and Dr. Jordi Pallares for their guidance, support and for their valuable comments. Without their knowledge, experience and help I would have been totally lost.

I am also grateful to Dra. Sylvana Varela, Sr. José Rodríguez and Sr. Vicenç Puig, for the technical support in the laboratory. I also have to thank all the mechanical engineering staff who supported me during that time.

I would also like to thank all the PhD students of the ECOMMFIT group for shearing me not only the office but also the knowledge, and for helping me in virtually everything. Last but not least, I would like to thank all the people who gave me the moral support I needed. The people who told me I could do it when I doubted. I think that help was the most important for me.

This work was supported financially by a pre-doctoral grant from Universitat Rovira i Virgili.

Tarragona, 2016

Abstract

During the last decades, considerable efforts have been devoted to study the flow structure and the heat transfer that occurs in flow over open cavities due to their importance in various engineering applications in different scales. The small scale of this geometry is applied in cooling of electronic component, while the medium scale can be found in solar collector with wind barriers. An excessive number of applications are embodied in large scales such as: harbor entrance, landing gear bays, bomb bay, canyon street, water deposit of firefighter airplanes ...etc. Beside all these applications, the main reason of making this geometry a point of interest is that this geometry is often used in the simplest isothermal configuration to validate the computational model and numerical codes.

A comprehensive three-dimensional numerical simulation and experimental studies for both laminar steady and unsteady regimes have been carried out for the mixed convective flow over a three-dimensional cubical open cavity. The cavity is heated from below at constant temperature while the other walls are adiabatic. The numerical simulation has been done using a three-dimensional incompressible finite volume flow parallel solver (3DINAMICS). The code solves numerically the three-dimensional incompressible Navier Stokes Equations, with Boussinesq approximation for the density, on non-uniform staggered Cartesian meshes. The effects of the buoyancy forces are acting perpendicular to the mainstream flow. The effects of the mixed convection over the steadiness, velocities and temperature distribution were obtained.

Air flow and water flow were studied. Uniform velocity u_0 and constant temperature T_0 were applied in the inflow conditions. It was studied for Reynolds numbers ($100 \leq Re \leq 1500$)

and Richardson number ($10^{-3} \leq Ri \leq 10^{1}$). Prandtl number is set to ($Pr=0.7$) for air flow, and ($Pr=7$) for water flow.

The effects of the temperature dependent physical properties of the water have been studied for this range or Reynolds and Richardson numbers. It was found that, the use of non-Boussinesq approximation does not affect the flow topology.

The phenomenological description of the mixed convection inside and outside the cavity and the combined effects of the natural and forced convection have been obtained. The phenomenological study shows the existence of a primary recirculation cell structure inside the cavity in all the cases that is similar to the flow structures found in a lid driven cavity. For the mixed convection, it has been found that the effect of the buoyancy is very weak and not important for low Richardson numbers at $Ri \leq 0.01$ for all $Re \leq 1500$, while at $Ri \geq 1$ the effect of the buoyancy is important.

For small Richardson cases ($Ri<1$) the flow inside the cavity is laminar and steady. It consists in a single roll that exhibits larger velocities as the Richardson number is increased. For both high Reynolds number and Richardson number ($Ri \geq 10$) the flow becomes unsteady with a complex three-dimensional nature. The natural convection strongly participate in the mixed convection since the effects of the buoyancy force is strong and almost leads the transport mechanism.

The time evolution of the unsteady flow structures was studied. An unsteady periodic flow is found at $Re=100$ and $Ri=10$. Alternate flow ejections from the cavity to the channel occur near the lateral walls while the flow enters the cavity from the channel through the central part of the cavity. A conditional sampling technique has been used to elucidate the evolution of the mean unsteady turbulent flow structures at $Ri=10$. It has been found that the alternate flow ejections persist for all the Reynolds analyzed.

The computed Nusselt numbers in the present three-dimensional setup are in general agreement with a previously reported correlation, valid for two-dimensional cavities of different aspects ratios.

Particle Image Velocimetry technique (PIV) has been used to achieve an experimental study. The PIV technique is able to obtain the instantaneous complex flow structures in a wide range of flow scales. However, the open cavity configuration is a challenge for the PIV technique since it extends the required velocity range, as the peak velocity of the recirculating flow in the cavity is a several times lower than the flow velocity in the channel. The velocity and the flow structures obtained by the numerical simulation were compared with the experimental results. Good agreement was realized between the experimental and simulation results.

The ranges of Reynolds and Richardson numbers considered ($100 \leq Re \leq 1500$ and $0.1 \leq Ri \leq 10$) correspond to the usual operating conditions of some processes associated with the cooling of electronic components. The effect of Ri on the flow stability, the analysis of the flow topology and the time evolution, when the flow is unsteady, are the main parts of this work. The experimental measurements allowed the confirmation of the numerical results.

The main objectives of this thesis are:

- Analyze mixed convection effects on the flow over a three-dimensional cubical open cavity with bottom wall heated by uniform temperature, while the other walls are adiabatic.
- Achieve an experimental study by using the PIV technique in order to calibrate the numerical results.
- Obtain and analyze the characteristics and time evolution of the flow structures present in the unsteady cases.

List of publications and conferences

Journal publications

[1] Abdelmassih G., A. Vernet, Pallares J. (2016); Steady and unsteady mixed convection flow in a cubical open cavity with the bottom wall heated. *Int. J. Heat Mass Transfer*. Volume 101, October 2016, Pages 682–691. **ISI-JCR, Impact Factor: 2.857 (Q1).**

DOI:10.1016/j.ijheatmasstransfer.2016.05.074.

[2] Abdelmassih G., Vernet A., Pallares J. (2012); Numerical simulation of incompressible laminar flow in a three-dimensional channel with a cubical open cavity with a bottom wall heated. *J. Phys. Conf. Ser*. **Scimago journal rank (SJR): 0.21 (Q4)**.

DOI:10.1088/1742-6596/395/1/012099.

Contributions to conferences

[1] Abdelmassih G., Varela S., Vernet A. and Pallares J. (2013); DPIV experimental study of mixed convection in an open cavity, the *10th International Symposium on Particle Image Velocimetry, Delft, the Netherlands* (Oral Presentation).

URL: http://repository.tudelft.nl/islandora/object/uuid:f90cd143-8a26-4b7c-83b9-524f7ccbf37d?collection=research

[2] Abdelmassih G., Vernet A. and Pallares J. (2012); Effect of mixed convection in the flow in a channel with an open cavity, the *6th European Thermal-Sciences Conference, Poitiers, France* (Oral Presentation).

[3] Abdelmassih G., Striba Y., Vernet A. and Grau X. (2010); A direct numerical simulation study on the mean velocity and temperature in mixed convection from an open cavity, the *5th European Conference on Computational Fluid Dynamics, Lisbon, Portugal* (Oral Presentation).

Contributions Workshops

[1] Abdelmassih G., Vernet A., Pallares J., Effect of mixed convection in the flow in a channel with an open cavity. The *11th Doctoral day of the programme in Chemical, Environmental and Process Engineering (2013), Tarragona, Spain,* (Poster Presentation).

[2] Abdelmassih G., Vernet A., Pallares J., Effect of asymmetric incoming boundary layer on the incompressible flow over a cubical cavity. The *10th Doctoral day of the programme in Chemical, Environmental and Process Engineering (2012), Tarragona, Spain,* (Poster Presentation).

[3] Abdelmassih G., Stiriba Y., Vernet A. Analysis of the flow and heat transfer processes for the incompressible flow over cavities. The *9th Doctoral day of the programme in Chemical, Environmental and Process Engineering (2011), Tarragona, Spain*, (Poster Presentation).

[4] Abdelmassih G., Stiriba Y., Vernet A. Three-dimensional numerical studies on the laminar flow over an open cavity with a bottom wall heated. The *8th Doctoral day of the programme in Chemical, Environmental and Process Engineering (2010), Tarragona, Spain*, (Poster Presentation).

Figure index

Table index

CHAPTER 1

Introduction

1.1. INTRODUCTION TO OPEN CAVITY

Over the last decades, the flow structure over an open cavity was an attractive research point due to its importance in various engineering applications in different scales as fuselage, harbor entrance, bomb bay, solar collectors, cooling of electronic components etc.; see [1]–[10]. The plane design research centers focused on this point because the existence of this type of geometry in many parts in the fuselage, especially one of the most important parts having this shape is the landing gear wells, this because the force of air which in many times can affect the geometry [11].

Solar energy researchers reported that solar cells are used for water heating proposes at most of the times [12]. Installing wind barriers in the perimeter of the cell is improving the absorption efficiency since the wind barriers inhibit the direct convection occurring over the solar cell surfaces. The flat solar cell with wind barriers has the same geometry as an open cavity in medium scales, the research point extended to find the optimum aspect ratio, which the flow inside the cavity could be capsulated.

During the second half of the previous century, cooling of electronic components was one of the most vastly applications in small scales for the open cavity [5], [8], [13]–[17]. It is simple in design and has a cheap maintenance cost. The electronic component considered as the source of heat while the effects of the natural/mixed convection on the flow structure was the focusing point. It was sorted under three main categories depending on the position of the heated wall, e.g. the electronic board, within the enclosure. These categories are:

1. **Assisting flow:**

   Both of mainstreams in the channel and the buoyancy force of the heated wall of the cavity acting in the streamwise direction, i.e. the mixed convection assists the flow.

2. **Opposing flow:**

   The buoyancy forces of the heated wall of the cavity acting in the opposite direction of the mainstream in the channel, i.e. the mixed convection resists the flow.

3. **Heated from below:**

   The buoyancy forces of the cavity bottom heated wall acting perpendicular on the mainstream in the channel.

Moreover of all these applications, there is another main reason to make this geometry a point of interest, is that this geometry in the simplest isothermal configuration, i.e. without heat transfer, is often used to validate the computational model and numerical codes [18].

1.2. LITERATURE SURVEY

The early studies of flow past cavities were carried out in the 1960s. These studies were done by Weiss and Florsheim [1], Burggraf [2], and Pan et al. [3]. It was reported that the flow in a cavity is characterized by a recirculating flow in a closed domain. More studies have been carried out to reveal the laminar, two-dimensional flow structure and the heat transfer process occurring in cavities with different aspect ratios [4], [6], [9], [10]. It was reported that the vortical structure that exists inside the cavity is dependent on the dimensions of the cavity and the mixed convection (in cases of heated configurations).

O'Hern et al. [18] carried out an experimental study using two optically techniques. Laser Doppler Velocimetry (LDV) was used to measure point velocities, and video based particle tracking Particle Image Velocimetry (PIV) to measure full velocity map. These experimental results were compared with numerical results performed using finite element solver FIDAP. Water flow was used. It was driven by a fully developed laminar channel flow passing over the top of the cavity. Reynolds number is ranged from 100 to 900. A good agreement was found by comparing the experimental and the numerical results.

The hydrodynamics instabilities in open cavities were studied by Huerre et al. [19]. It was reported that viscous diffusion between the external and cavity flow create a zone with steep gradients of streamwise velocity concentrating most of the vorticity. Detailed information on the velocity, turbulent distribution and the interaction between turbulent boundary layer and the cavity can be found in Lin et al. [20].

Manca et al. [5] studied numerically the effect of heat wall position on mixed convection in a channel with an open cavity. The numerical model applied was two-dimensional. Different aspect ratios were studied. It was reported that the maximum temperature values decrease as the Reynolds number and Richardson number increase for all the studied configurations. The developing flow in a series of canyon streets has been investigated at [21], [22]. The flow structure inside the street canyon is of crucial importance for the dispersion of the pollutants emitted from street level, particularly vehicular exhausts.

Zdanski et al. [23] studied numerically both laminar and turbulent flow in two-dimensional over shallow cavities for incompressible flow with average Reynolds number. They studied the effect of the Reynolds number, turbulent level of incoming flow and cavity aspect ratio on the flow structure. It was reported that for the turbulent case the external flow touches the floor of the cavity at specific value of each of these parameters.

Yao et al. [24] used finite difference scheme to study numerically incompressible laminar flow over three-dimensional rectangular cavities. They indicated that for a given Reynolds number, the flow structure is affected by the thickness of the inflow boundary layer with a significant interaction between the external flow and the recirculating flow inside the cavity. At moderate Reynolds numbers, the shallow cavity flow is more stable than deep cavity flows. The flow inside the enclosure becomes unsteady and complex at high Reynolds number. Faure et al. [25] visualized experimentally the flow structure inside an open cavity at a medium range of Reynolds number, $1150 \leq Re \leq 10670$, with different aspect ratio cases $0.5 \leq AR \leq 2$. They reported that the developments of the dynamic structures in the three dimensions are not caused by secondary shear layer instabilities.

Manca et al. [8] investigated experimentally the opposing mixed convection in an open cavity with a heated wall bounded by a horizontal unheated plate. The heated wall is on the opposite side of the main stream. The ranges of parameters used in this experiment are Reynolds numbers ($100 \leq Re \leq 2000$), and Richardson numbers ($4.3 \leq Ri \leq 6400$). The ratio between the length and the height of cavity is $0.5 \leq L/D \leq 2.0$, while the ratio between the channel and cavity height is $H/D=1$. The results show that at the lowest Reynolds number ($Re=100$), the surface temperatures are lower than the corresponding surface temperatures for $Re=2000$ at the same ohmic heat flux. The flow visualization shows that for $Re=1000$, there are two nearly distinct fluid motions: a parallel forced flow in the channel and a recirculation flow inside the cavity. For $Re=100$, the effect of a stronger buoyancy determines a penetration of thermal plumes from the heated plate wall into the upper channel. Analyzing the flow visualization shows that for lower Reynolds numbers, the forced motion penetrates inside the cavity and a vortex structure is adjacent to the unheated vertical plate. At higher Reynolds numbers, the vortex structure has a larger extension while L/D is held constant.

Stiriba [26] and Stiriba et al. [27] studied numerically in three-dimensional approach the flow and heat transfer characteristics for assisting and opposing incompressible laminar flow past an open cavity. The results show that the flow exhibits a three-dimensional structure and is steady for Re=100 with Ri ranging from 0.01 to 10 and Re=1000 with Ri ranging from 0.001 to 1. The forced flow dominates the flow transport mechanism and a large recirculating zone from inside the enclosure. These studies were followed by several studies for the mixed convection and the flow instabilities over an open cavity; see [15], [28]–[30].

Abdelmassih et al. [17] used a finite volume flow solver to present a three-dimensional numerical simulation study for both laminar steady and unsteady regimes to interpret the mixed convective flow over a three-dimensional cubical open cavity. The bottom of the cavity was heated at constant temperature while the other walls are adiabatic. The range of Reynolds numbers is $100 \leq Re \leq 1500$. Prandtl number (Pr) for the air flow is set to 0.7. Richardson number range is $0.001 \leq Ri \leq 10$. It was reported that, for both high Re and Ri the flow becomes unsteady. The mixed convection effects dominate the flow transport mechanism and push the recirculation zone and the flow further upstream. Beside this study, Stiriba et al. [31] compared between velocities within a rectangular cavity heated from below in the same ranges of [17]. They concluded that increasing Richardson number generates remarkable velocities differences while the inflow Reynolds is held constant. Zamzari et al. [14] achieved a two-dimensional study of the entropy generation and mixed convection in a horizontal channel with an open cavity. A laminar air flow in a range of $200 \leq Re \leq 500$ and $0.25 \leq Ri \leq 1$ was considered. Results show that the cavity flow, heat transfer rates and entropy generation are strongly affected by variations of the Reynolds number, Richardson number and the aspect ratio. Most of the previous studies were used air flow, where constant properties and Boussinesq approximation were applied. The variation of viscosity and expansion coefficient were neglected.

For the water flow, the effect of temperature dependent physical properties found in the literature indicates that the overall flow topologies are not affected by the effects of the physical properties variation with temperature in natural convection case; see [32]. The authors studied the effects of a non-Boussinesq fluid for Rayleigh-Bénard convection in a cubical cavity using water as a convecting fluid. These simulations were considered with variations of 62% and 40% of the thermal expansion coefficient and viscosity, respectively, between cold and hot plates.

Zonta et al. [33] studied the effect of temperature dependent fluid properties on mixed convection heat transfer in turbulent flow channel. The authors performed a flow simulation for both constant and temperature dependent fluid properties at three different absolute values of the Ri=926, 498, and 346 in a range of Reynolds numbers $110 \leq Re \leq 180$. They have found that the effect of thermal expansion coefficient on mixing increases for increasing Ri and decreases for increasing Re, and they reported that only the effect of $\beta(T)$ is important, whereas the effect of $\mu(T)$ is negligible.

In this work, the Ri is decreased to be much smaller than used in [33]. Also, Re is increased which means that not only $\mu(T)$ will not affect the flow topology and is negligible but the effect of $\beta(T)$ is expected not to make any significant change on the flow structure. However, these numerical results are not sufficient. The effect of the temperature dependent physical properties for the uncovered range at [32] and [33] should be analyzed.

Although the rich literature of the open cavity studies, there is much work left to be done in this area. Basically, little information exists for the mixed convection in cavity flows. Other aspects have also to be analyzing such as the three-dimensional flow structures and the flow behavior when it is unsteady. Identifying the vortex core is also important to illustrate the three dimensions swirl motion of the flow.

In the present work, experimental and numerical data are presented and compared to analyze the behavior of the cavity flow. The main objective is to study the mixed convection focusing on the effect of the buoyancy forces on the flow topology and temperature fields for an incompressible laminar inflow over an open cavity with a bottom wall heated.

Air and/or water inflow were used separately in this work. The ranges of Reynolds and Richardson numbers considered ($100 \leq Re \leq 1500$ and $0.1 \leq Ri \leq 10$) correspond to the usual operating conditions of some processes associated with the cooling of electronic components. The effect of Ri on the flow stability and its performance in three dimensions is still unobvious. Explaining/analyzing the behavior of the flow, when it is unsteady, is the main part of this work. It was essential to validate the numerical results by achieving an experimental study for the most sensitive cases and consequently we guarantee the rest of the results.

CHAPTER 2

Numerical approach

The numerical approach used is described in this chapter. Air and water inflow were used separately. A laminar inflow with a uniform velocity is considered in the channel passing over the top of an open cavity.

2.1. GEOMETRY

The geometry of the channel including the cubical open cavity and the computational domain used in this study are shown in **Figure 2.1**. Where L is the length, width and height of the cavity (AR=1). The length of the channel from the inlet opening to the cavity leading edge is L, while 2L is the length of the channel behind the cavity trailing edge in the streamwise direction, and the height of the channel is L.

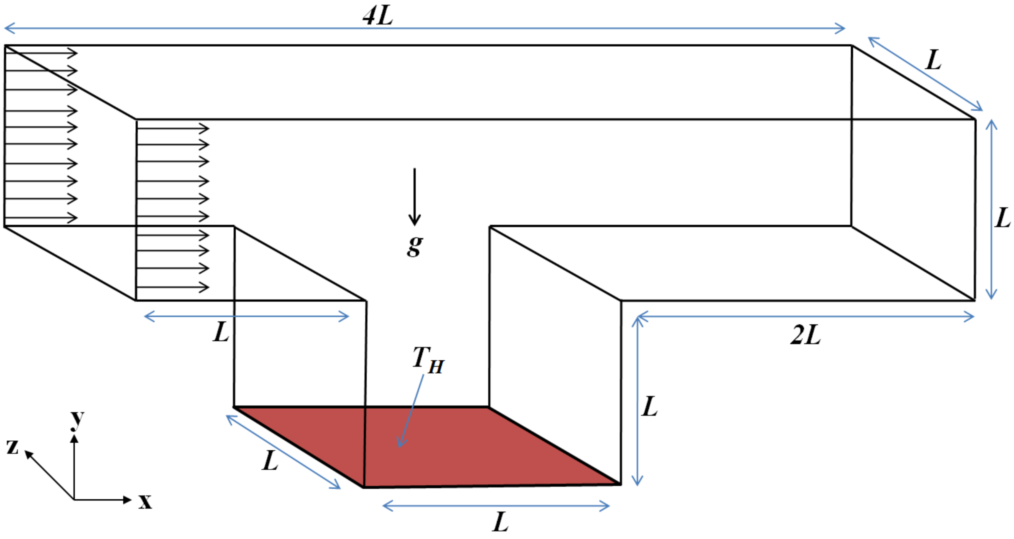

Figure 2.1: Sketch of the geometry.

2.2. PHYSICAL PROBLEM

The inflow direction is from left to right with a uniform velocity U_0 and a constant temperature T_∞ at x=0. Convective Euler boundary condition is assumed for the outflow located at x=4L and the non-slip boundary condition is applied for the rest of the boundaries. The cavity is heated from below at a constant temperature T_H, and the remaining walls of the cavity and the channel are adiabatic.

A cooling incompressible inflow at constant temperature T_∞, was applied. Air and water inflow were used separately in two different studies. Prandtl number for air flow cases is set (Pr=0.7), while for water flow cases is set (Pr=7). The Reynolds number range for both studies (air and water flow) is set ($100 \leq Re \leq 1500$), while the Richardson number range is ($0.001 \leq Ri \leq 10$). The thermo-physical properties of air flow are assumed to be constant in this range, except for the change in fluid density with temperature according to the Boussinesq approximation; see [4], [5], [26], [27], [31], [34]–[36].

The thermo-physical properties of water flow were investigated. The effect of temperature dependent physical properties found in the literature indicates that the overall flow topologies are not affected by the changes on the physical properties with temperature in the natural convection [32] or the mixed convection [33] in the specified ranges mentioned previously.

In this study, the range of Ri is decreased to be much smaller than that used in [33] as well as the range of Re is increased. This implies that not only the effect of the viscosity variation μ(T) will not affect the flow topology, but also the effect of the variation of thermal expansion coefficient β(T) is also expected not to make any significant change on the flow structure. However, since the effect of β(T) in the literature is not covering the considered ranges (Re=100-1500) and (Ri=10^{-3}-10). Numerical simulations to study the effect of β(T) have been implemented. The change of the thermal expansion coefficient with the temperature was governing by the following dimensional equation [37]:

$$\beta(\mathrm{T}) = 9.38 \times 10^{-6} \cdot T - 2.54 \times 10^{-3} \qquad (2.1)$$

where T in (K) and β in (1/K).

2.3. GOVERNING EQUATIONS AND NUMERICAL METHOD

The 3DINAMICS finite volume parallel code has been used in this work [13], [17], [26], [27], [31]. The code solves numerically three-dimensional incompressible Navier-stokes equations (2.2─2.4) for mixing convection [37] on non-uniform staggered Cartesian meshes. The fluid properties are assumed constant for air flow except for the change in fluid density with temperature, according to the Boussinesq approximation.

The variation of the thermal expansion coefficient with the temperature (non-Boussinesq) was applied in equation (2.5) for water's crucial cases in order to compare with Boussinesq cases. The SMAC method is used to join continuity and momentum equation, in which, the Poisson equation for the pressure is computed with the biconjugate gradient method (BiCGtab). Convective and the diffusive terms are approximated using SMART scheme [38] and central differences, respectively.

$$\frac{\partial u_i^*}{\partial x_i^*} = 0 \tag{2.2}$$

$$\frac{\partial u_i^*}{\partial t^*} + \frac{\partial (u_j^* u_i^*)}{\partial x_j^*} = -\frac{\partial p^*}{\partial x_i^*} + \frac{1}{Re}\frac{\partial^2 u_i^*}{\partial x_j^* \partial x_j^*} + Ri\, T^* \delta_{i2} \tag{2.3}$$

$$\frac{\partial T^*}{\partial t^*} + \frac{\partial (u_j^* T^*)}{\partial x_j^*} = \frac{1}{Re.Pr}\frac{\partial^2 T^*}{\partial x_j^* \partial x_j^*} \tag{2.4}$$

$$\frac{\partial u_i^*}{\partial t^*} + \frac{\partial (u_j^* u_i^*)}{\partial x_j^*} = -\frac{\partial p^*}{\partial x_i^*} + \frac{1}{Re}\frac{\partial^2 u_i^*}{\partial x_j^* \partial x_j^*} + Ri\, T^* (1 + 0.29T^* + 0.037T^{*2})\delta_{i2} \tag{2.5}$$

The dimensionless variables are defined as:

$$x_i^* = \frac{x_i}{L}\,,\quad t^* = \frac{U_0 t}{L}\,,\quad u_i^* = \frac{u_i}{U_0}\,,\qquad p^* = \frac{p}{\rho_\infty U_0^2}\,,\quad T^* = \frac{T - T_\infty}{T_H - T_\infty}\,,\quad Ri = \frac{Gr}{Re^2}$$

where U_0 refers to the inflow velocity components, u_i refers to the velocity components, ρ_∞ is the density, T_H is the temperature at the heated wall surface, $Re=(U_0 L)/\nu$ is the Reynolds number, Ri is the Richardson number, Gr is the Grashof number, $Gr=(g\beta \Delta T L^3)/\nu^2$, and Pr is the Prandtl number, $Pr=\nu/\alpha$. Here β, ν, and α are the coefficient of volumetric expansion, kinematic viscosity, and thermal diffusivity, respectively.

$$Nu_l = \frac{\partial T^*}{\partial y^*}\Big|_{y^*=0} \quad , \qquad Nu_s = \int_0^1 \int_1^2 Nu_l \, dx^* dz^* \tag{2.6}$$

Nu_l is the local Nusselt number and surface average Nusselt number is Nu_S, are applied equation (2.6), to represent heat transfer at the heated wall. The numerical code was validated at [17], [26], [27], [31].

2.4. GRID INDEPENDENCE

In general, to solve any flow problem using finite volume approach, the fluid properties that include velocity, pressure, and temperature are calculated across the surfaces of each finite control volume in the grid of whole geometry domain. The number of cells in the grid controls the accuracy of a CFD solution. The large number of cells presents better solution accuracy. The solution accuracy and its cost in terms of necessary computer hardware and calculation time are dependent on the fineness of the grid. Non-uniform meshes are optimal meshes because these meshes are finer in areas where exhibit to large variations from point to point and coarser in regions with relatively little change. Great efforts are under way to develop CFD codes with a self-adaptive meshing capability; such programs will automatically refine the grid in areas of rapid variations [39]. A substantial amount of basic development work still needs to be done before these techniques are robust enough to be incorporated into commercial CFD codes. The skills of the CFD user are playing an important role in design a grid that is a suitable compromise between desired accuracy and solution cost. A big time spent in industry on a CFD project is devoted to the definition of the domain geometry and grid generation.

Non-uniform grid sizes have been used in this work. The grid is narrow close to the walls to capture the rapid changes in the dependent variables; see **Figure 2.2**. To check the grid independence of the solution, three different grids were tested: 160×80×40, 200×100×50 and 220×110×60. The tested grid sizes correspond to 40^3,50^3 and 60^3 grid points in the cavity, respectively. The grid independency was checked at Re=1500 and Ri=10. **Figure 2.3** shows a comparison between the temperatures of the different grids at x^*=1.5 and z^*=0.5. The results with the other two meshes show less than 2% difference in the average temperature and the averaged surface Nusselt numbers at the heated wall. Finally, the grid of 200×100×50 (50^3 grid points inside the cavity) was used in this work to provide a high resolution in a reasonable time.

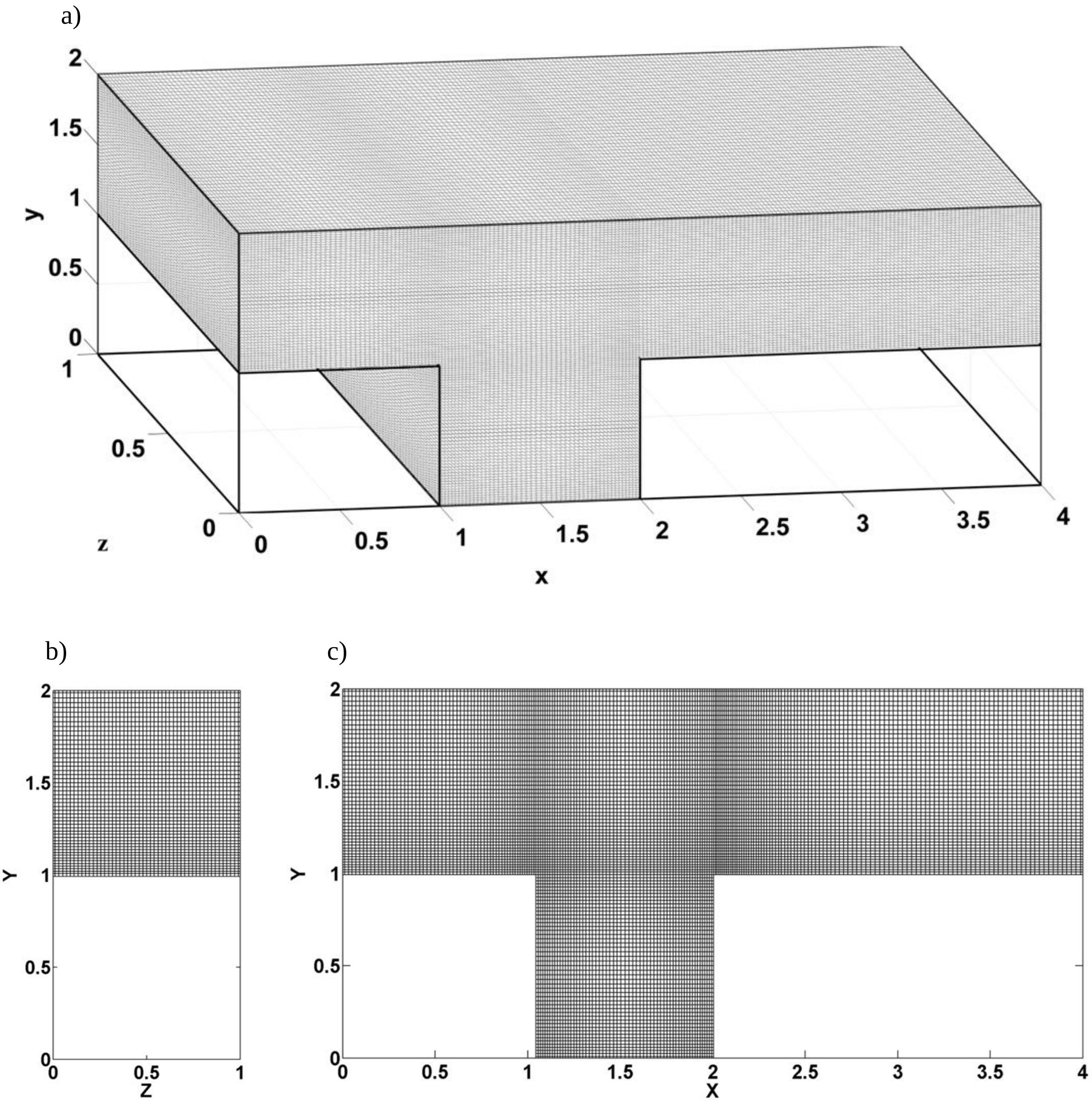

Figure 2.2: Sketch of the non-uniform grid.

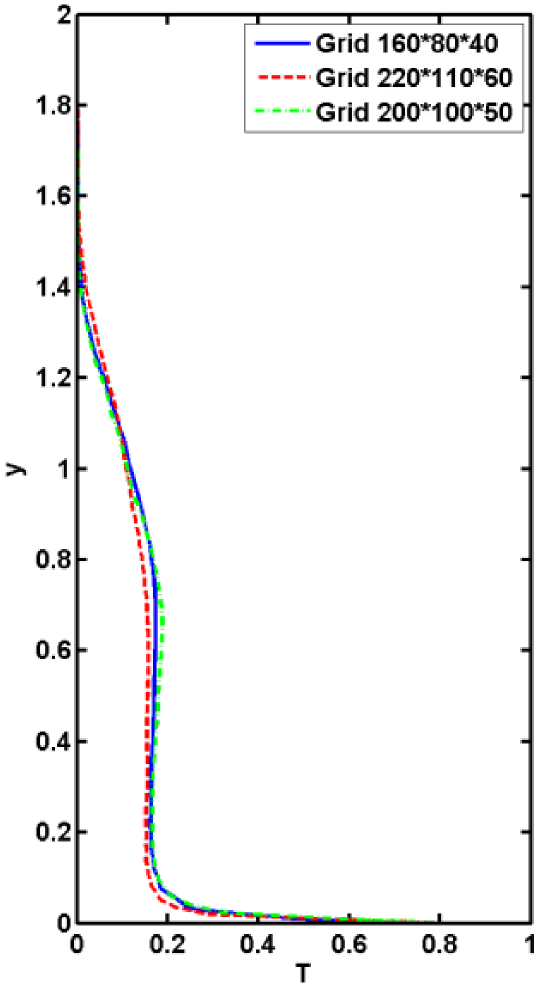

Figure 2.3: Comparison between the temperatures at x^*=1.5 and z^*=0.5, for Re=1500 with Ri=10, for the different grids.

CHAPTER 3

Experimental techniques: PIV

The experimental part of this work has been done using Particle Image Velocimetry (PIV). It is a frequent optical and non-intrusive method for flow visualization and velocity measurement used in the analysis of fluid flows. The basic PIV configuration allows to measure two velocity components in a two-dimensional plane that is illuminated with a thin light sheet.

PIV was initially developed by Adrian in 1984 [40] and generalized in the following years, among others, by Westerweel [41]–[44]. The development in the photographic techniques and the creation of digital cameras was a turning point in developing the PIV technique as applicants moved from using filmed images to digital images captured by digital cameras while the technique renamed to Digital Particle Image Velocimetry (DPIV). The new technique becomes easy and more accurate in determining the flow velocity field. The principles of this measurement technique are described in this chapter.

3.1. PIV BASICS AND PRINCIPLES

Basic PIV technique can be divided in two main parts: image acquisition and image processing. Image acquisition is achieved in the laboratory and it requires an experimental setup, with the moving fluid of interest, and some specific equipment as cameras (for image recording), laser (for illumination) and tracer particles (for seeding the fluid). The image processing is the part of the technique where the recorded images are analyzed and used to obtain the fluid velocity field. This part can be achieved separately of the experiments and usually is done latter in a computer using specific software.

PIV is applied to visualize the flow, thus, both the experimental setup and the fluid need to be transparent, allowing the lighting and the acquisition of the images. For this reason to visualize the fluid movement, some especial particles need to be added to the fluid acting as tracers of the fluid movement. From the recorded image, the technique detects the particles and computes their velocity. The velocity of the fluid is obtained assuming that the velocity of the fluid is the same as the velocity of the particles. Illumination is also an important element of the PIV technique. Usually a thin laser sheet is used to illuminate the plane region of interest. The basic PIV configuration is shown in **Figure 3.1**.

A digital camera captures two consecutive images of the illuminated region of interest within a short time interval Δt, these images are stored for latter processing. During the short time interval, the particles will have moved driven by the underlying flow. Measuring the straight-line displacement of these tracer particles yields a field of linear displacement vectors where each vector presents a displacement value and direction of the movement of a localized group of these particles. This process is applied in practice by discretizing the whole images to small windows called interrogation windows. Analyzing them statistically allows calculating the local velocity as a function in displacement and time.

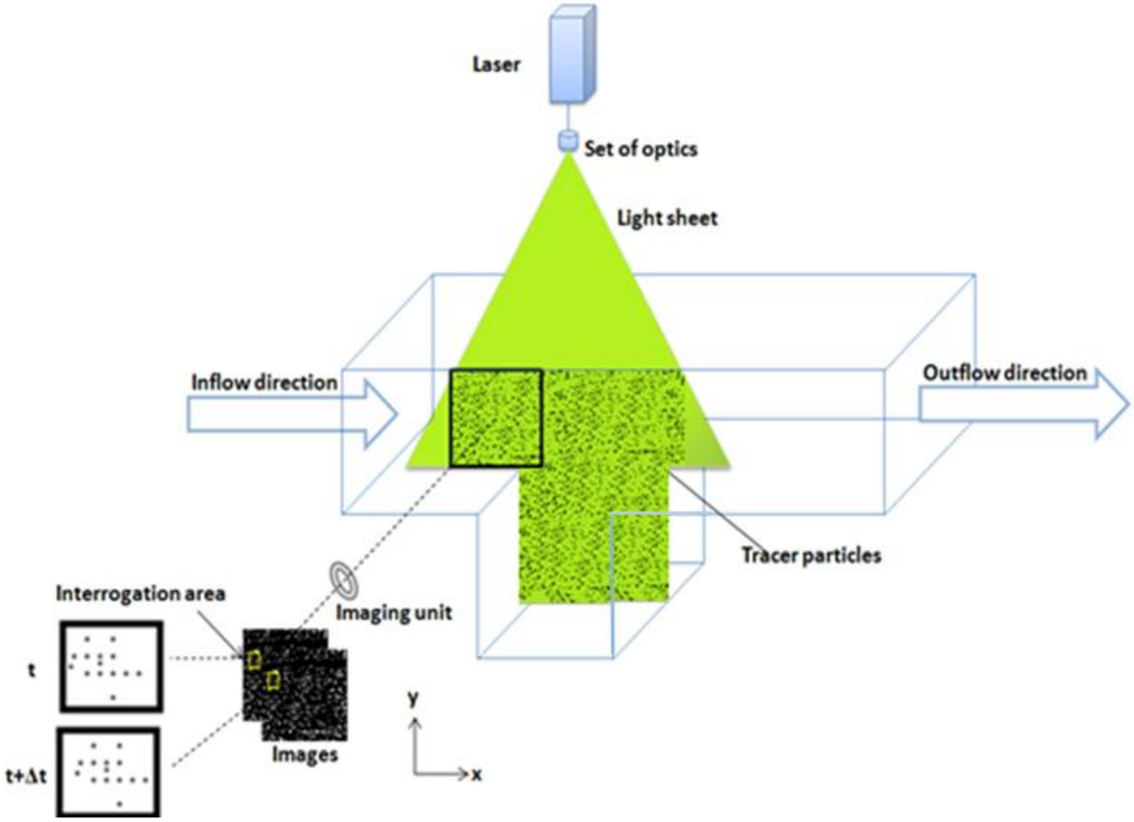

Figure 3.1: Sketch of the experimental technique.

3.2. TRACER PARTICLES

Tracer particle selection is important to get accurate measurements since the tracer particles must follow the fluid motion completely. This happens when the slip velocity of the particles with respect to the fluid velocity is small. The relaxation time constant is the time that particles need to adjust a sudden change in the velocity. It is affecting the slip velocity. When relaxation time constant is small in comparison with the smallest time scale of the fluid motion, the particle follows the flow completely.

Several properties of the tracers must be considered in the process of selecting the appropriate seeding material for a particular PIV application. The choice of the right seeding particles to scatter the light sheet or a light from laser beams can be crucial to the image acquisition process. Mean particle size is only one of the parameters. Others include specific gravity, particle shape and size distribution, surface characteristics and refractive index. Some of the requirements of the particles to have PIV working properly are [45]:

- The particles must have similar density of the fluid. This because, if the particles density is smaller than the fluid density the particles will float, while the particles sediment in the bottom if its density is higher. At very low Reynolds numbers, the ability of the particles to follow the fluid's flow is inversely proportional to the difference in density between the particles and the seeded fluid.

- The refractive index for the seeding particles must be different from the seeded fluid, therefore the laser sheet incident on the fluid flow will reflect off the particles and be scattered towards the camera.

- The particles must be small enough so that the response time of the particles to the fluid motion is reasonably short to follow the flow accurately. The ability of the particles to follow the fluid's flow at very low Reynolds numbers is inversely proportional to the square of their diameter. In practice the lower limit of the particles is dp>1μm, as the scattering intensity decreases rapidly for particles smaller than 1 μm [46].

- The particles must be large enough to scatter enough light to be accurately visualized within the laser sheet plane and consequently in the captured images. The scattered light from the particles is proportional to the square of the particles' diameters. Thus, the particle size needs to be balanced to scatter enough light, but small enough to follow the flow accurately.

- The particles must be homogeneously distributed over the light sheet to be able to make a fair estimation of the particle displacement by correlation techniques. Also, to avoid the large differences in the number of particles in the interrogation areas. The particles homogeneity over the light sheet strongly depends on the time constant of the particles. Homogeneously distributed planes can be achieved if particles are small enough to follow the flow accurately. In addition, the particles must be recirculated through the setup, i.e. after adding particles the setup should run for a sufficient time. The particles must not alter the fluid properties. This can be achieved when the particles material guarantees that no chemical reactions occur between the particles and the fluid flow

- The particles concentration in the fluid must be adequate, i.e. not high to avoid the speckle problems in the images and not low to provide information in all parts of the images. The distribution of the particles should be homogeneously over the light sheet to allow making an unbiased estimation of the displacement of the particles using the correlation techniques and to avoid too large differences cases in the number of particles in the interrogation areas. Statistically, the meaningful number of tracer particles in the interrogation windows is roughly ten [47].

3.3. IMAGE ACQUISITION

The flow velocity in PIV is measured by tracing the motion of small tracer particles present in the fluid. A camera captures the image strips of the illuminated particles in desire plane. Controlling the time interval during the capturing process is very important to achieve accuracy measurements. Time interval between two successive images must be short enough to permit the tracers appearing in an image also appear in the next, and long enough to present a noticeable movement of these particles.

Indeed, there is an inverse proportionality between the capturing frequency (frames per second) in any digital camera and the exposition rate, as the maximum exposition value is decreased as a respond of increasing the capturing frequency.

An adequate exposure value must be identified since low exposure is not sufficient to provide accurate image strips, while the high exposure makes the particles look like traces in the images. Although, these traces can be used to visualize the flow movement, it is not positive for PIV that requires seeing the particles as points for accurate correlation.

3.4. IMAGE PROCESSING

Processing technique includes all the steps necessary to obtain the velocity fields from the raw particle images. The general idea is that two consecutive images containing particle were previously recorded together with a short time interval, are used to obtain the velocity field from the straight-line displacement of the tracer particles.

The cross correlation estimates the relative displacement of the particles. This correlation is computed with help of the Fast Fourier Transform algorithm. The image pair can yield a field of linear displacement vectors, where each vector is formed by analyzing the movement of localized groups of particles.

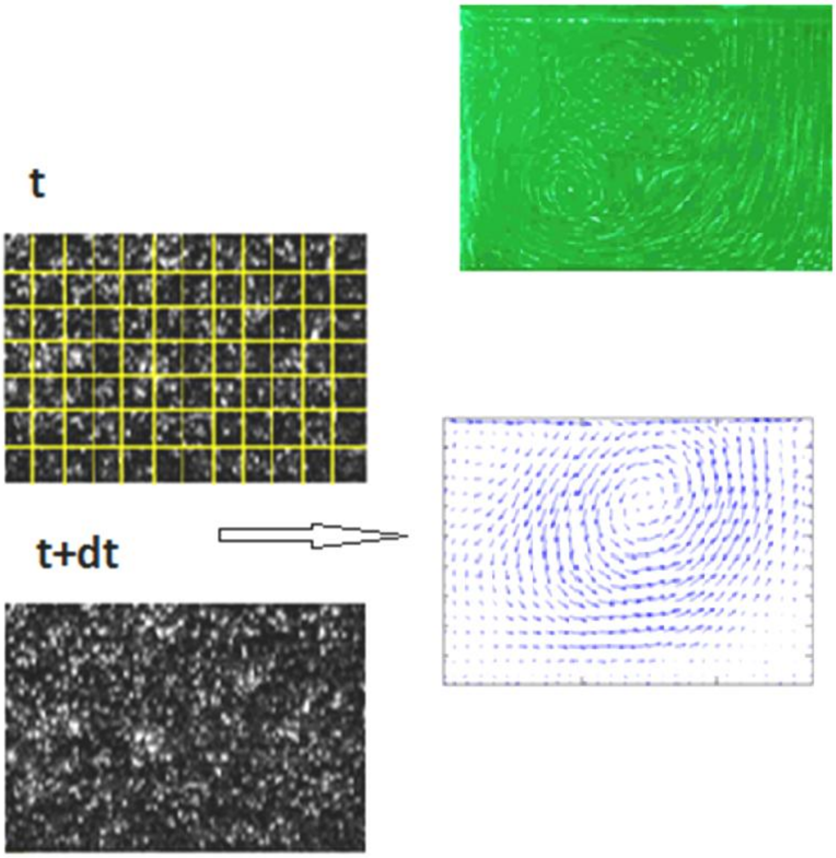

Figure 3.2: The procedures necessary to obtain the PIV velocity field.

In practice, the estimation is performed by extracting small samples and analyzing them statistically. Rather than estimating the displacement function analytically, the method of choice is locally finding the best match between the images in a statistical sense. This is accomplished using the discrete cross-correlation function. Consequently, to implement the correlation, a discretization preprocess must be applied. Each image is divided into subdivisions (small regions) called interrogation windows. An example of this procedure is shown in **Figure 3.2**.

In the most common cases the interrogation window sizes range from 8 to 128 pixels depending on the size of the digital image, the seed particle size and seeding density. The sample in these common implementations is 32×32 pixels or 64×64 pixels. In our case, the interrogation window has a size of 32×32 pixels with an overlapping of 16 pixels.

Estimation of displacement for a given shift of two samples depends on the cross-correlation function, which measures statistically the degree of match between the two samples for a given shift. The maximum value will obtained in the correlation plane is used as a direct estimate of the particle image displacement.

The subdivisions are controlled by the grid spacing and size of the interrogation window. The grid spacing is the space between measurements in the image. For example, if the grid spacing is 4 pixels, this means that in the output will have a velocity every 4 pixels in the image, or a 64×64 grid of velocity measurements for an image size of 256 pixels. In this work, each image was divided into 32×32 interrogation windows.

Each window should have appropriate concentration of particles since the accuracy deteriorates and produces error vectors due to losses of many particle pairs in a complex flow region while speckle problem arises in high concentration cases. Roughly, the necessary number of the particles for each window is ten [47]. The particles in each window assumed to be moving in a uniform shape during the short time interval between the consecutive images.

3.5. PIV-MATLAB

Different PIV software codes are available in the library that used over the world in PIV image processing. PIV-Matlab code was used in the image processing stage in this work. The code developed by several members of ECOMMFIT group. It consists of a set of routines written in Matlab® that process a series of particle images, and computes the velocity fields associated. PIV-Matlab has been tested in such studies as [13], [48], [49].

PIV-Matlab code obtains the velocity field of the fluid flow for any series of images. Its options can be adapted for the necessary conditions of the fluid flow and image properties. One of these options is to correlate between two or three consecutive images.

The code is open, which permits adding new options to obtain the desired characteristics velocity field. Some of these options are related with higher methods, which improve the performance and accuracy of the PIV technique. A brief idea of the PIV-Matlab is presented in the following sections, while the most important options are explained in details in [48].

The time series of PIV images show the time history of the illumination at each pixel, and its statistical properties can be analyzed. The value of the illumination at each point provides information regarding the permanent background illumination that reveals the existence of spurious illuminations, reflections or stick to the wall particles that affects the detection of the actual displacement of the particles.

To remove/reduce the undesired light reflections and homogenize the median illumination, a clean-up mask approach has been used to tackle the samples of the particle images [48], [50]. The use of the clean-up mask is a pre-process step to define the permanent background reflections to get accurate velocity vectors. As illustrated in **Figure 3.3**, the clean mask procedure prevents the spurious correlation peaks due to the presence of permanent bright spots. Permanent spots must be removed, since it tends to 'lock' the correlation to null displacement. The clean-up mask was applied for 100 images of each series.

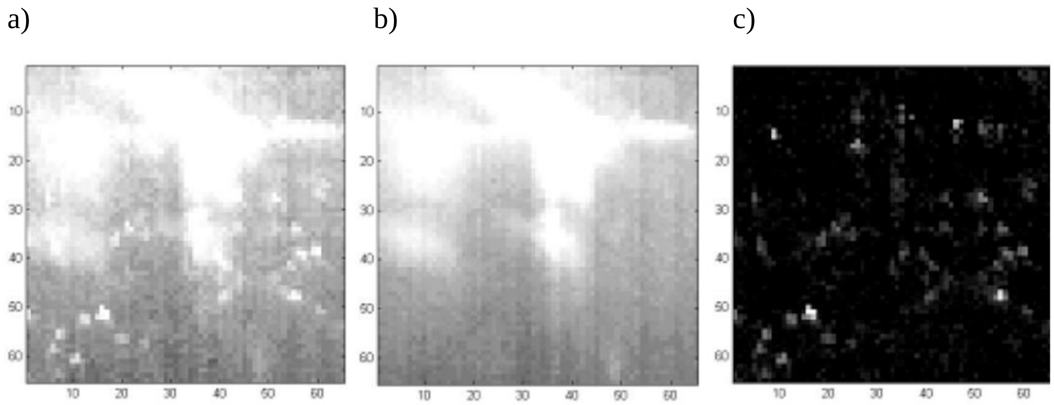

Figure 3.3: Reflections removal by median estimator across time series. a) Original instantaneous image, b) Median image from a time series of 512 images, and c) Difference image between the original and the median [48].

Large reflections may cause the saturation of areas involving several pixels, so that particle image information cannot be recovered there. However, in the case where 'mild' reflections occur, not reaching the saturation level, image particle information can still be recovered by proper treatment of the local brightness histogram.

The out of plane displacement causes a loss of correlation or other problems that produce spurious vectors. This can also be reduced by dealing with well resolved time series of PIV images [50]. Basically, any given image of the time series can be paired with either the next or the previous image in the time series. As long as the out of plane displacement is kept smaller than half the laser sheet thickness, every particle presents in one image will have its counterpart in either the next or previous image. A correlation algorithm involving the three images should prove more robust to out of plane motion than the usual single pair correlation algorithm. The algorithm used here implements this strategy by multiplying both correlation planes in order to improve the peak detection. This leads to the attenuation of the spurious correlation peaks appearing in only one of the correlation planes, while increasing the absolute height of the valid peak.

Local Field Correction Particle Image Velocimetry (LFCPIV) has been applied [51], in order to accurately resolving small scale structures in the flow and down to a few times the mean distance between particles as the LFCPIV has a remarkable capability to resolve flow structures much smaller than the interrogation windows. Local field correlation (LFC) method [51] was implemented on triple image correlation to obtain the mean displacement of the ensemble particles image series hence the triple image correlation algorithm enhances the peak correlation in moving parts that appear in the image.

Boundary treatment technique has been applied using the weight function to obtain a good resolution of the velocity fields and achieve an accuracy level equivalent to inner flow location accuracy.

The interrogation technique delivers a small percentage of erroneous velocity vectors. These spurious vectors due to the limitations of each technique and the images quality. The homogeneous seeding images do not prevent the existence of image portions without useful information because of the lack of particles or out of plane displacement of the particles. Some interrogation techniques have limitations to the minimum or maximum in plane detectable displacement of particles. This may also lead to the occurrence of spurious vectors.

At image acquisition, there is always a certain amount of noise, ambient light, bad focusing or alignment. That may deteriorate the signal to noise ratio in portions of the image. Thus, some kind of quality control of the obtained vector field must be performed in order to discriminate between vectors corresponding to correct measurements with uncertainty and spurious vectors, as classified at [51].

Local Median Validation is done to the displacement data by computing median value for each 3x3 windows and borders are completed by these median values. Also, standard deviation median values are calculated and validated to the borders. A simple global histogram validation of PIV displacement data has been performed in the program.

Nogueira et al. [52] present a validation algorithm called Eye Validation. The proposed algorithm emulates the behavior of human visual validation. This process starts by locating a zone where the vector field seems coherent and proceeds scanning through the vector field, visually tracking the local gradient until a location is reached where vectors clearly deviate from the previously scanned coherent ones. In this way, more than mere local information is used to decide whether a vector belongs to the vector field or not.

CHAPTER 4

Experimental setup

In this chapter, the experimental setup used for our experiments was described. First, the flow facilities were described. Then, it followed by the PIV measurement devices, such as illumination and imaging systems.

4.1. CAVITY AND CLOSED CHANNEL

A model of an open cavity located in the bottom of a horizontal channel has been designed and constructed at ECOMMFIT (**Figure 4.1**). The cavity design allows working in different configurations, such as:

- **Isothermal configuration:** No heat transfer occurs since the walls of the cavity have a no-slip condition [18], [13].
- **Bottom wall heated configuration:** The bottom wall of the cavity is heatable while the rest of the walls of the cavity and the channel are adiabatic [5], [13], [16], [17], [31].
- **Assisting flow configuration:** The vertical wall of the leading edge is heatable while the rest of the walls of the cavity and the channel are adiabatic. The temperature is pushing the flow in streamwise direction. Therefore, it is called assisting flow [5], [26].
- **Opposing flow configuration:** The vertical wall of the trailing edge is heatable while the rest of the walls of the cavity and the channel are adiabatic. The temperature is pushing the flow in the opposite direction. Therefore, it is called opposite flow [5], [27].

- **More configurations:** The previous heated vertical walls configurations can also be combined to give more configurations (**Figure 4.1.b**). The cavity parts are replaceable as the required configurations.

However, two configurations only were conducted in this work: isothermal and bottom heated wall configuration. The studied cases are shown in **Table 4.1.**

Table 4.1. List of the experimental cases

<table>
<tr><td colspan="2"><i>Isothermal configuration</i></td></tr>
<tr><td>Re</td><td rowspan="3">No heat transfer occurs</td></tr>
<tr><td>1000</td></tr>
<tr><td>1500</td></tr>
<tr><td colspan="2"><i>Heated bottom configuration</i></td></tr>
<tr><td>Re</td><td>Ri</td></tr>
<tr><td>1000</td><td>10</td></tr>
<tr><td>1500</td><td>10</td></tr>
</table>

The cubical cavity with 100mm inner length is set up in a square cross-section channel 100mm×100mm as shown in **Figure 4.1** and **Figure 4.2**. The length of the channel is 500mm. The length from the inflow tank to the cavity leading edge is 100mm while the cavity is followed by a 300mm outflow length.

The material used in the fabrication of the walls of the cavity and the channel is poly-methyl-methacrylate (PMMA). This transparent material having the property of transmitting rays of light through its substance particles to admit optical access for the PIV measurements. PMMA Sheets of 20mm thickness were used in the fabrication process. A stair single step 10mm in all edges has been made in order to resist the flow rate pressure and avoid any leakage.

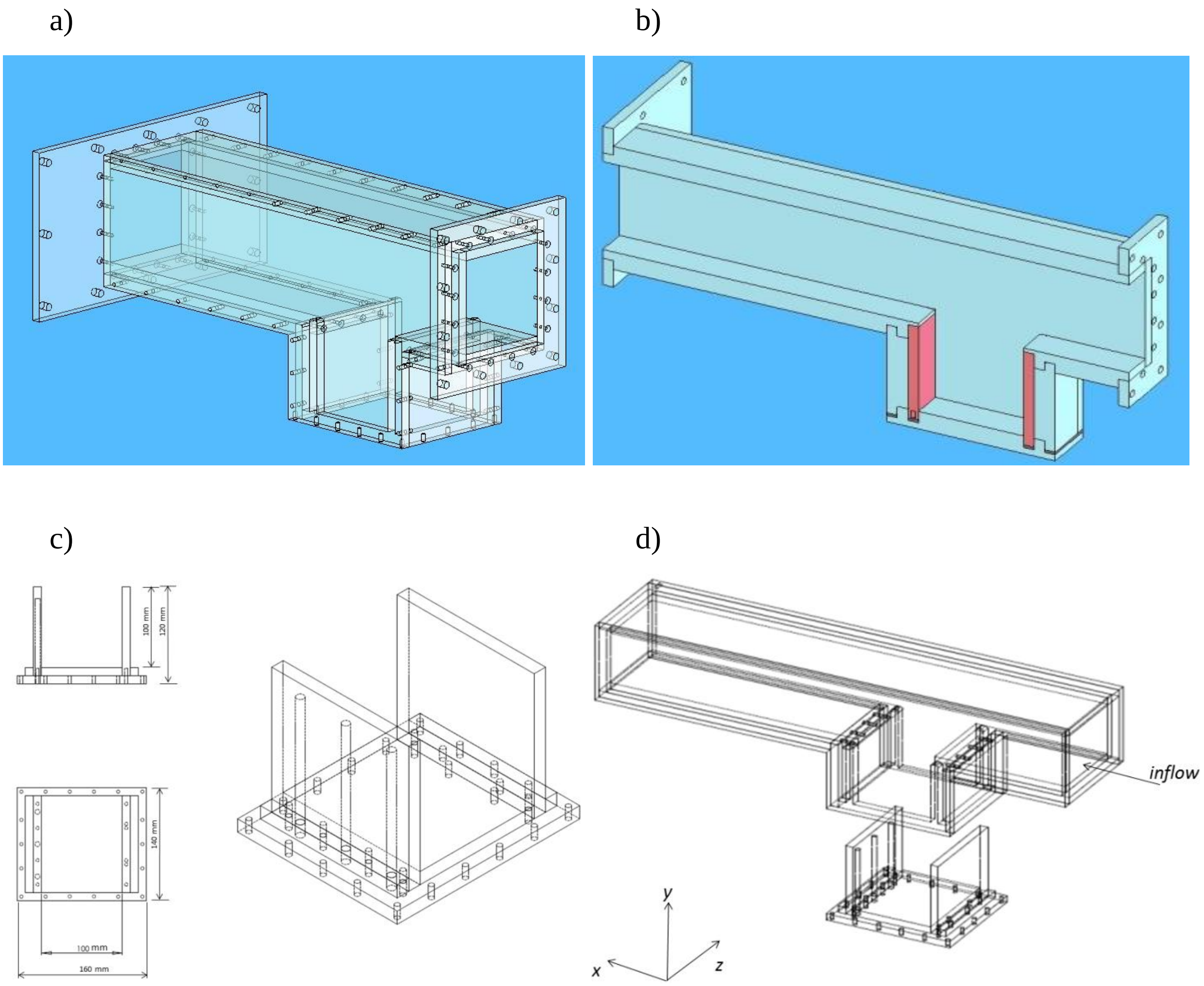

Figure 4.1: The designed model of the channel with the open cavity.

The inflow tank receives the water through a controlling valve. It is used to direct the water flow from the top and the bottom in the same time, to avoid the creation of eddies within the inflow tank. The water in the inflow tank passes through seven mesh plastic screen 1mm×1mm, separated each other with 15 mm distance, spited in two groups separated by a honeycomb 10mm×10mm with 30mm thickness (**Figure 4.3**). After the filters, the flow passes through a smooth contraction to reduce the section from 90000 mm^2 to 10000 mm^2 and ensures a flat velocity profile at the entrance of the channel.   .

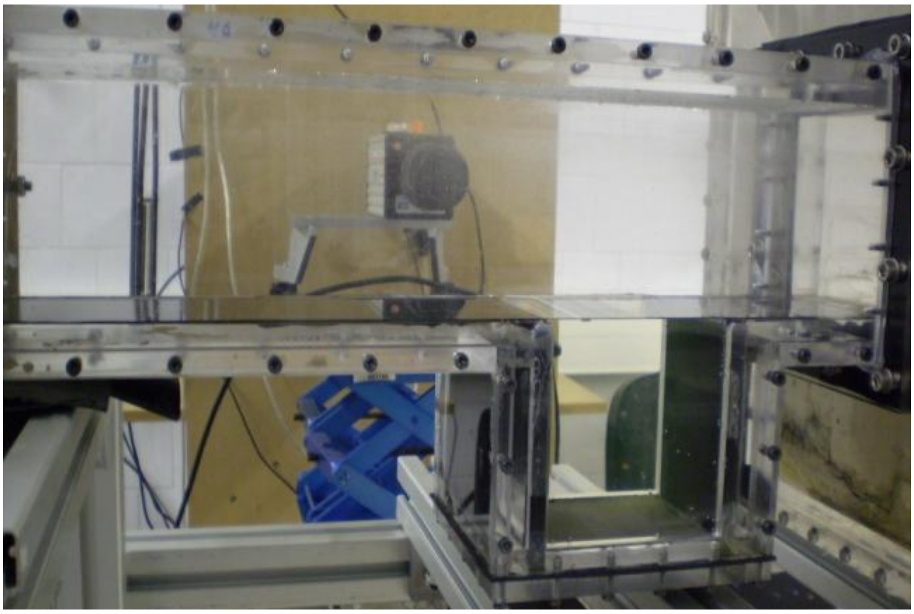

Figure 4.2: The isotherm configuration model of the cavity.

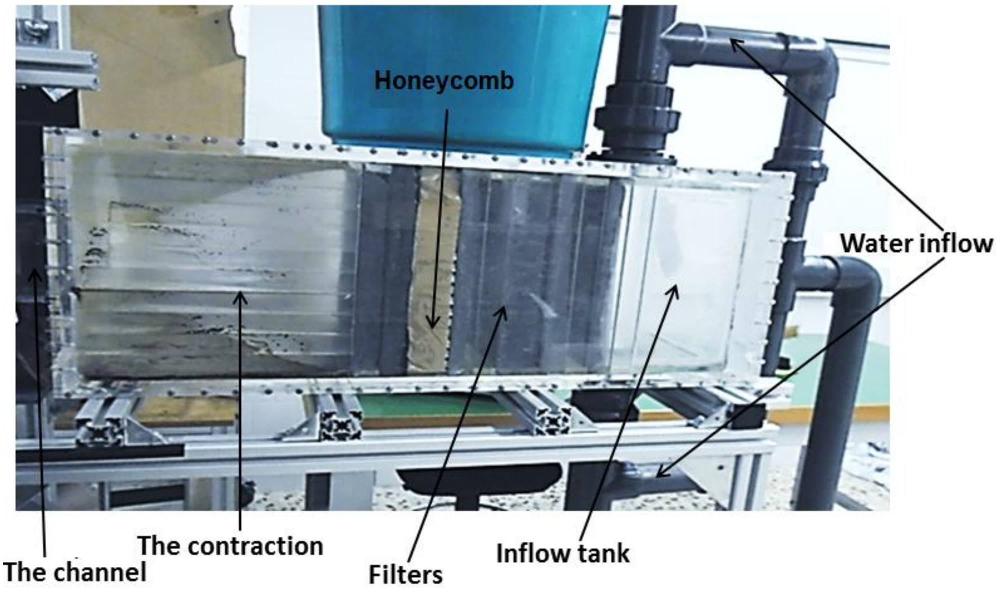

Figure 4.3: The inflow tank.

4.2. THE FLOW CYCLE

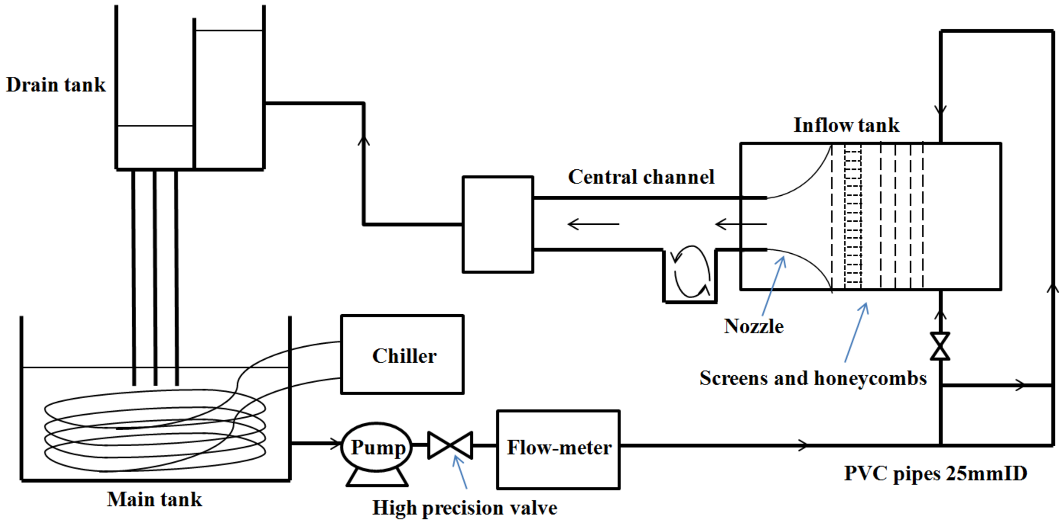

Figure 4.4: Sketch of the flow cycle.

The circulating fluid that flows through the channel is part of a closed flow system; see **Figure 4.4.** The flow is supplied by a main tank, with capacity of about 1m^3, filled with 240 liters approximately of water. A centrifugal pump type GRUNDFOS CHIE 2.3, with maximum power 0.37 kw was used (**Figure 4.5.a**). It is pumping the water to the inflow tank trough a PVC pipe (25mmID) while a flow-meter “MABECONTA S.A. MID 100” (**Figure 4.5.b**) is placed to measure the flow rate that is controlled by a high precision valve (**Figure 4.5.c**).

As explained before, the fluid enters the inflow tank by two opposite entrances to reduce undesired effects, and flow through the filters and contraction until the channel entrance, passes from one side to the other of the channel. The outflow is collected in a drain tank in a level higher than the central channel and the inflow tank to prevent the creation of the air bubbles in the flow. Finally, the water passes from the drain tank to the main tank by three tubes, which are closing the flow cycle.

The properties of water, i.e. density and viscosity, are varying with the temperature. Thus, a temperature control has become necessary to maintain a constant water temperature during each experiment. The temperature of the water is controlled using a closed circuit chiller (PolyScience 6106) shown in **Figure 4.5.d.** This chiller is controlling the temperature in a range from -10 ^{o}C to 40 ^{o}C [48]**.**

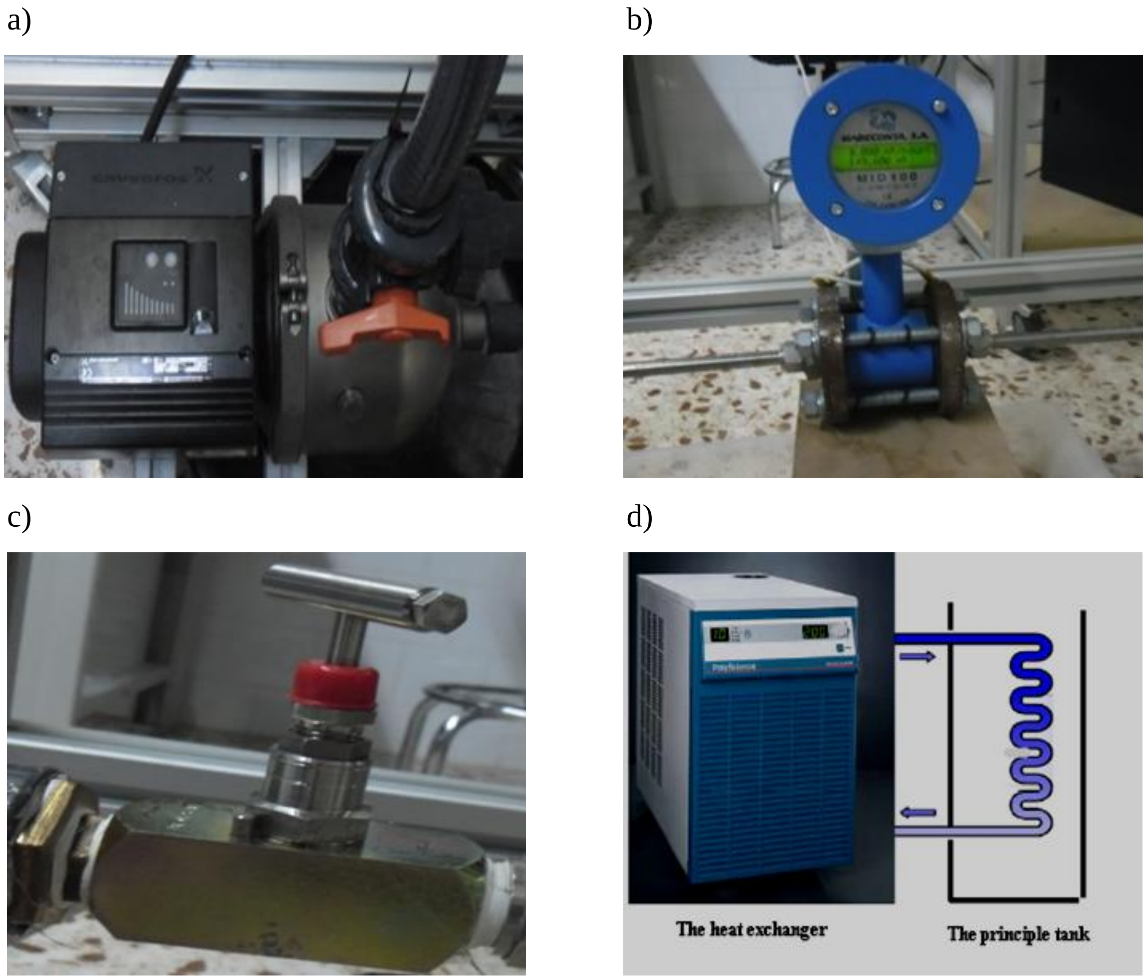

Figure 4.5: a) Centrifugal pump, b) Flow-meter, c) High precision valve, and d) PolyScience 6106chiller.

In the heated bottom configuration, the cavity bottom wall is made from cooper metal that can be heated using several thermal resistances (**Figure 4.6** and **Figure 4.7.a)**. The copper is characterized by high thermal conductivity allows a homogenous temperature distribution on the heated wall surface. The bottom walls of the channel and the cavity were painted with a black matt color in order to reduce the reflection of the laser light sheet and improve the quality of the images at the edges.

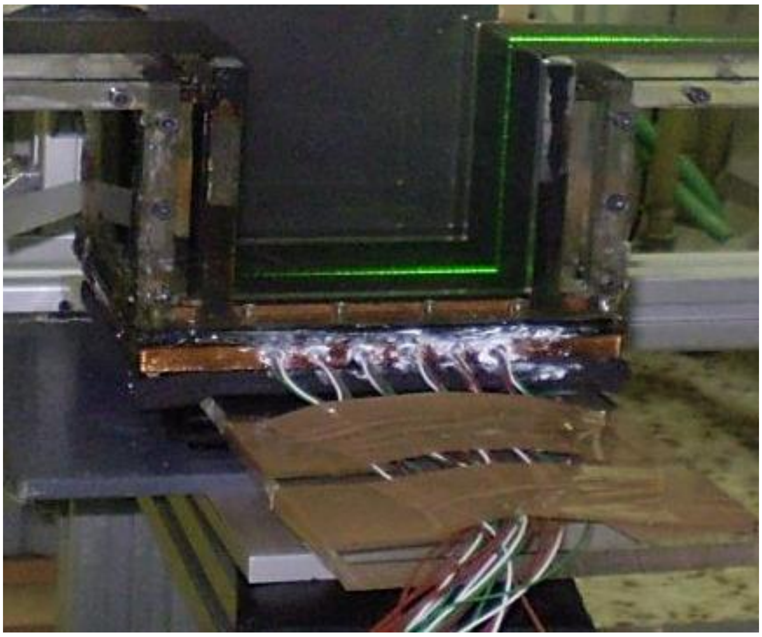

Figure 4.6: The bottom heated wall configuration model of the open cavity.

Six cartridges are used to heat the copper flat plate. Each cartridge contains a thermocouple (type “k”) and thermal resistance (2500 Ohm) capsulated in a waterproof bar 130mm length and 6.5mm diameter (**Figure 4.7.b**). The cartridges are connected with the source by 1000mm waterproof Teflon leads. The maximum power of each cartridge is 20Watt.

The cartridges were inserted in the specific holes of the copper plate (**Figure 4.6**), and connected each other in parallel using a power supply (AC current) with changeable voltage. Thermal paste was used in order to increases the thermal conductivity of the thermal interface. This thermal compound is a viscous fluid substance filling the microscopic air-gaps present due to the imperfectly flat and smooth surfaces of the components. The compound has far greater thermal conductivity than air. A thermal insulation treatment was applied for the heatable wall to avoid the effect of the direct contact with the surrounding conditions.

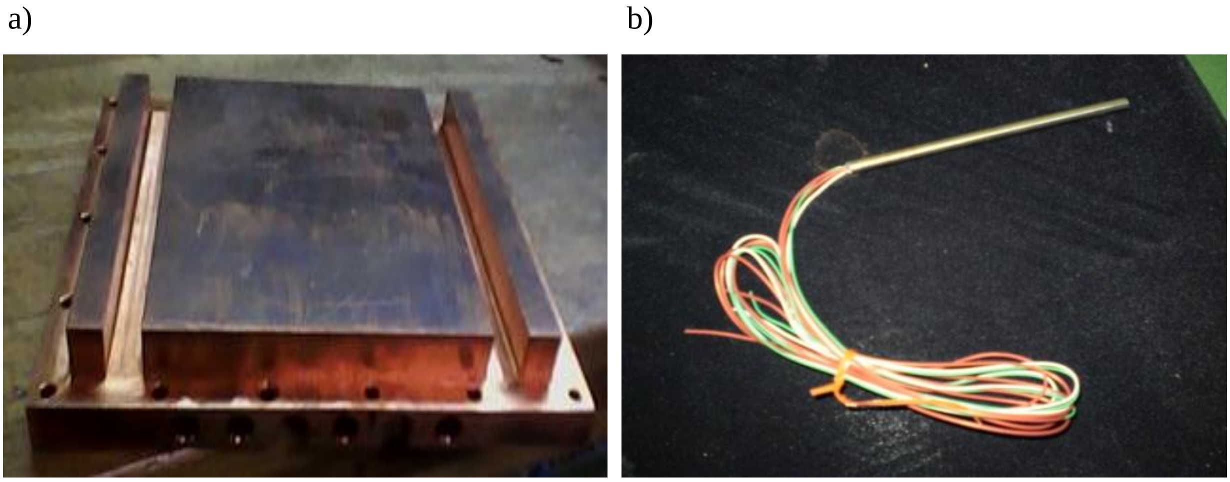

Figure 4.7: a) The cupper heated wall, and b) The cartridges.

4.3. LIGHT SOURCE AND IMAGING

Nd:Yag semi-conductor laser, “Monocrom MP532-3W” with an output power of 3W, was used in this work to generate the plane of light; see **Figure 4.8.a**. This laser is linearly polarized with 532nm wavelength and it was used in continuous mode. The laser was installed in a vertical position with a distance of 300mm over the top wall of the channel. This to illuminate the area of interest (the cavity symmetry plane), as shown in **Figure 3.1**.

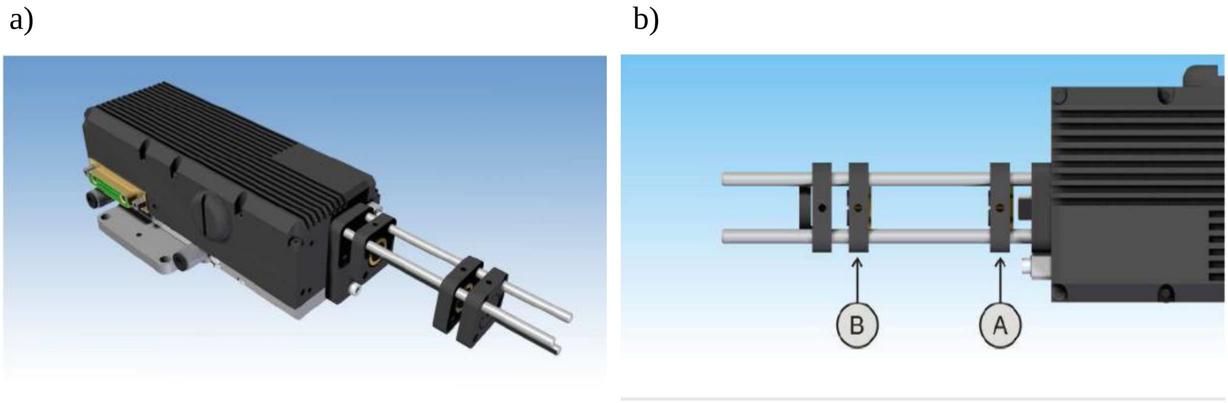

Figure 4.8: a) Laser sketch, and b) Optical system

Optical system (MP532-3W) composed of 3 lenses is mounted on the beam (**Figure 4.8.b**) in order to form and generate the required thin sheet. The first two lenses are doing beam forming while the third one generates the desired light sheet. The input condition of the laser beam before the optics is 12 mm at *x*-axis. The output condition of the laser beam after optics set is 120 mm at *x*-axis. The focus length of the 2 lenses of the focus group was 10 mm and 25 mm while the generating sheet lens has a focus length of 5 mm. The light sheet has been 1mm thick.

Figure 4.9: MotionPro HS-3 digital camera.

MotionPro digital cameras, model HS-3, has been used in the PIV recording processes (**Figure 4.9**). The sensor of the camera presents a 1280×1024 pixels resolution with square pixels 12μm. The sensitivity range is from 350 to 1000 nm. A zoom Sigma, 28-300mm F3.5-6.3 DG Macro has been used to amplify the interested regions.

Indeed, the time interval between two successive images have to be short enough so that the tracers appearing in an image also appear in the next, and long enough, to appreciate the particles movement. The time interval depends on the velocity of the fluid. In this geometry, the challenge was that the velocity inside the cavity is several times smaller than the channel velocity. In case of existence of two cameras, capturing two frames, one for the channel and another for the cavity, with same time interval can solve this problem. Identify a compromising time interval was the only solution to allow to capture these velocity in the same frame since one camera only was available in that time.

The maximum size of each image series is limited by the internal memory of the camera, which is (4Gb), and consequently measurements were recorded for 1800 images/strips. Several capturing frequencies were tested. The range between 500 fps and 10 fps were considered because at frequencies > 500fps the whole strip (1800 images) does not provide the minimum movement required for accurate analysis for the medium of the turbulent flow within the cavity. Even high capturing frequency provide an accurate results, but it decreases the exposition rate in the images beside that the whole period is limited by the capacity of the camera. Also, it was found that the accuracy becomes deteriorated and error vectors are produced due to the losses of many particle pairs in the channel at low capturing frequency than 20 fps. At the large exposition time, the particles in the channel, where the velocity is high, are moving faster and looking like traces in the images. However, a capturing frequency of 50 fps was used for extracting the mean velocities in order to get good accuracy and enough capturing period. Also, because the illumination in the images is much better when the capturing frequency is low.

According to our camera capacity, the 50 frame/Second capturing frequency allows to capture a series of images with a time length of 36 second. The number of image strips per experiment was dependent to the maximum power allowed by the laser source.

4.4. TRACER PARTICLES

Four different types of the seeding particles were tested in order to improve the PIV image quality and to satisfy seeding requirements for the considered water flow application. The four types are Lycopodium, Hollow Glass Spheres (HGS), Polyamide Seeding Particles (PSP) and Alginate-micro particles with fluorescein.

Lycopodium particles satisfy most of the seeding requirements in water. The main problem of these particles is that they are organic and they decompose leaving some dirty inside the equipment setup and its need a huge technical work to handle and clean.

Hollow Glass Spheres (HGS) are borosilicate glass particles with a spherical shape and a smooth surface. It is recommendable for liquid flow applications. Regarding to the used type of the laser and the camera we have, the appearance of the particles in the image is acceptable when the wanted plane is closed to the laser beam but it is still small enough to reflect the wanted amount of the light in other planes far away from the laser source. Only one size was available in the market at that time, which has a mean particle diameter of 10 µm, offered by DANTEC DYNAMICS.

Alginate micro particles with fluorescein imbedded have been fabricated and tested in our laboratories [49], [53] for mean diameters of 5µm, 10µm and 20µm. The main problem of these particles is the fluorescein that in some cases is dissolves in the water and reflects some undesirable light when the particles are not filtered perfectly. The group is still working in the development of these particles. Unfortunately, the rate of production of these particles does not allow us to use it in the experiments described in this work, even that their properties make them the best choice.

Polyamide Seeding Particles (PSP) has been tested (**Figure 4.10.a**). PSP offered by DANTEC DYNAMICS is producing by polymerization processes and therefore has a round but not exactly spherical shape. These micro-porous particles are highly for water flow applications. Finally it was found that the optimum type for our case is polyamide seeding particles with a mean particle diameter of 50 µm (**Figure 4.10.b**) as its size is large enough to reflect the required amount of the light sheet and overcome the decomposition problems since the PSP is not organic.

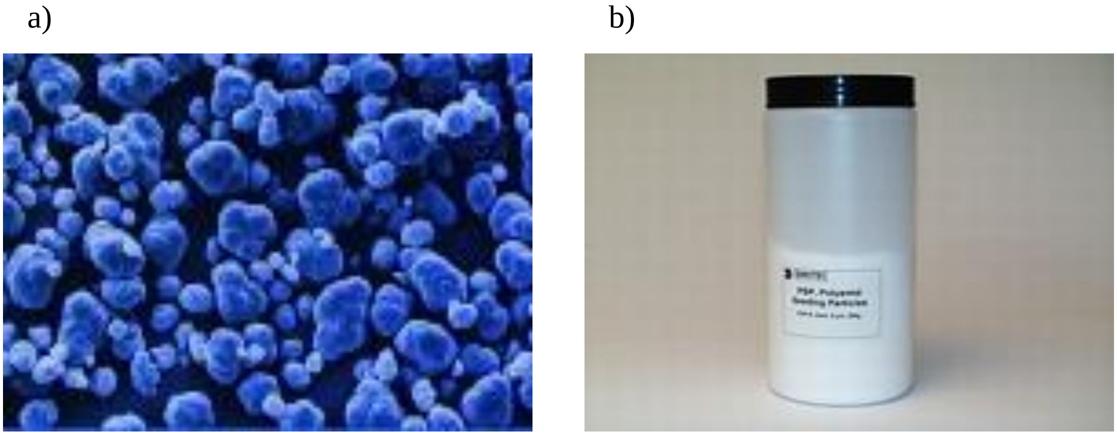

Figure 4.10: Polyamide Seeding Particles with a mean particle diameter of 50 µm.

4.5. EXPERIMENTATION CHALLENGES

Some challenges were found during the experiments. The equipment model was not fully symmetric. This produces an asymmetric inflow condition. The effects of the asymmetric inflow condition on the steadiness and the vortex location in the cavity are discussed in section 6.3.

A significant fluctuation becomes fact at low flow rates because the minimum pump force is higher than the required. This makes a high pressure close to the high precision valve. Due to the inconstant inflow condition, the steady state never realized experimentally. The results were more accurate for high flow rates. However, due to these constraints, the Reynolds number considered experimentally is $Re \geq 1000$ for both configurations.

The fluid flows through the equipment about an hour before any capturing in order to:

- Stabilize the flow cycle.
- Inhibit the possibility of bubbles creation in the fluid flow.
- The flow cleaning the walls from the pasted up tracer particles from previous experiments, which can make noise in the images.
- To let the particles distributed homogeneously over the light sheet.

CHAPTER 5

Air flow analysis/discussion

In this chapter, we discuss the numerical simulation results of the air flow. The obtained results are discussed in terms of in streamlines, velocity components and isotherms. Different planes are presented to reveal different aspects of the fluid flow structure and the mixed convection effects on the stability of the flow in three dimensions. Isothermal configuration and cavity with the bottom wall heated configuration were applied for Re≤1500.

The isothermal configuration concept is that no heat transfer occurs and all the walls have a no-slip condition. Undoubtedly, the flow in the isothermal configurations is governed by the continuity and the momentum equations. Indeed, the isothermal configuration is only proceeded to check the flow steadiness before studying the effect of heating the bottom wall of the cavity.

The cavity with the bottom wall heated configuration, the bottom wall of the cavity is heated by a uniform temperature while the rest of the walls are adiabatic. Consequently, this configuration is governed by the continuity, the momentum and the energy equations. The range of the Richardson number applied for this configuration is Ri≤10. The studied cases for each configuration are shown in **Table 5.1**.

Table 5.1. List of the air flows' cases

Isothermal configuration	
Re	No heat transfer occurs
100	
500	
1000	
1500	
Heated bottom configuration	
Re	***Ri***
100	0.001, 0.01, 0.1 , 1.0 and 10.0
500	
1000	
1500	

5.1. ISOTHERMAL CONFIGURATION

The simulation of the isothermal configuration was implemented before the cavity with the bottom wall heated configuration to check the flow steadiness in this range of Reynolds number in case of no heat transfer process occurring. The fluid flow in the cavity and the channel were studied at different inflow Reynolds number (Re=100, 500, 1000 and 1500). As a result of the small Re≤1500, the flow is laminar and steady for all cases.

In all the studied cases of the different Reynolds number, for the isothermal configuration, a fixed phenomenon was found. The existence of a primary recirculation cell structure inside the cavity which is similar to the flow structures found in a lid driven cavity [5], [6], [8], [18], [20], [23], [25].

Figure 5.1 presents the streamlines for Re=100, Re=500, Re=1000 and Re=1500, respectively. The steady state is reached in all these cases. The recirculation cell center of the structure inside the cavity in case of Re=100, is located in the higher part of the cavity at x^*=1.55 and y^*=0.72, which is close to the cavity vertical centerline. Increasing the Reynolds number increases the inertia of the flow and consequently the recirculation cell center is moving slightly down within the cavity.

A small secondary recirculation region appears in the downstream right corner of the cavity at Re≥1000, which becomes more evident by increasing Reynolds number. However, the main conclusion of the isothermal configuration is that the flow is laminar and steady for all cases at Re≤1500.

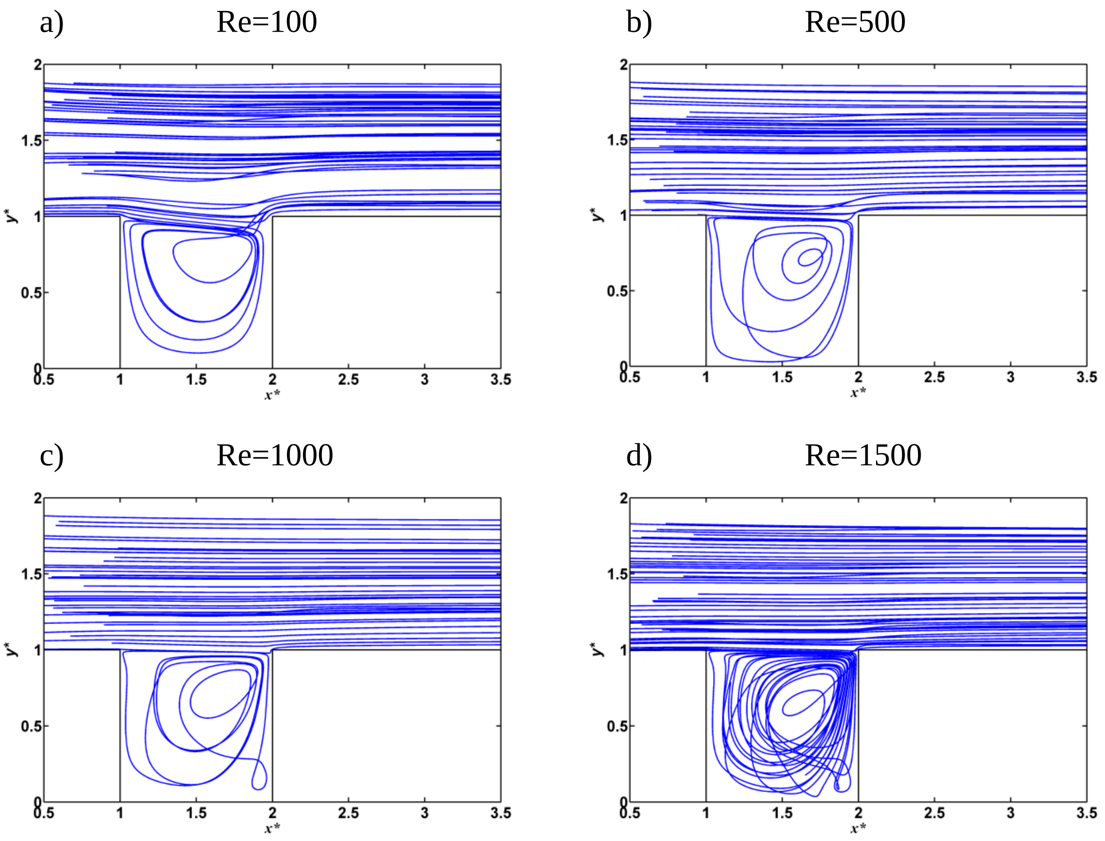

Figure 5.1: The flow structure for a) Re=100, b) Re=500, c) Re=1000 and d) Re=1500.

5.2. CAVITY WITH HEATED BOTTOM WALL CONFIGURATION

In the cavity with heated bottom wall configuration, the cavity bottom wall heated by a uniform temperature T_H, while all the rest of the walls are adiabatic. The flow stability and its structure are not dependent only on the Reynolds number (Re) as for the isothermal configuration. The effect of the Reynolds number on the stability of the flow and its flow structure is varying influenced by the buoyancy forces contributed in the mixed convection according to the value of Richardson number ($Ri=Gr/Re^2$). The Reynolds numbers considered in this study are 100, 500, 1000 and 1500. For each value of the Reynolds number, we considered five values of Richardson number (Ri=0.001, 0.01, 0.1, 1 and 10).

Temperature distributions on the vertical symmetry plane of the computational domain (**Figure 5.2**) are presented for some cases along the flow streamlines to analyze the flow structure and the effects of the mixed convection. Other planes in *x-z* and *y-z* directions are presented for some interested cases to reveal different aspects in three dimensions. The heated wall has a dimensionless temperature equal to 1, and the air inflow temperature is equal to 0, while the increment between the temperature contours in the figures is equal 0.025.

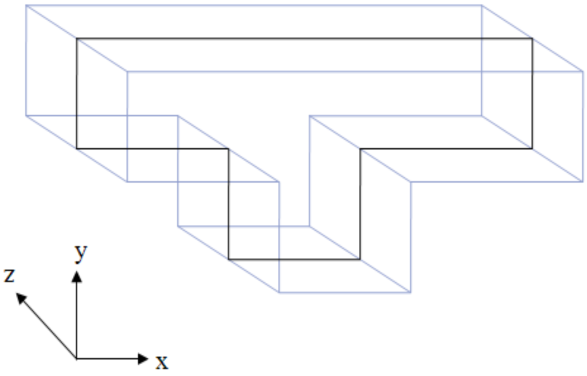

Figure 5.2: Streamwise symmetry plane.

In all cases of this configuration, a fixed phenomenon is noted which shows that no significant change in the cases of (Ri=0.001−0.01) for the different values of Reynolds numbers understudy; see **Figure 5.3.** As shown, the flow structure and the temperature distribution on the vertical symmetry plane of the computational domain are similar. Also, the flow structure in that small Richardson number is similar to that found in the isothermal configuration. This means that for small $Ri \leq 0.01$, the effect of the buoyancy is not significant.

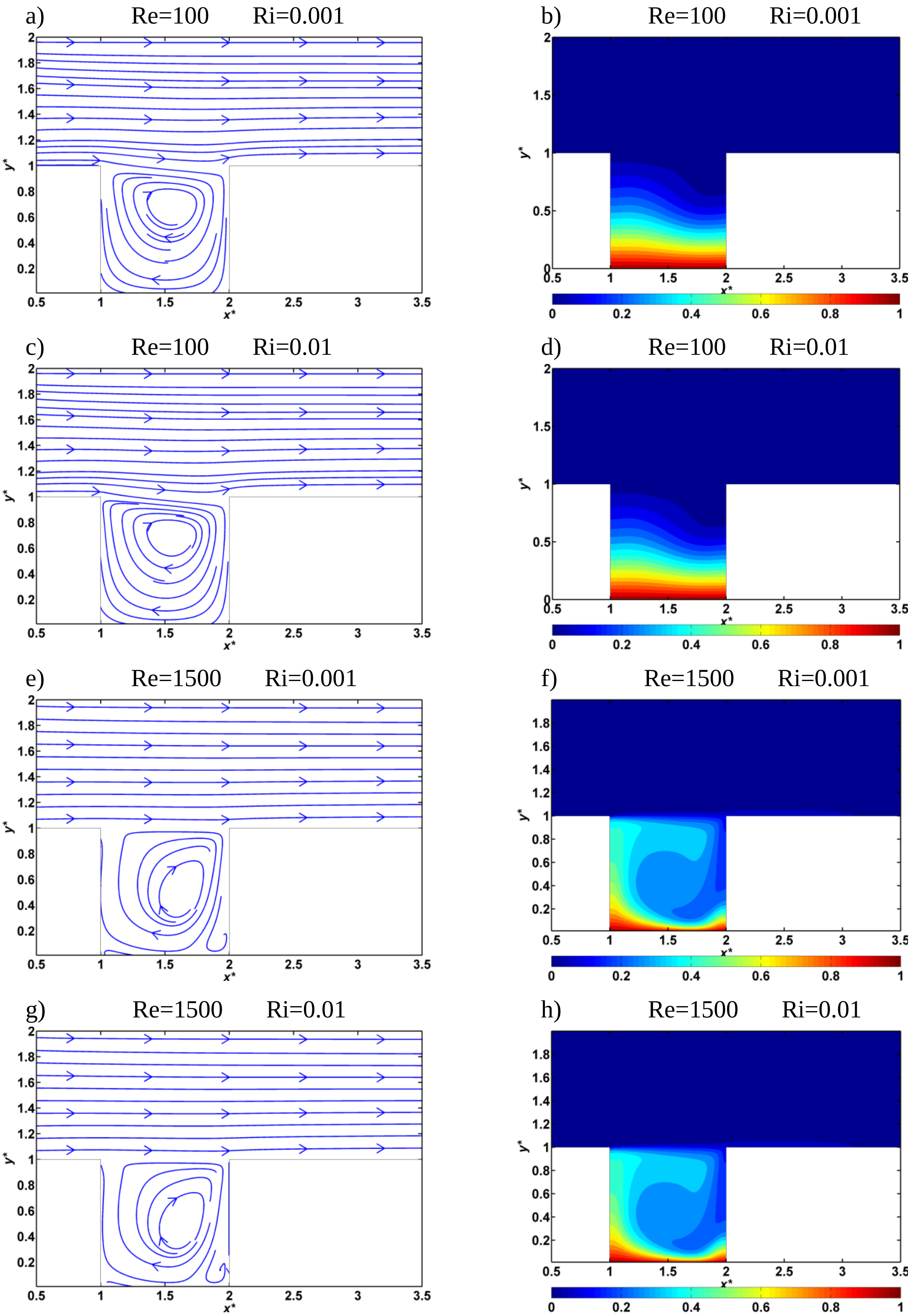

a) Re=100 Ri=0.001

b) Re=100 Ri=0.001

c) Re=100 Ri=0.01

d) Re=100 Ri=0.01

e) Re=1500 Ri=0.001

f) Re=1500 Ri=0.001

g) Re=1500 Ri=0.01

h) Re=1500 Ri=0.01

Figure 5.3: Comparison between the flow structure and temperature distribution for Ri=0.001 and Ri=0.01 at different Reynolds number.

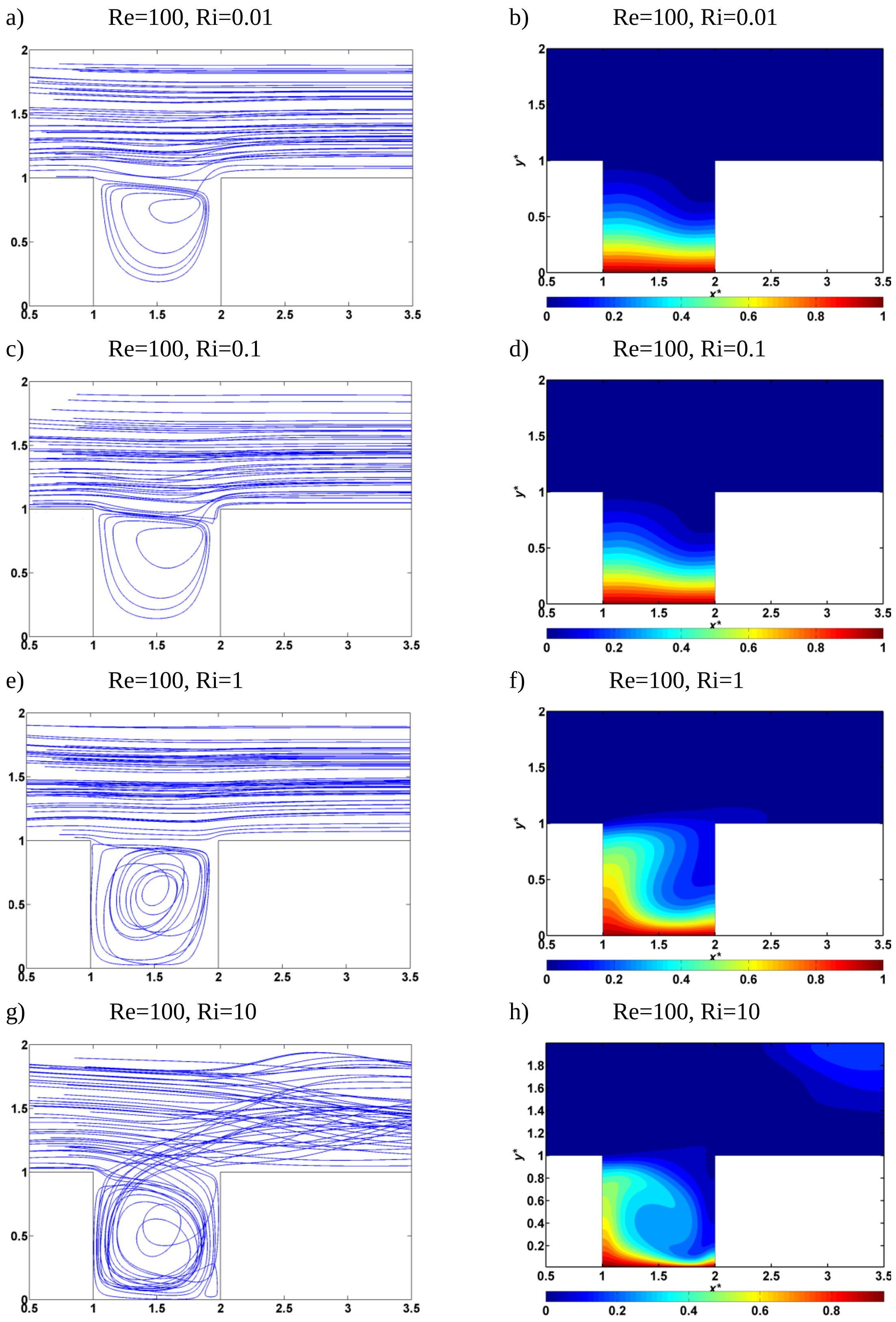

a) Re=100, Ri=0.01

b) Re=100, Ri=0.01

c) Re=100, Ri=0.1

d) Re=100, Ri=0.1

e) Re=100, Ri=1

f) Re=100, Ri=1

g) Re=100, Ri=10

h) Re=100, Ri=10

Figure 5.4: Streamlines and temperature distribution for Re=100.

Figure 5.4 demonstrates the results for Re=100, for different values of Ri=0.01, 0.1, 1 and 10. At Ri=0.01and 0.1 (**Figure 5.4.a-b** and **Figure 5.4.c-d**, respectively), the flow is steady. The recirculation center is located near the top of the cavity. The effect of the buoyancy force is very small as shown in the temperature profile. The temperature contours are parallel and clustered closed to the heated wall at Ri≤0.1, where the conduction mechanism is dominant.

At Ri=1, (**Figure 5.4.e-f**), the recirculation center moves down slightly and it is located closed to the center of the cavity, while the buoyancy force becomes more effective on mixed convection. At Ri=10, **Figure 5.4.g-h** shows that the recirculation center moves to the lower half of the cavity. The temperature distribution shows that the contribution of the buoyancy forces is higher than previous cases and pushes the flow upstream slightly. The temperature contours exceed the top of the cavity and affects the outflow region.

At Re≥500, for all values of Ri, the temperature distribution exceeds the top of the cavity; see **Figure 5.5** to **Figure 5.7**. At Re=500 and Ri≤0.1 (**Figure 5.5.a-d**), the flow is steady and the effect of buoyancy is small as indicated by the isotherms. The flow in the cavity rises up affected by the heated wall and incorporating with the recirculation cell.

The increase of Richardson number produces unsteady flow influenced by an increase of the buoyancy force. The time average temperature distributions in (**Figure 5.5.e-h**) show that, the buoyancy pushes the flow upstream and enhances the recirculation flow. A small eddy in downstream corner is presented at the bottom of the cavity in both cases of Ri=1 and 10.

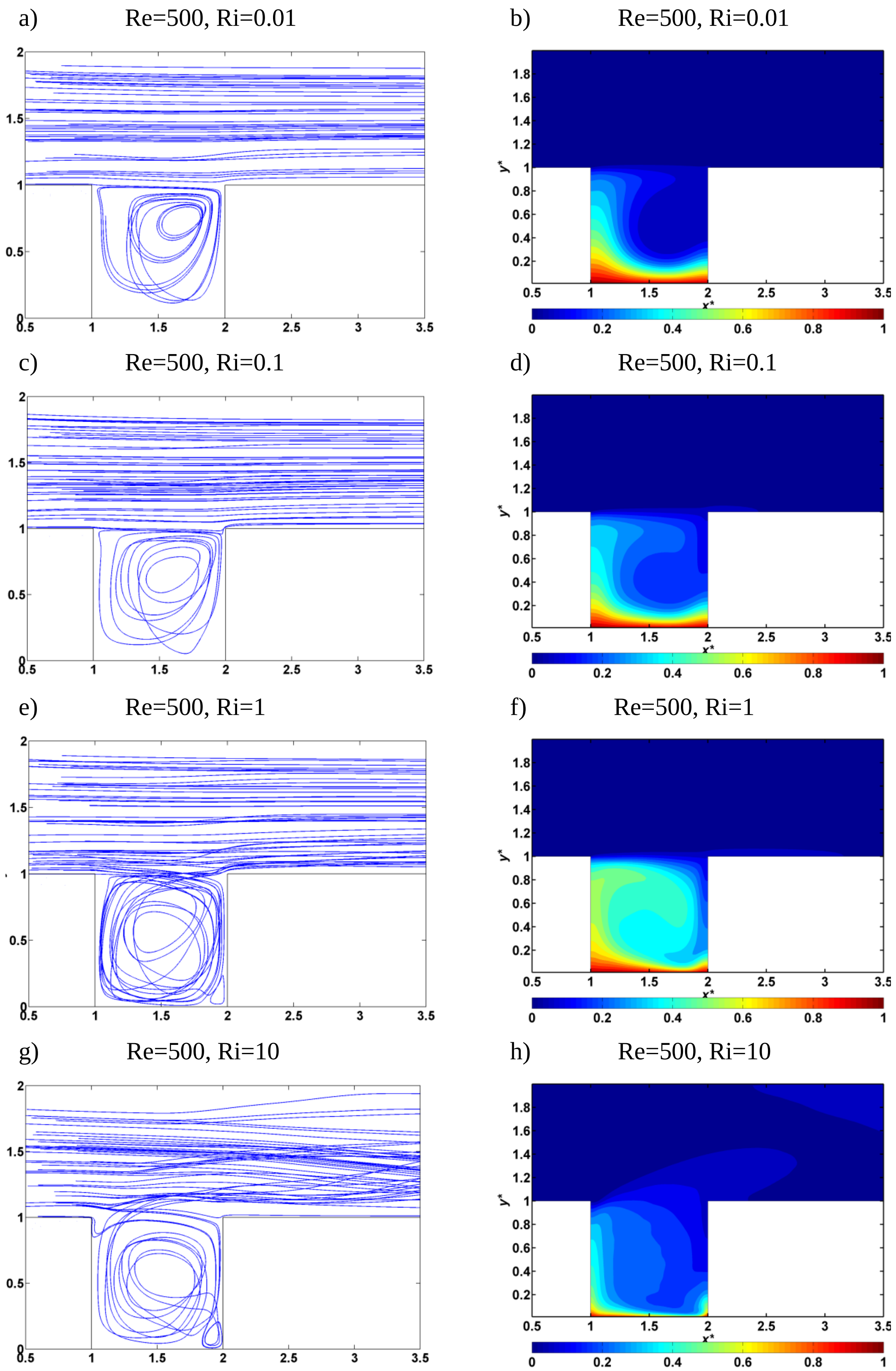

Figure 5.5: Streamlines and temperature distribution for Re=500.

At Re=1000, the flow is steady only for low values of Ri (Ri≤ 0.1). At Ri≥1, the flow becomes unsteady. Consequently, the air flow in the cubical heated bottom wall cavity loses the steadiness at Re≥500 with Ri≥1. **Figure 5.6.a-d** depicts the cases for Re=1000, at Ri=0.01 and 0.1 respectively. The temperature distribution is clustered towards the heated wall and the left vertical wall of the cavity.

At Ri≥1 and Re=1000, the flow is unsteady. The time average velocities show that the main recirculation cell grows to fill most of the cavity volume. **Figure 5.6.c-d** and **Figure 5.6.e-f** show the time averaged flow structure in streamlines and the time averaged temperature distribution for Re=1000 with Ri=1 and Ri=10, respectively. In case of Ri=1, the temperature distribution reaches to the lower part of the outflow opening (**Figure 5.6.f**). At Ri=10 (**Figure 5.6.h**), the temperature distribution affects the outflow indicating that heat transfer strongly effected by convection.

At Re=1500 and Ri=0.01 (**Figure 5.7.a**), the flow structure is similar to the one presented in **Figure 5.6.a**. The increase of the inertia by increasing the Re enhances the vortex velocities. This moves the recirculation cell center slightly lower.

For Re=1500 and Ri≥0.1 (**Figure 5.7.c-h**), the flow is unsteady moving complex in the three-dimensions. In the vertical symmetry plane, the main recirculation cell grows and fills most of the cavity volume. A small eddy appears in the downstream right corner. It has been noted that, the effect of buoyancy in such high Ri has a strong contribution in the mixed convection since it enhances recirculation cell by pushing the cavity fluid upstream from the left side of the cavity.

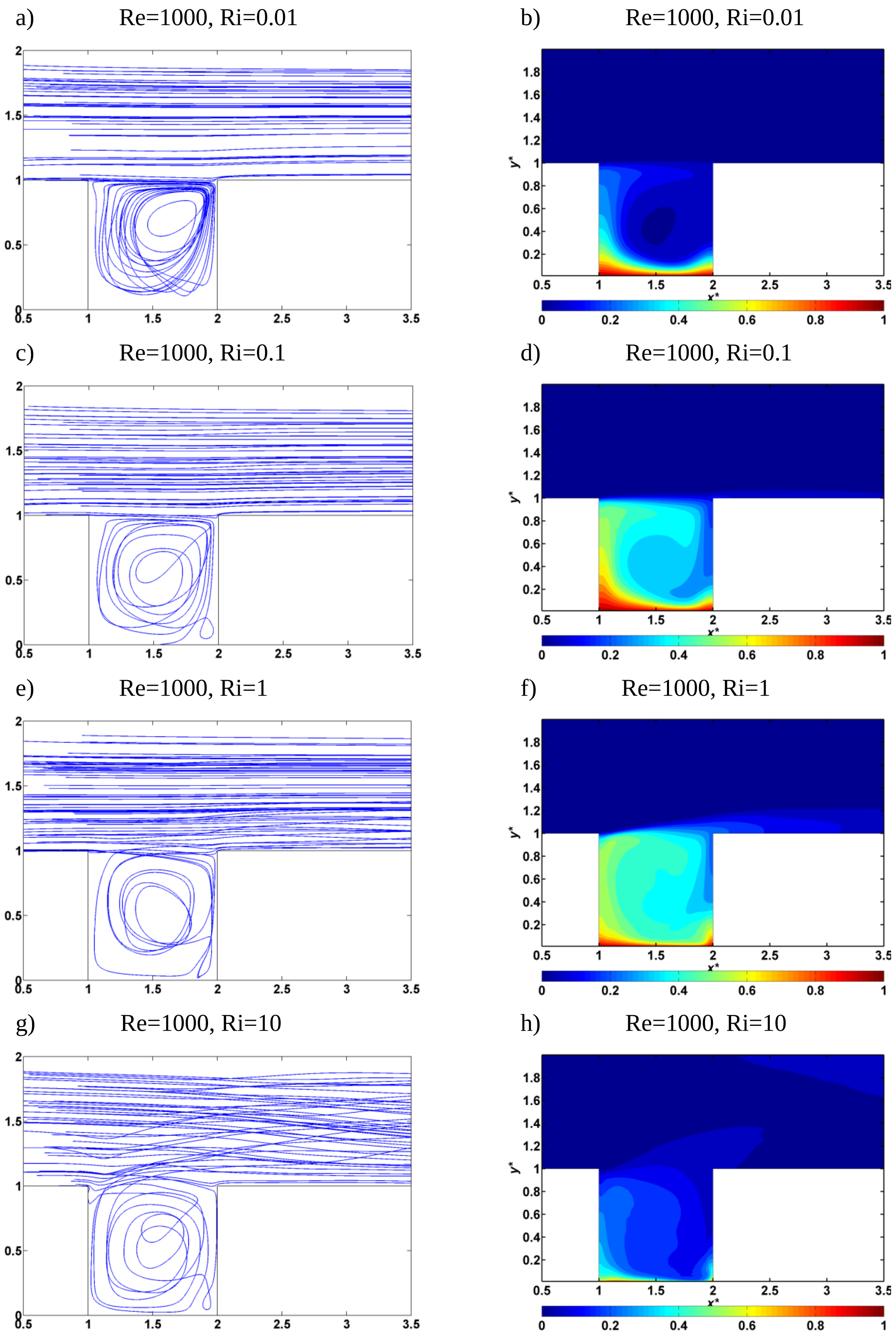
a) Re=1000, Ri=0.01
b) Re=1000, Ri=0.01
c) Re=1000, Ri=0.1
d) Re=1000, Ri=0.1
e) Re=1000, Ri=1
f) Re=1000, Ri=1
g) Re=1000, Ri=10
h) Re=1000, Ri=10

Figure 5.6: Streamlines and temperature distribution for Re=1000.

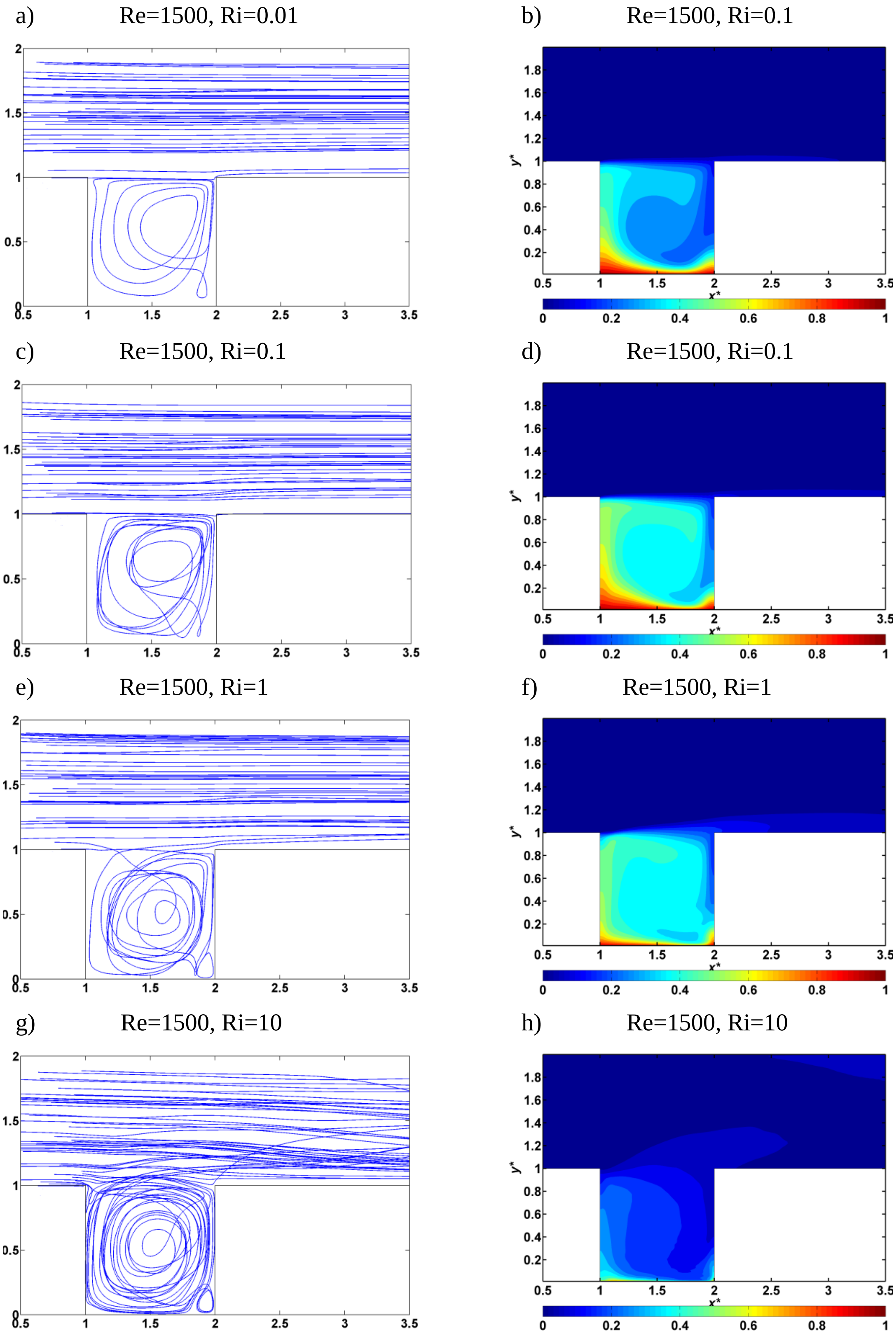

Figure 5.7: Streamlines and temperature distribution for Re=1500.

To illustrate the difference between the instantaneous flow structure and the time average flow structure approach, **Figure 5.8.a** and **Figure 5.8.b** show an example of the instantaneous and the time average flow structure in the vertical symmetry plane for Re=1500 and Ri=10, respectively.

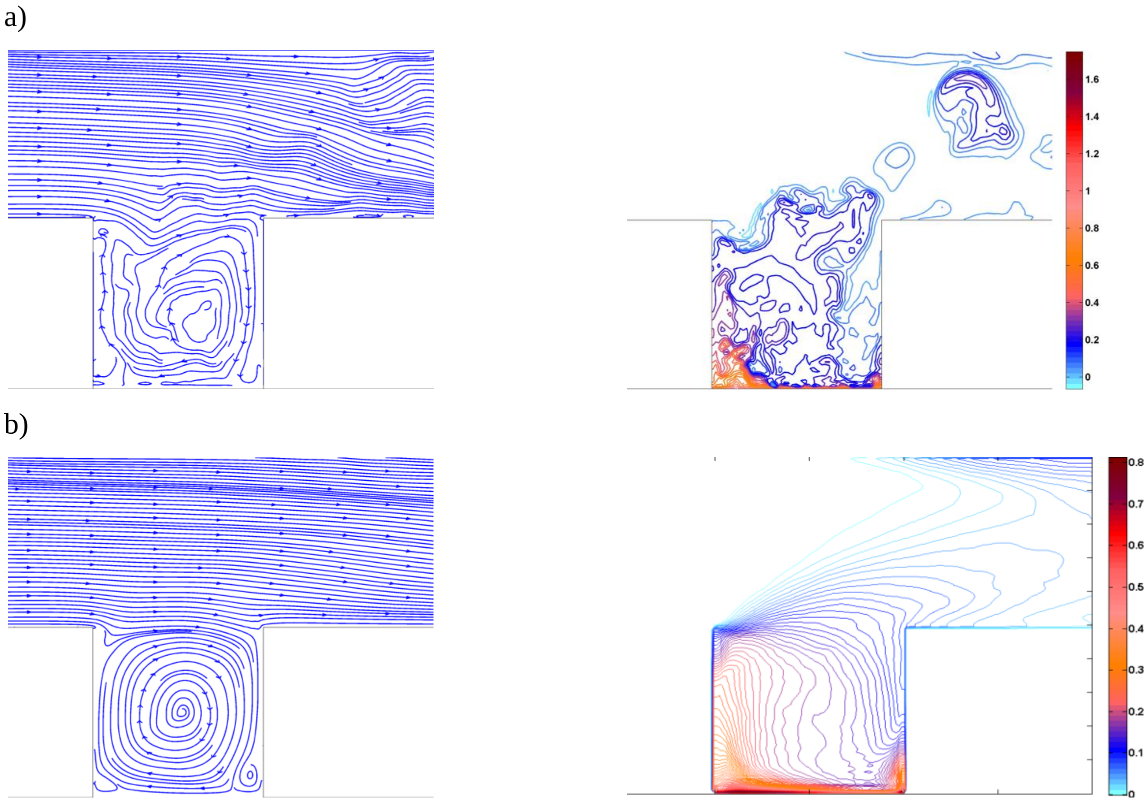

Figure 5.8: a) Instantaneous flow structure and b) Time average flow structure at Re=1500 with Ri=10.

The time evolution deemed to be one of the calibrators of the computational simulations. It is also defining if the flow is steady or unsteady. As an example of the flow unsteadiness, the evolution of the velocity u^* acting in *x*-direction at (x^*=1.2, y^*=0.5 and z^*=0.5), which is located in the symmetry plane close to the leading vertical wall of the cavity, is shown in **Figure 5.9.a**. The evolution of the *y*-component of the velocity (v^*) at the same point is shown in **Figure 5.9.b**. On the other hand, the time evolution of the spanwise velocity component (w^*) at the point (x^*=2.2, y^*=1.2 and z^*=0.5), which is located in the channel near the top trailing edge of the cavity is shown in **Figure 5.9.c**.

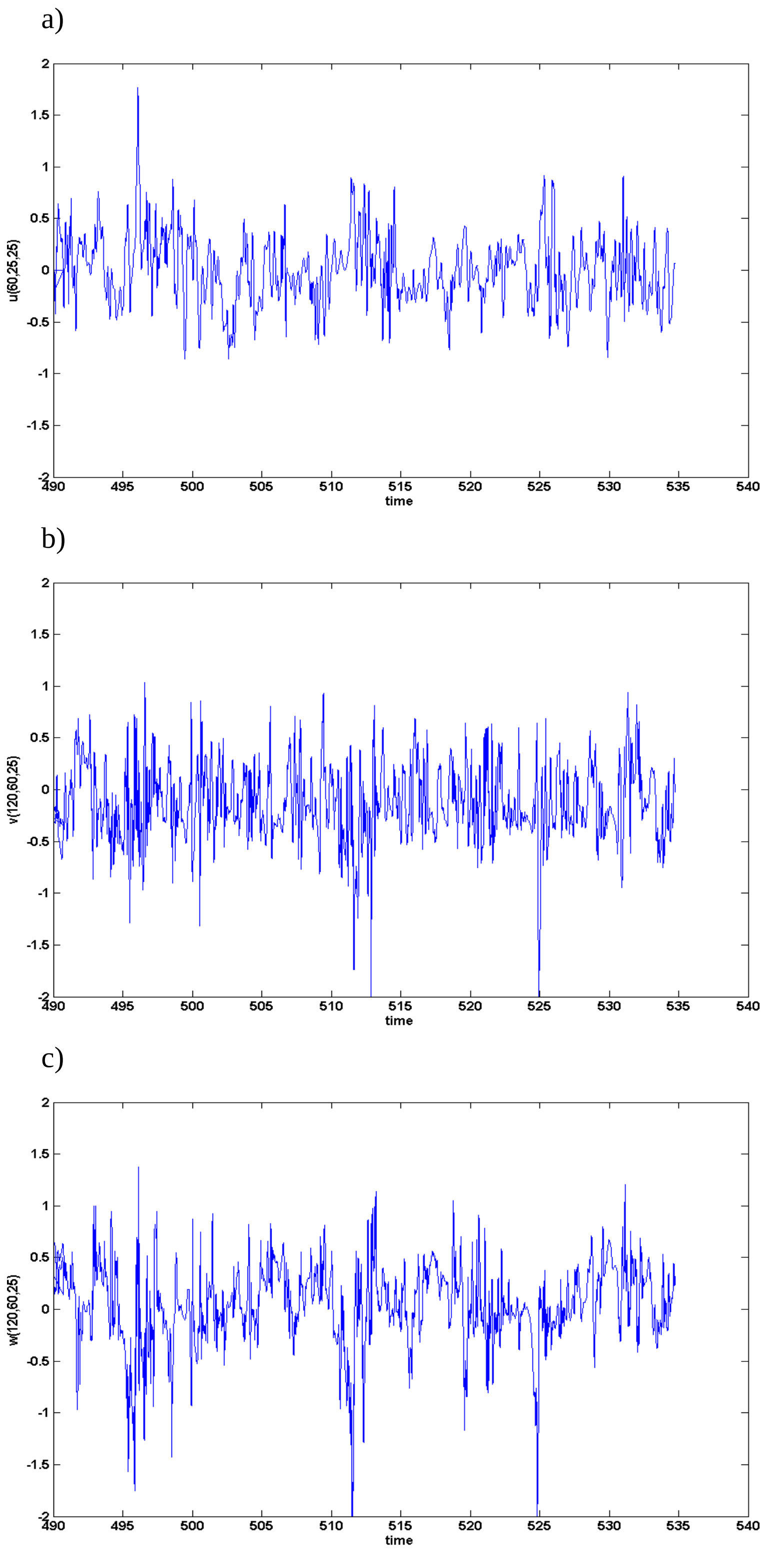

Figure 5.9: Instability of velocity of the a) u^* at $x^*=1.2$; $y^*=0.5$; $z^*=0.5$, b) v^* at $x^*=1.2$; $y^*=0.5$; $z^*=0.5$, and c) w^* at $x^*=2.2$; $y^*=1.2$; $z^*=0.5$.

Figure 5.10 draws the root mean square (rms) between the instantaneous and average velocities for the component (u^*) at the cavity centerline of the streamwise symmetry plane. The maximum rms is equal to 0.54.

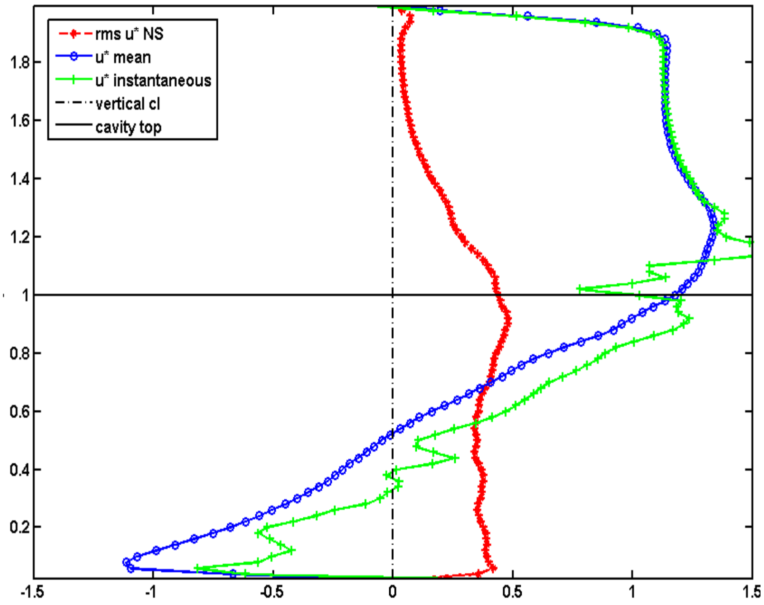

Figure 5.10: The rms of the u^* velocity component in the cavity vertical centerline of the streamwise symmetry plane.

In order to study the effect of varying the Richardson number on the velocity of the flow within the cavity, comparisons between the mean v^* velocity component at the cavity centerline of the streamwise symmetry plane for Re=1000 and 1500 with different Ri are shown in **Figure 5.11** and **Figure 5.12**, respectively.

The figures indicate that at low Richardson number in ranges $Ri \leq 0.01$, the difference between the results of the velocity component v^* is not important since the small effect of buoyancy at these values of Ri; see the temperature contours depicted in **Figure 5.6.a** and **Figure 5.7.a**.

At $Ri \geq 0.1$, the buoyancy becomes more effective since it pushes the flow within the cavity upward to enhance the recirculation flow. This can be noted from the differences between the velocities shown at **Figure 5.11** and **Figure 5.12**.

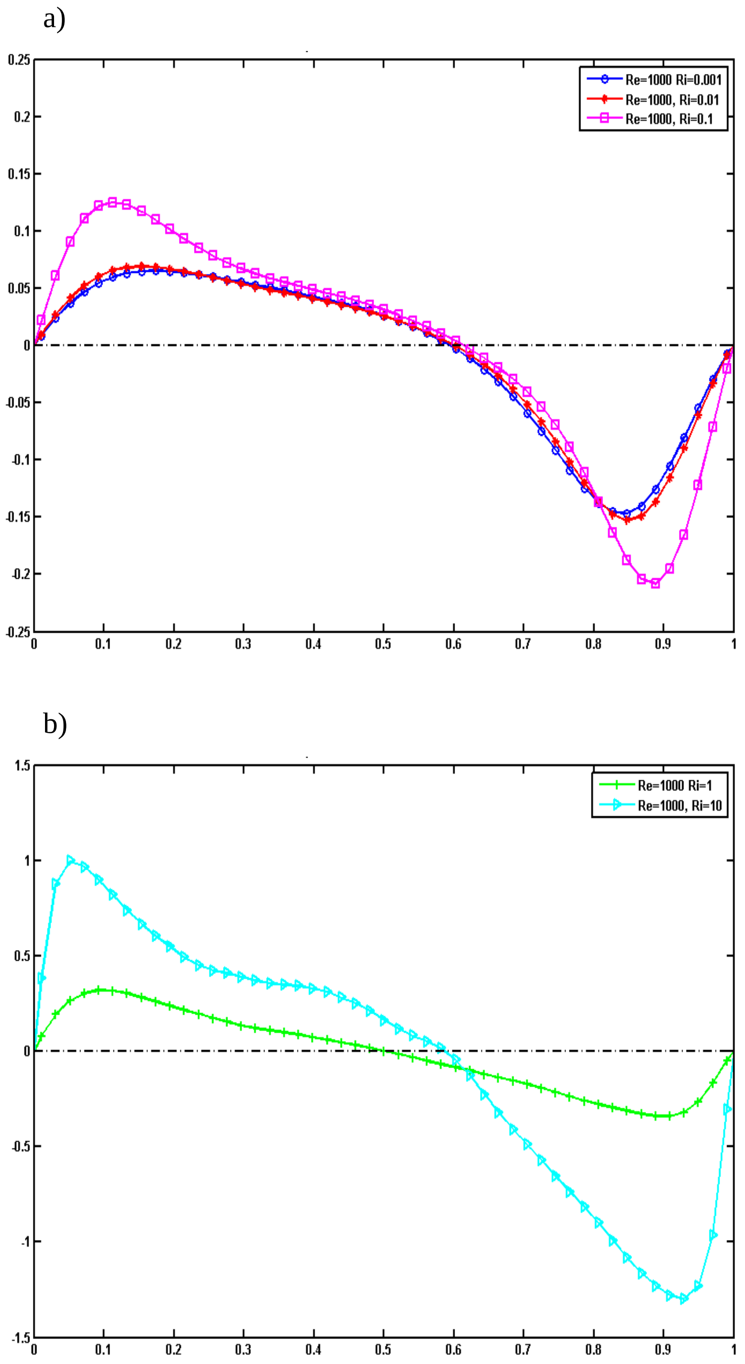

Figure 5.11: v^* mean velocity component for Re=1000 with different Ri, at the cavity centerline of the streamwise symmetry plane.

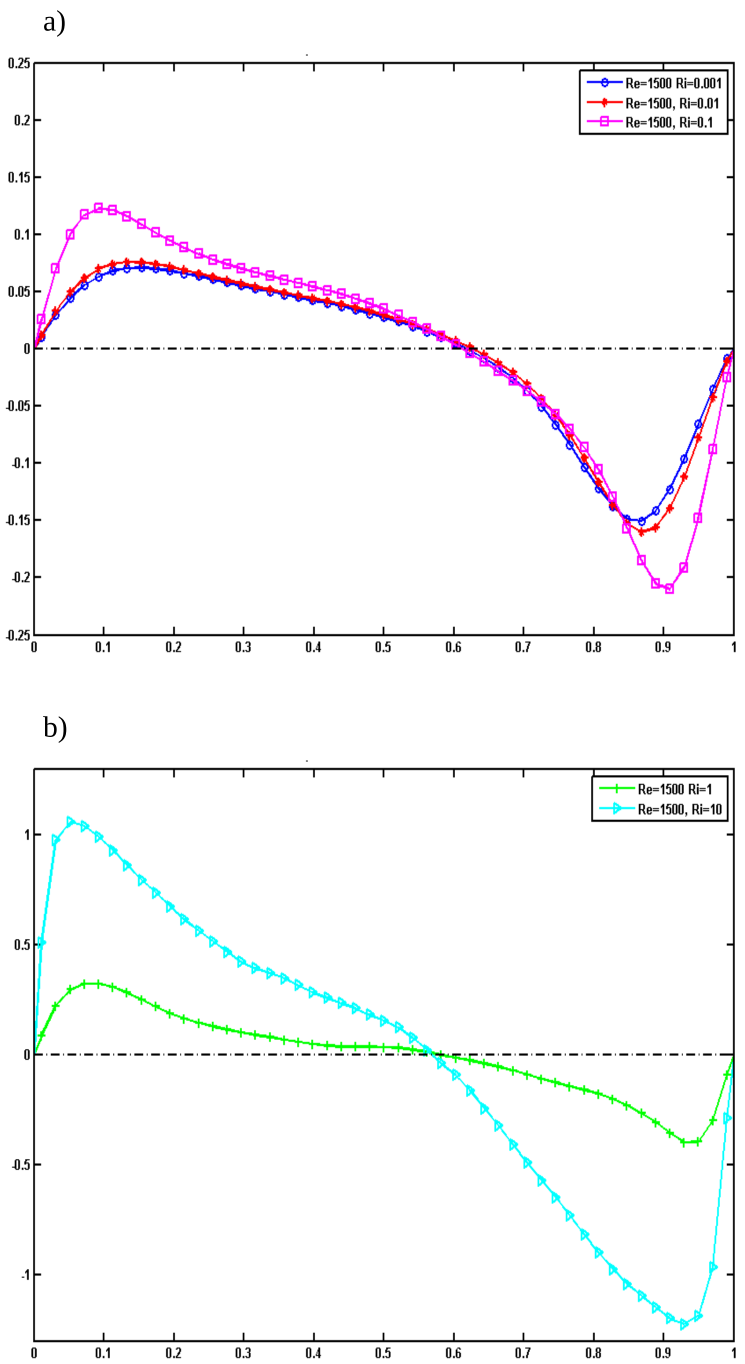

Figure 5.12: v^* mean velocity component for Re=1500 with different Ri, at the cavity centerline of the streamwise symmetry plane.

Figure 5.13 and **Figure 5.14** show the mean velocity component u^* for Re=1000 and Re=1500, respectively, with different Ri, at two different positions on the symmetry plane. These figures also confirm the small effect of such small Richardson number in ranges

Ri≤0.01, since the results tend to match each other's. A small difference occurred at Ri=0.1, due to the enhancement of the recirculation cell velocities by the buoyancy.

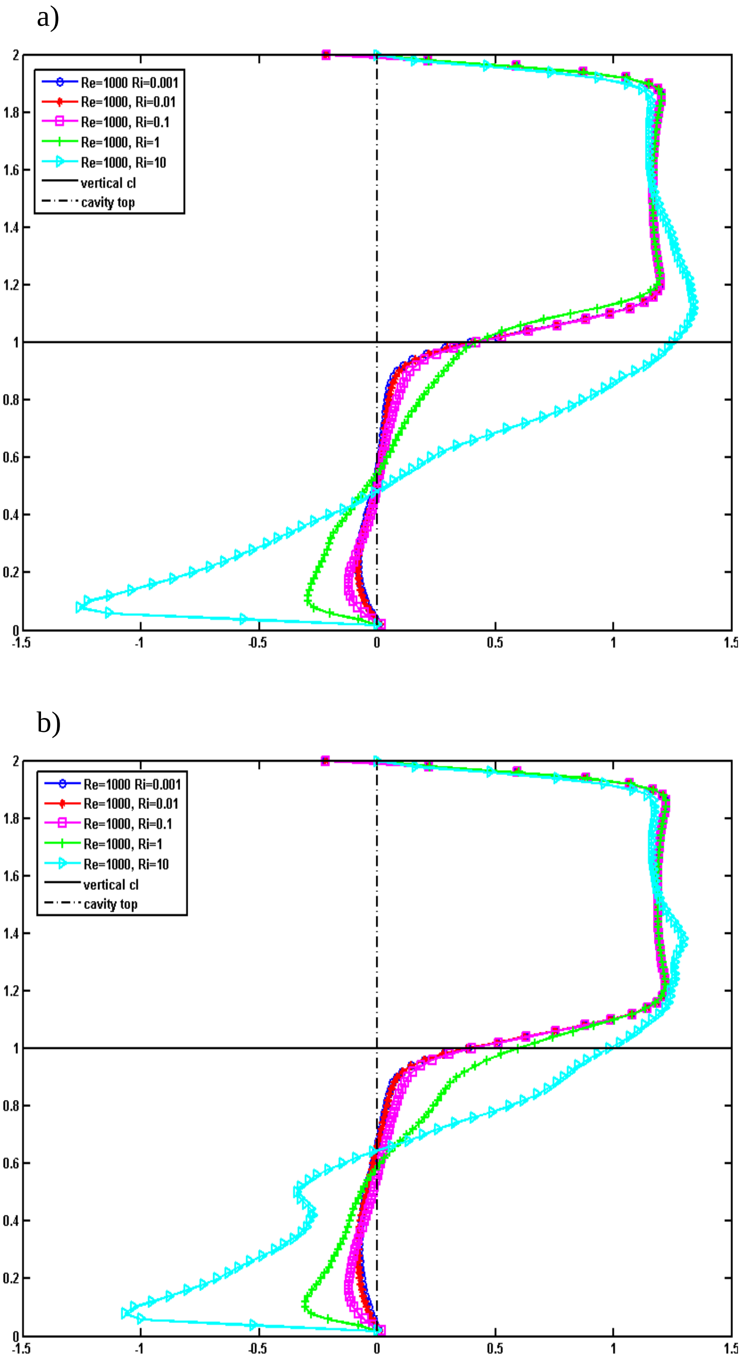

Figure 5.13: u^* mean velocity component for Re=1000 with different Ri, at different positions on the streamwise symmetry plane a) u^* at x^*=0.33 and b) u^* at x^*=0.66.

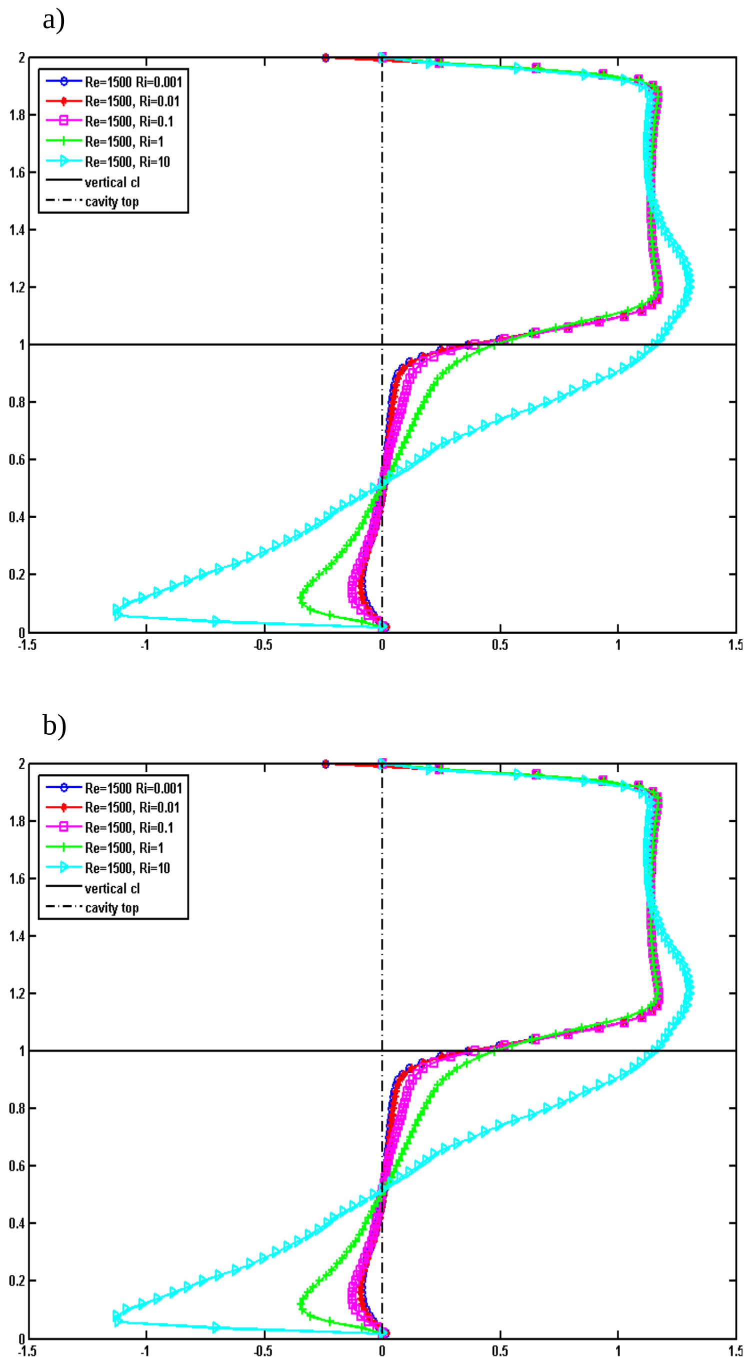

Figure 5.14: u^* mean velocity component for Re=1500 with different Ri, at different positions on the streamwise symmetry plane a) u^* at x^*=0.33 and b) u^* at x^*=0.66.

The velocity components u^* and v^* are extremely increased in comparison with at low Ri≤0.1; see **Figure 5.11** to **Figure 5.14**. It is obvious that the effect of buoyancy is high enough to induce the fluid to rise up from the left side of the cavity enhancing strongly the main vortex velocities in both streamwise and the transverse direction.

The three-dimensional structures for the steady and the unsteady and the flow evolution with time are described in details in *Chapter 6*. The average Nusselt number at the heated wall is calculated. **Figure 5.15** depicts the average Nu with Ri for cases Re=100, 500, 1000 and 1500. Nusselt number increase with Ri for each value of Re. When Ri is low, the buoyancy is weak. Thus, the effect of the natural convection is low in the transport mechanism and the convective effect is dominated. The Nusselt number increases strongly at higher values of Ri, and this reveals that natural convection is dominant.

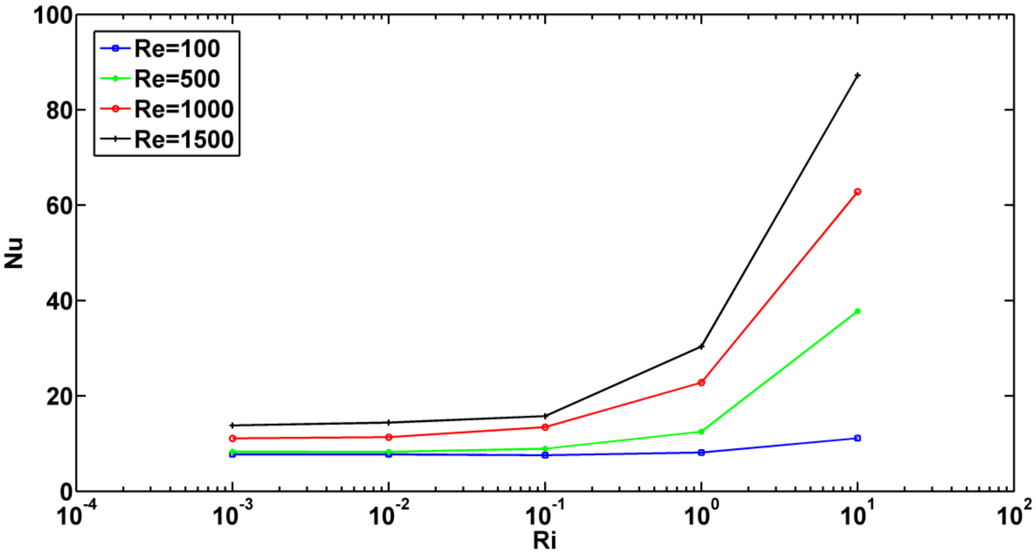

Figure 5.15: Average Nusselt number.

CHAPTER 6

Water flow analysis/discussion

In this chapter, the numerical and experimental results of the water flow are explained. The experimental study has been performed to authenticate the numerical results. In the simulations, the effect of temperature dependent physical properties was considered.

6.1. TEMPERATURE DEPENDENT PHYSICAL PROPERTIES

The effect of temperature dependent expansion coefficient of water has been studied numerically because the temperature dependent physical properties has not been previously considered in literature for this property in this range of Re and Ri. **Figure 6.1**, shows a comparison between the u^* and v^* velocity components in the vertical (**Figure 6.1**.**a**) and horizontal (**Figure 6.1**.**b**) centerlines of the cavity symmetry plane. These figures show the velocities comparison at Re=1500 with Ri=10, which is the most sensitive case in the range understudy. The triangles indicate the velocity components at constant expansion coefficient. The cycles indicate the velocity components at temperature dependent expansion coefficient.

It can be observed from the comparison that the variation of the thermal expansion does not affect the flow topology. The difference in the average Nusselt is less than 5%. Consequently, by merging this result of the temperature dependent expansion coefficient with the other temperature dependent fluid properties of [32], [33] we conclude that the temperature dependent fluid properties is not affecting the structure of the water flow in the specific range of Re and Ri. Accordingly considering constant physical properties in this range of Re, Ri is acceptable.

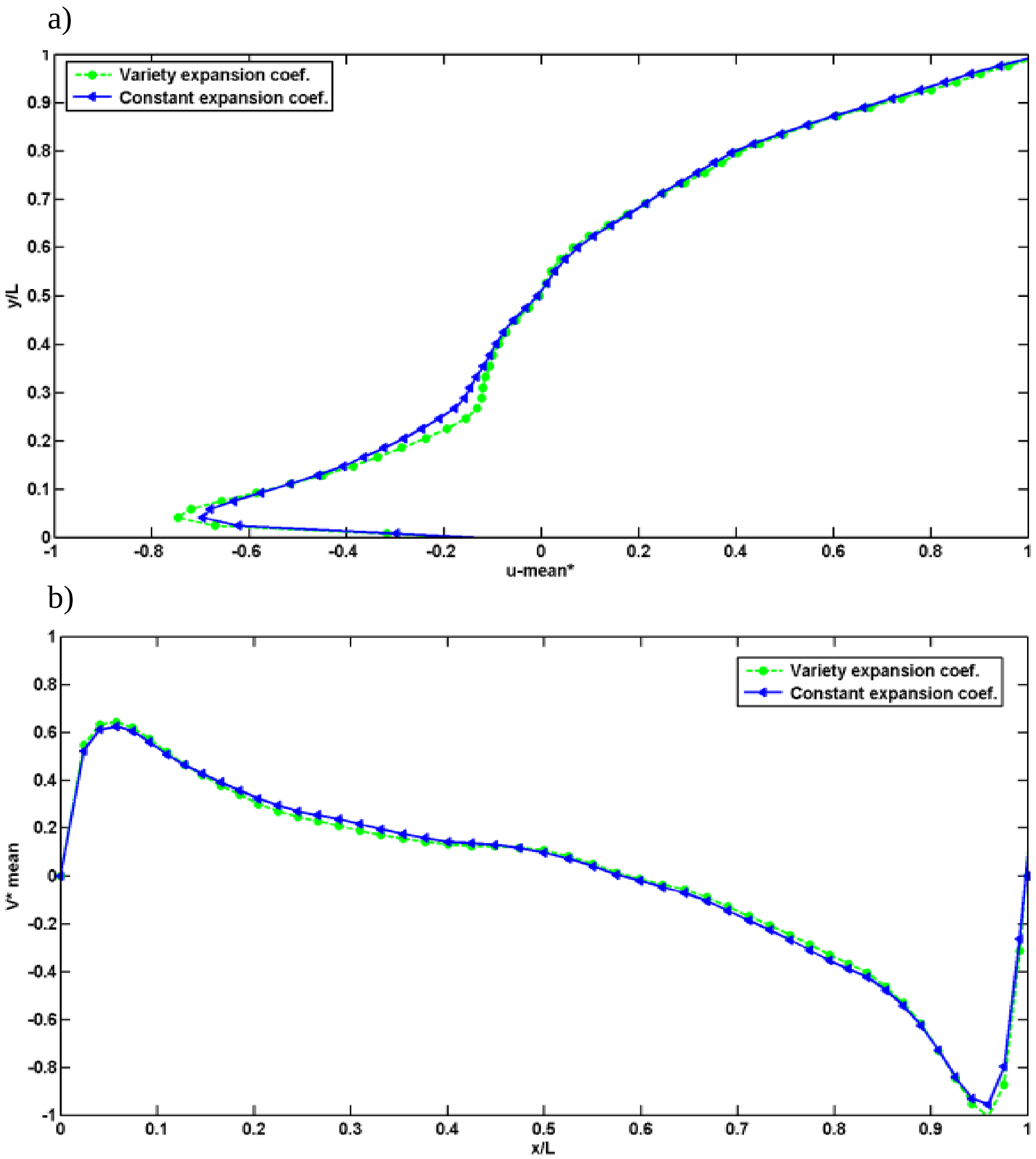

Figure 6.1: Comparison of the numerical results between the constant and temperature dependent expansion coefficient for Re=1500 at Ri=10, (a) u^* and (b) v^*.

6.2. EXPERIMENTAL RESULTS AND COMPARISON

In this section, the experimental results were analyzed and discussed. Achieving an experimental study was essential to validate the numerical results. The work plan proposed is to examine the crucial cases of the numerical results by experimental results and hereby we guarantee the rest of the results.

Isothermal and heated bottom configurations were applied experimentally. Actually, using such PIV experimental technique in this geometry presents a measurement challenge, because the maximum velocity inside the cavity is many times smaller than the flow velocity over the cavity [18]. This increases the required attention during the capture process. Other challenges appear during the measurements such as changes of the surrounding conditions.

The isothermal configuration has been implemented experimentally for two different Reynolds numbers (Re=1000 and 1500). The studied cases for each configuration are shown in **Table 6.1**. For the heated wall configuration, it has been observed experimentally that for small Ri≤1 for each Re the flow is similar to that examined in isothermal configuration which was found to be true for the two values of Re. This behavior may be explained due to the small temperature increment of the order of $\Delta T < 2°C$. For this reason, we focused on the cases of Ri=10 for each Re. The numerical results showed interesting unsteady flow characterized by a three-dimensional nature in these cases.

Table 6.1. List of the experimental cases and its states

Isothermal configuration			
Re		***Numerically***	***Experimentally***
1000	No heat transfer occurs	Steady state	Unsteady state
1500		Steady state	Unsteady state
Heated bottom configuration			
Re	***Ri***	***Numerically***	***Experimentally***
1000	10	Unsteady state	Unsteady state
1500	10	Unsteady state	Unsteady state

6.2.1. ISOTHERMAL CONFIGURATION RESULTS

The isothermal configuration has been implemented experimentally for Re=1000 and 1500. Different points have been considered to guarantee good accuracy during the measurements. The image frame was focused on the whole cavity plus the 5% of the flow in the channel. The flow cycle was running for more than 30 minutes before starting the image capture to avoid fluctuations generated by the pump and to eliminate air bubbles in the flow cycle. **Figure 6.2**, shows the velocity fields for Re=1000. The velocity field numerically calculated is shown in **Figure 6.2.a**, while **Figure 6.2.b** corresponds to the experimentally measured velocity field.

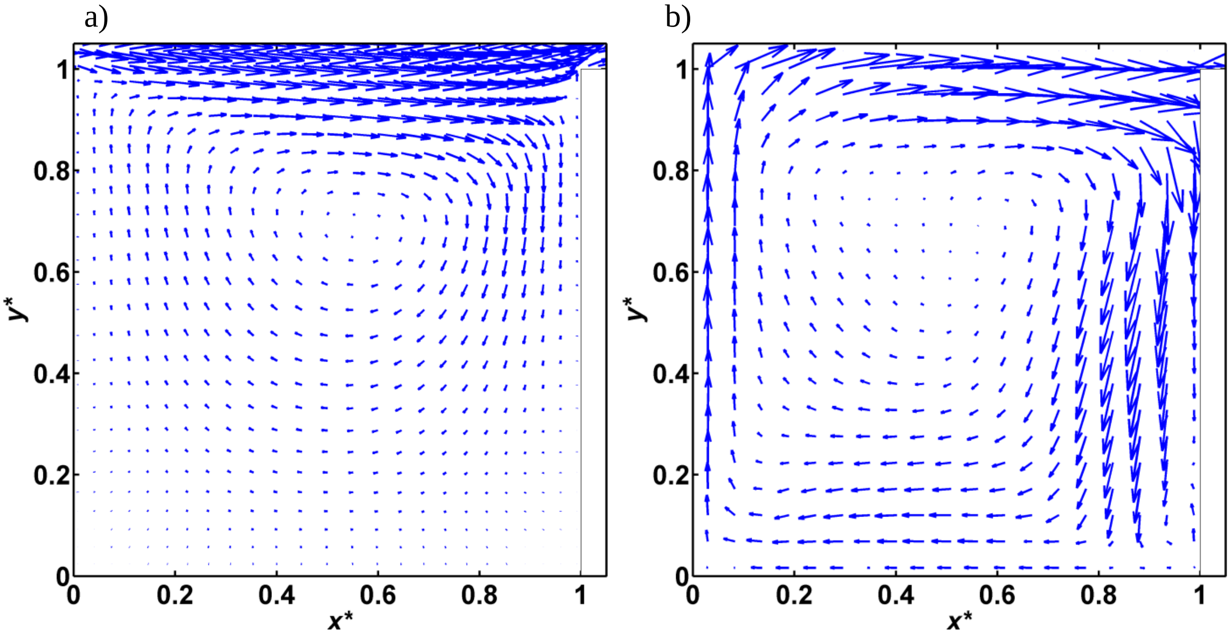

Figure 6.2: The velocity vector fields for the mean velocities for Re=1000, a) Numerical simulation and b) Experimental results.

It is obvious that there are significant differences between the two configurations mainly because under the experimental conditions the inflow profile was asymmetric and cannot be guaranteed to be completely constant as shown in **Figure 6.3**. This indicates that even small perturbations in the flow above the cavity can produce important differences with respect to the numerical results in the flow inside the cavity. It was found that the effect of these perturbations is strongly suppressed by increasing the Re and/or Ri. A possible explanation is the increment of the velocity components in the cavity that enhanced by the inertia and/or the buoyancy forces. This will be noticeable in the following results especially for Re=1500 with Ri=10. Also, it was found that the experimental inflow was asymmetric. However, the effect of the inflow condition on the cavity flow is discussed in details in **section 6.3**.

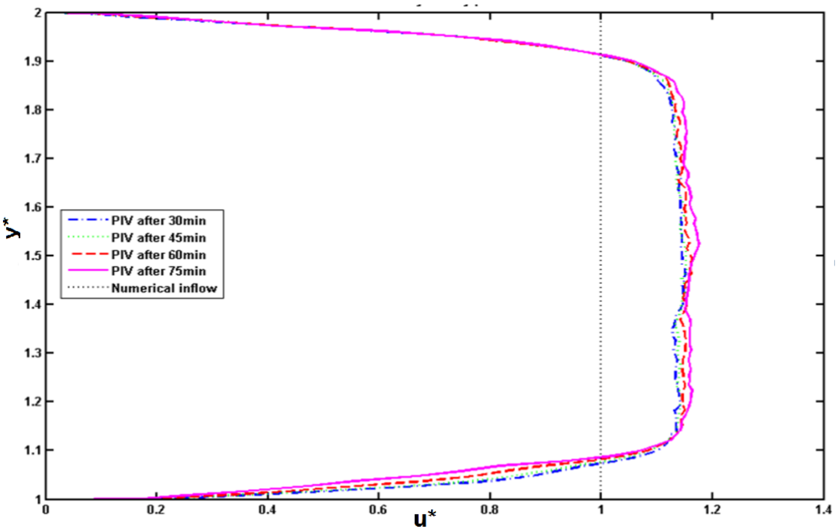

Figure 6.3: Inflow velocity profile at the vertical symmetry plane for the case Re=1500.

The location of the recirculation cell center in both numerical and experimental results is found to be the same, but both vortices do not have the same shape. Experimentally, the vortex is covering the whole cavity.

For Re=1500, **Figure 6.4** demonstrate that the differences in the flow structures found numerically (**Figure 6.4.a**) and experimentally (**Figure 6.4.b**) are reduced in comparison with results at Re=1000. This improvement is due to the relative reduction in the intensities of the perturbation as the flow-rate is increased. The main recirculation cell center is moved 20% laterally in the experimental results. Also, the opposite recirculation cell appears clearly in the experimental results.

The comparison between the numerical and experimental results of the vertical velocity component v^* is shown in **Figure 6.5**. It illustrates that, even though the fallen flow to the cavity in both is almost similar and at the same location, however the rising flow is different. Experimentally, the flow is rising faster close to the left wall than administered numerically. However, results were much improved in the heated configuration due to the increase of the velocities enhanced by the mixed convection.

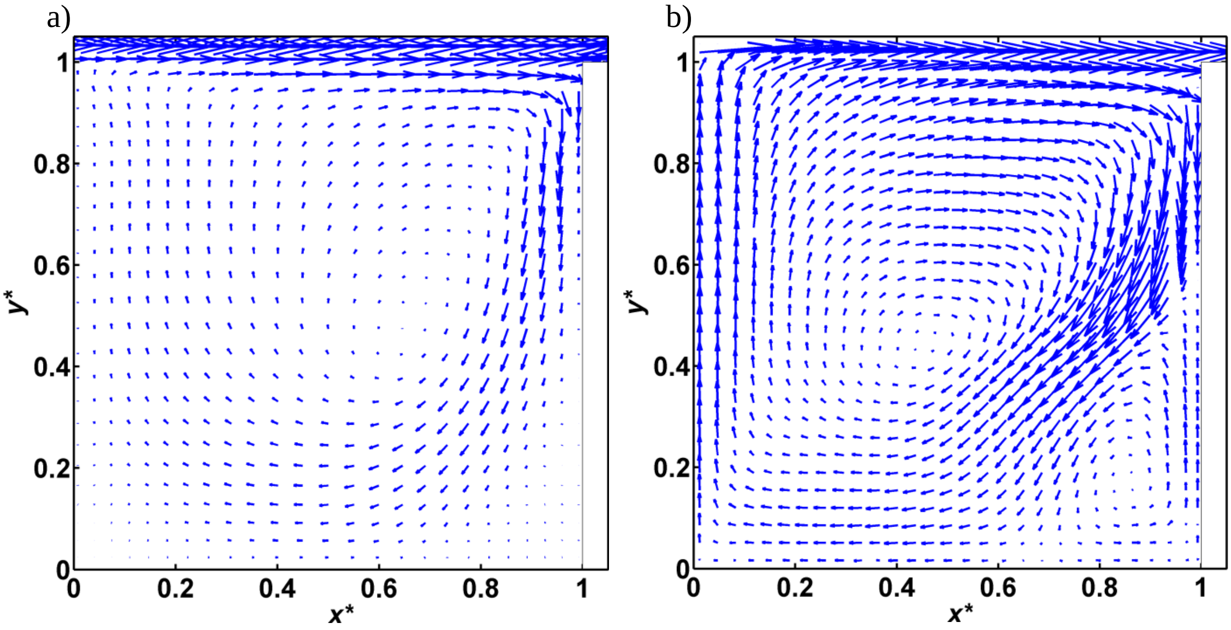

Figure 6.4: Velocity maps for the mean velocity for Re=1500, a) Numerical simulation, and b) Experimental results.

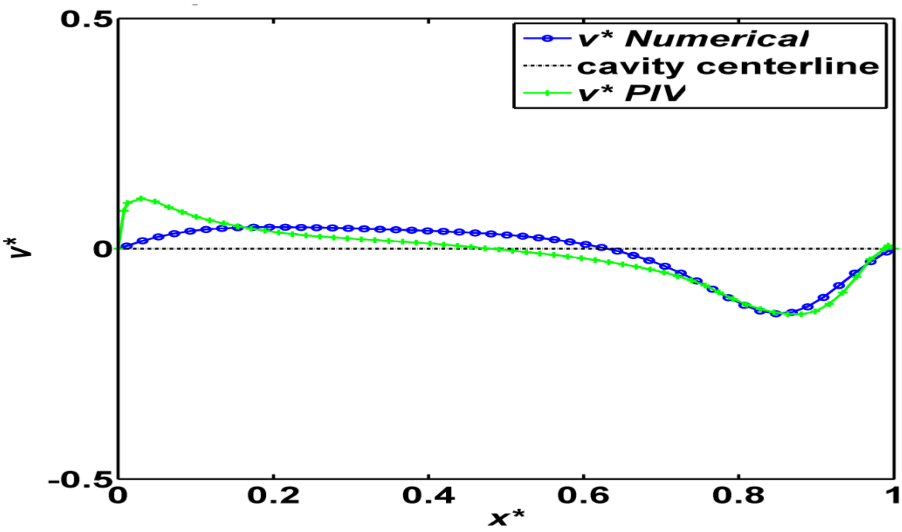

Figure 6.5: Comparison between numerical and experimental results of the v^* vertical velocity component at Re=1500.

6.2.2. CAVITY WITH HEATED BOTTOM WALL CONFIGURATION

In the cavity with the bottom wall heated, it was very difficult to apply an accurate experimental study for Richardson numbers in the range of Ri≤1, since the difference in temperature between the water inflow and the cavity bottom surface is less than 2 ^{o}C. Also, due to the experimental uncertainties and inflow profile matter. For these reasons, the experimental measurements were focused on Re=1000 and 1500 at Ri=10 where ΔT=5 ºC and 11ºC, respectively.

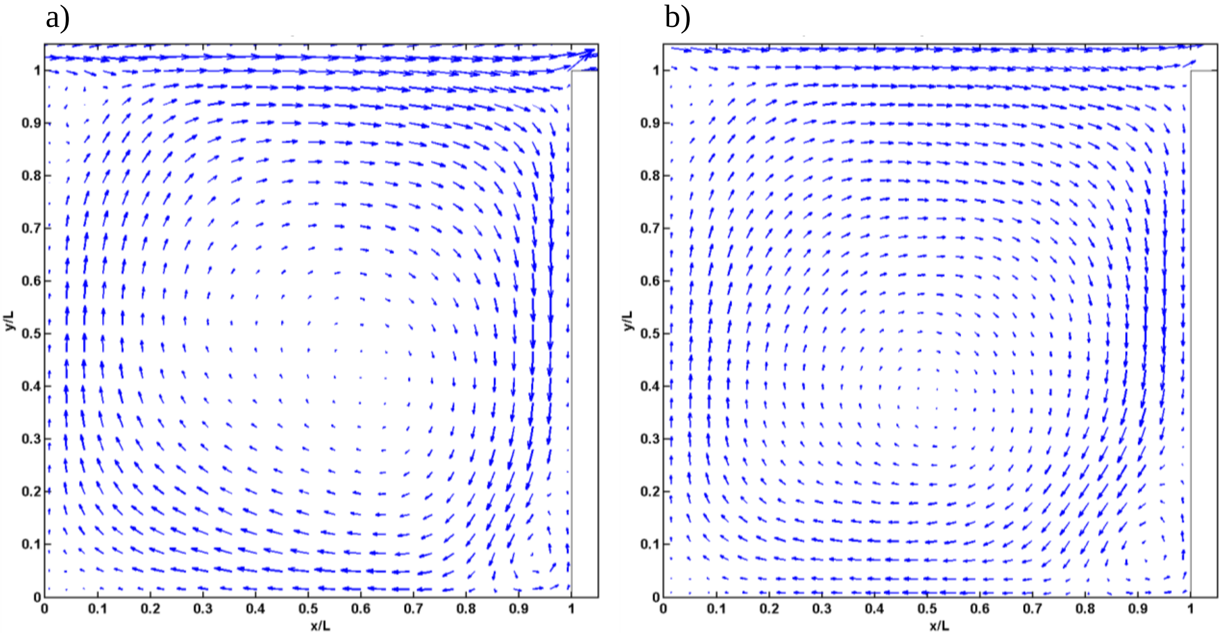

Figure 6.6: Velocity maps for the mean velocity in the streamwise symmetry plane for Re=1000 and Ri=10, a) Numerical simulation and b) PIV experimental results.

Figure 6.6.a and **Figure 6.6.b**, displays the numerical and experimental mean velocity maps of the flow in the streamwise symmetry plane for Re=1000 and Ri=10, respectively. Two opposite recirculation cells are shown. The principle recirculation cell covers around 90% of the cavity while the opposite recirculation cell appears on the downstream corner. Generally, there is a good agreement between both numerical and experimental structures. However, the relocate of the recirculation cell obtained from experimental results appears to

be at x^*=0.53 and y^*=0.4, while the simulations proposed a lateral shift, of ≈ 7% within the cavity to relocate at x^*=0.6 and y^*=0.4.

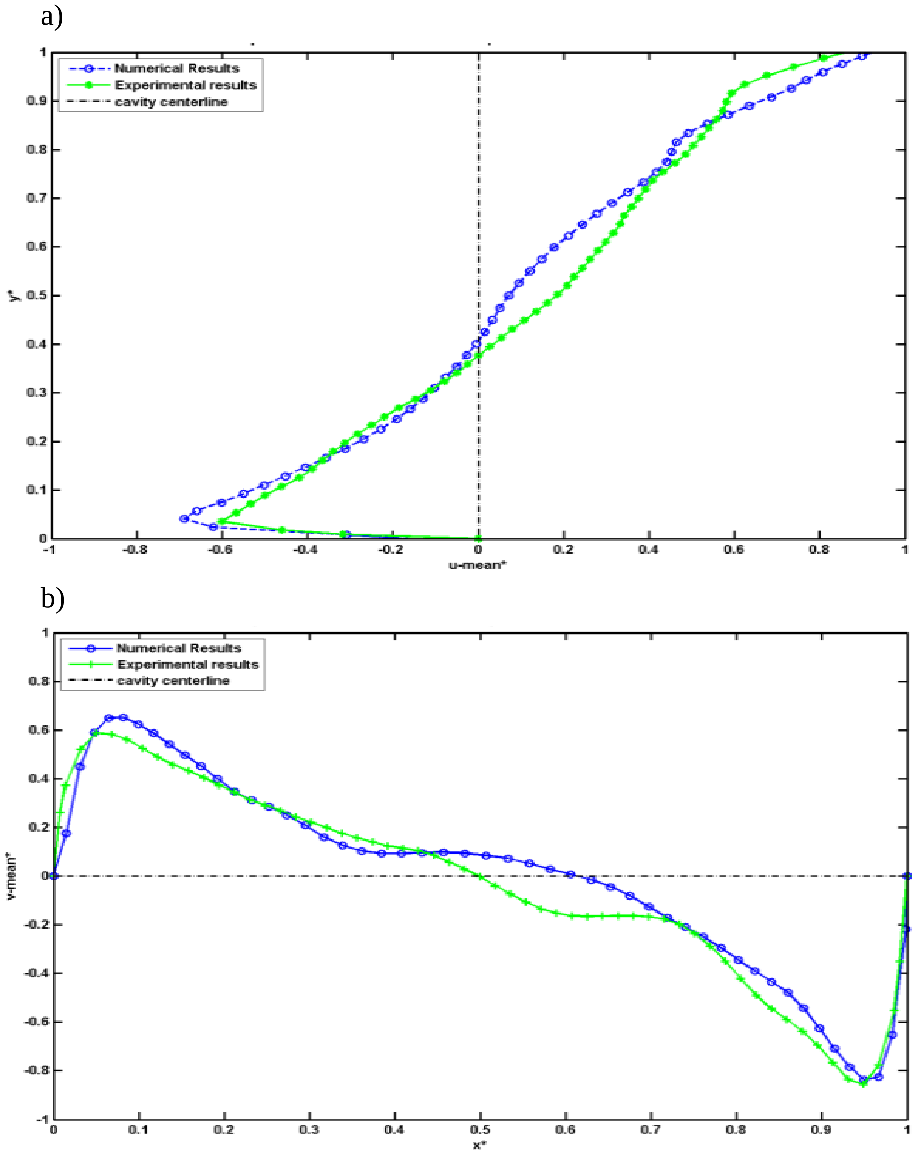

Figure 6.7: Comparison between u^* and v^* of the numerical and experimental results on the vertical cavity centerlines of the cavity symmetry plane for Re=1000 at Ri=10. (a) u^* *velocity* at x^*=1.5 and z^*=0.5, and (b) v^* *velocity* at y^*=0.5 and z^*=0.5.

The flow histories in both numerical and experimental results present an unsteady flow. This flow is turbulent inside the cavity and at the channel behind the cavity. A comparison between time average u^* velocity component acting on *x*-direction and time average v^*

velocity component acting on *y*-direction in the vertical and horizontal centerlines of the streamwise symmetry plane of the cavity are shown in **Figure 6.7**. The differences between the numerical and experimental results are due to the shift of the main recirculation cell between the numerical and the experimental results, which is effected by the experimental inflow condition.

The numerical and experimental mean velocity maps of Re=1500 with Ri=10 are shown in **Figure 6.8.a** and **Figure 6.8.b**, respectively. The only difference between the numerical and experimental results is a shift less than 5% of the center of the main recirculation. A comparison between the mean velocity components for both results in the centerlines of the symmetry plane is shown in **Figure 6.9**. The comparison shows an average velocity difference less than 6% that is produced due to the relocate of the recirculation center. Although, the comparison in this configuration shows a good agreement between the numerical and experimental results and consequently this authenticates the rest of the numerical results, a numerical simulation was conducted to identify the main reason of the differences, which might be the perturbation, the asymmetry or a combined effect.

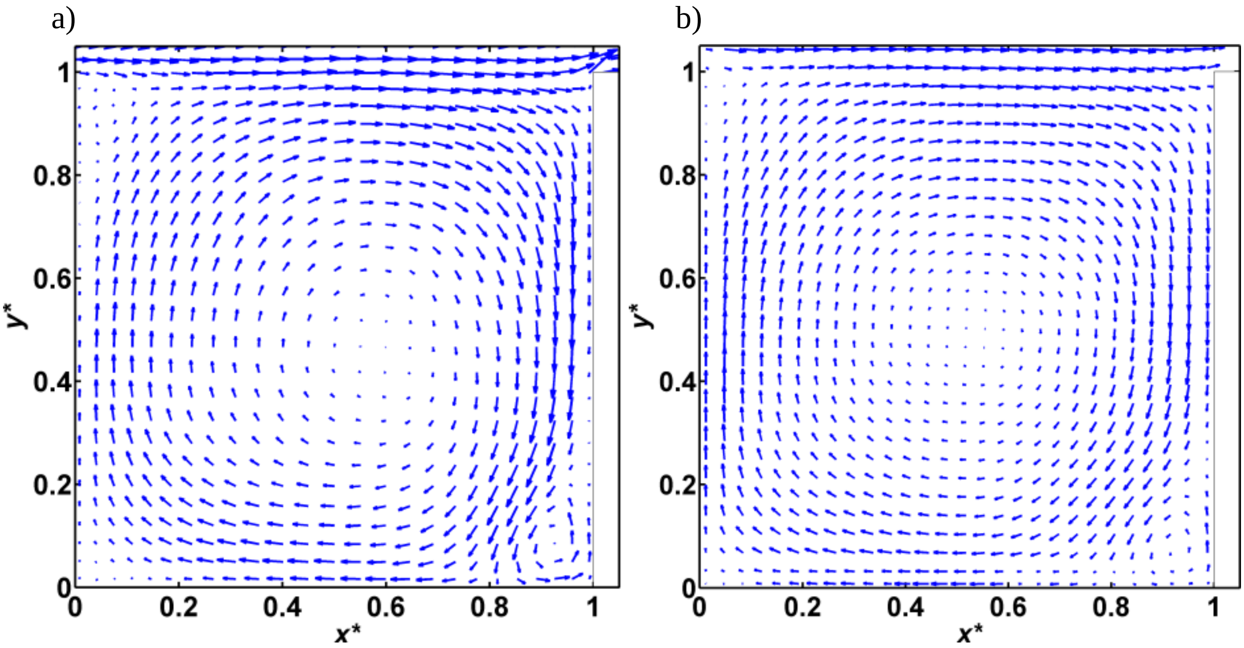

Figure 6.8: The mean velocity maps at the vertical symmetry plane of the cavity for Re=1500 at Ri=10. (a) Numerical results, and (b) Experimental results.

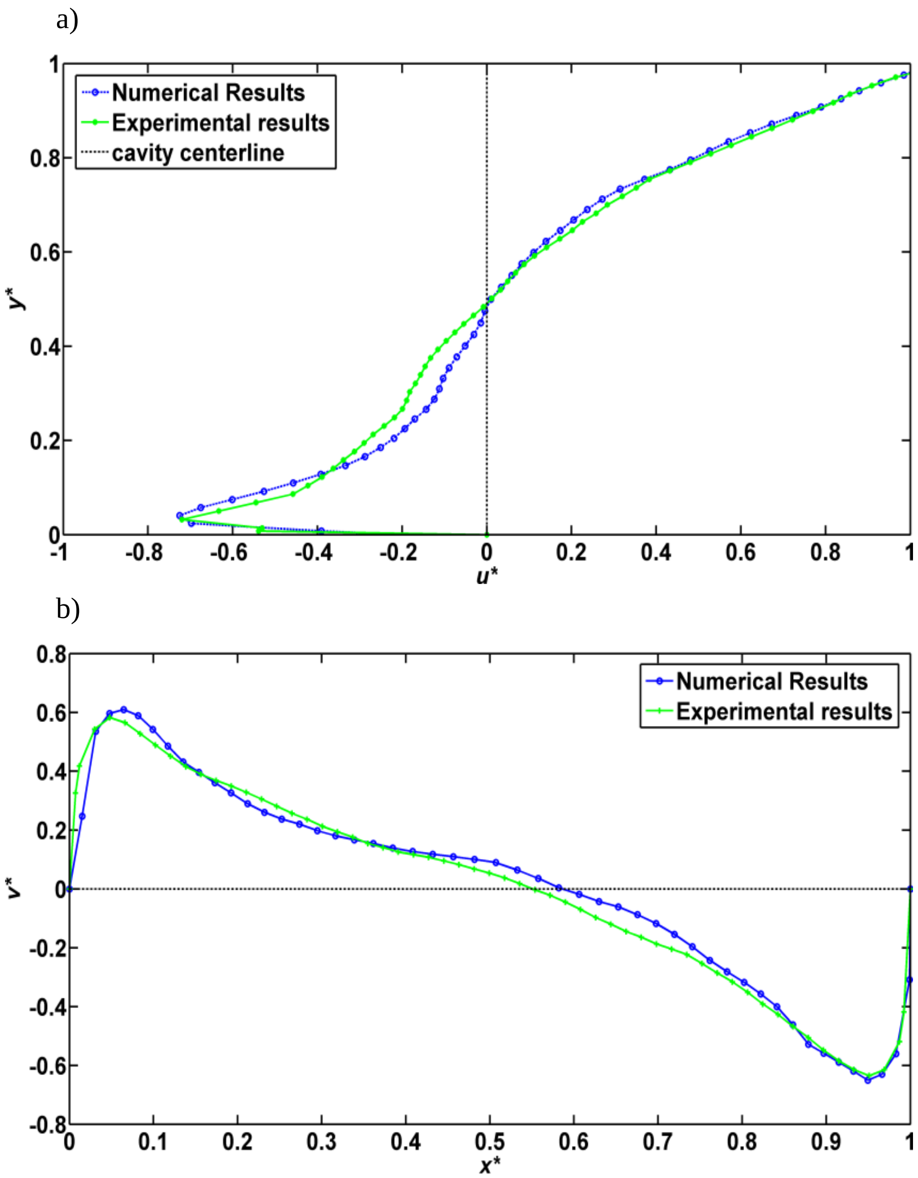

Figure 6.9: Comparison between numerical and experimental results for Re=1500 and Ri=10. (a) u^* *velocity* at x^*=1.5; z^*=0.5, and (b) v^* *velocity* at y^*=0.5; z^*=0.5.

6.3. EFFECTS OF INFLOW BOUNDARY CONDITION

The numerical simulation, in most cases, proposes the boundary conditions as in its ideal cases. In fact, to apply ideal boundary conditions in laboratories is extremely difficult due to the limitations on controlling the surrounding conditions and the fabrication uncertainties in the experimental setup.

In this work, the fluctuation and the asymmetry of the experimental inflow condition are the main problems. The pump used in this work has a high potential, since the minimum flow pumped was higher than that needed. Although, the use of high precession valve located behind the pump to control the flow, it was not able to control a fluctuation around ±3% of the flow-rate as illustrated in **Figure 6.3**.

However, extensive technical work has been done to obtain the inflow profile that is presented in **Figure 6.3**. Normalizing the laminar inflow was a challenge also due to some fabrication uncertainties. These uncertainties produce an inflow profile asymmetry as shown in **Figure 6.10.a**. This initial inflow profile was obtained before handling the inflow tank. In that case, the water in the inflow tank was passing through five pierced plastic screen with holes of 5mm diameter, separated from each other by 15 mm. Then to the contraction placed on the front of the inflow opening in order to direct the flow to the main channel.

Figure 6.10.b shows the inflow profile under the same conditions after handling the inflow tank. In this case, the water in the inflow tank passes through seven mesh plastic screen 1mm×1mm, separated from each other by 15 mm. These screens were divided into two groups separated by a honeycomb 10mm×10mm with 30mm thickness followed by the contraction (**Figure 4.3**). Also, the flow-rate controller valve was replaced by a high precision controller valve. However, although some improvement has been achieved in the inflow profile, we could not handle perfectly neither the asymmetry problem (**Figure 6.10.b**) nor the perturbation since the resultant profile was a bit twisted and the inflow condition was not completely constant, **Figure 6.3**. Consequently, the steadiness will never be achieved experimentally due to the effect of the inflow perturbation. For this reason, a clear difference

was shown in the isothermal configuration because we are comparing between a numerical steady cases with an experimental unsteady cases.

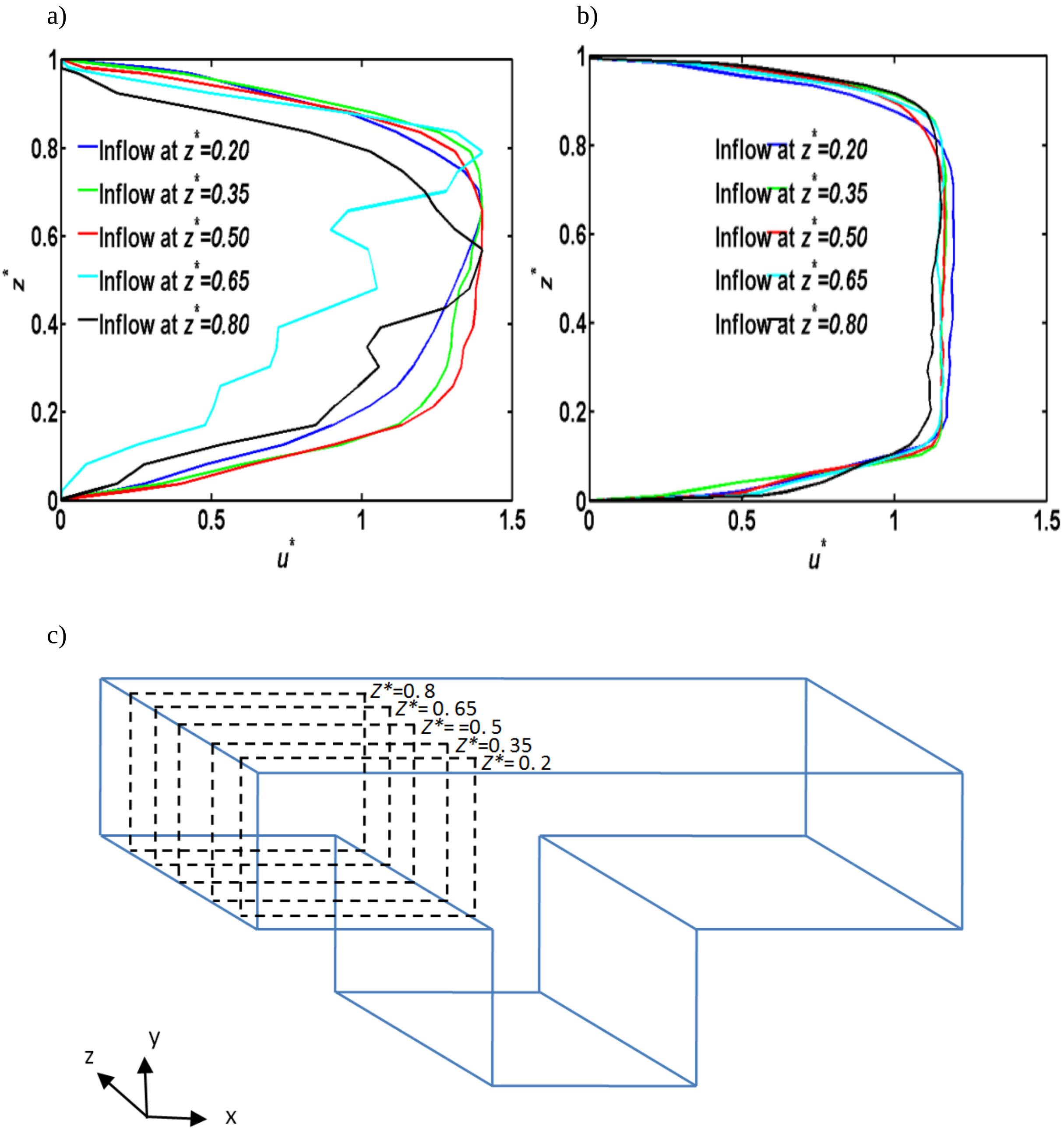

Figure 6.10: The inflow profile at x^*=0.1, in different vertical positions along the channel depth z^*. (a) Before handling, (b) After handling, and (c) Measurement planes.

Numerical simulation have been conducted for the real inflow profile found experimentally shown in **Figure 6.11.a**, to assure if that difference between numerical and experimental results is actually due to the asymmetry inflow boundary conditions or a result of the inflow perturbations. Also, another twisted inflow profile with a higher asymmetry (**Figure 6.11.b**) was considered to check the effect of the twisted incoming boundary layer. The results were compared with the ideal uniform inflow boundary condition simolations.

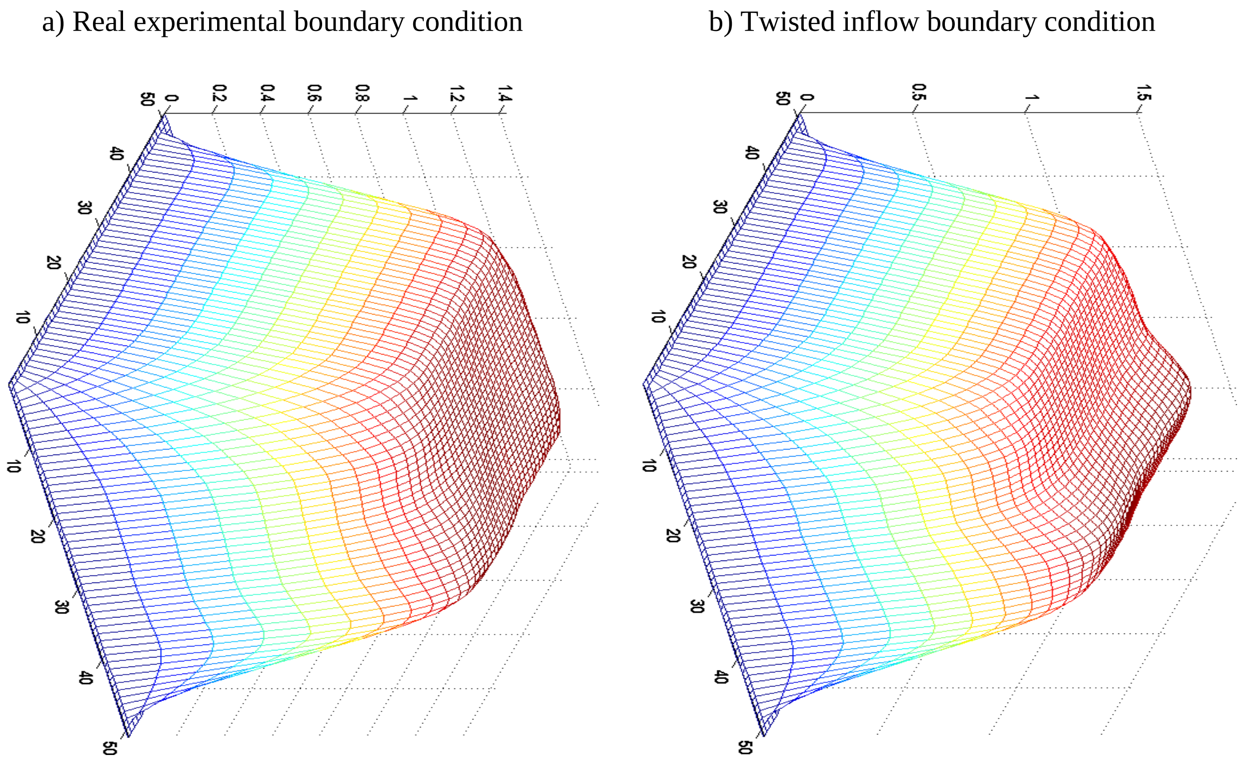
a) Real experimental boundary condition

b) Twisted inflow boundary condition

Figure 6.11: The inflow boundary conditions applied numerically to check the asymmetry effects. (a) Real inflow boundary condition occurs experimentally, and (b) Extra twisted inflow boundary condition.

6.3.1. EFFECTS OF ASYMMETRIC INFLOW BOUNDARY CONDITION ON THE FLOW STEADINESS

The numerical results declared that there is no effect of the asymmetric inflow boundary condition for both of the actual experimental profile and the twisted profile on the steadiness of the flow within the cavity. The temporal evolution for each velocity component in the three dimensions at Re=1000, is shown in **Figure 6.12**. The steady state has been reached for all tested inflow boundary condition. These velocities were checked at the same nodes mentioned previously. This proves that the flow-rate fluctuations (perturbation) are responsible of losing the steadiness in the experiments for isothermal cases.

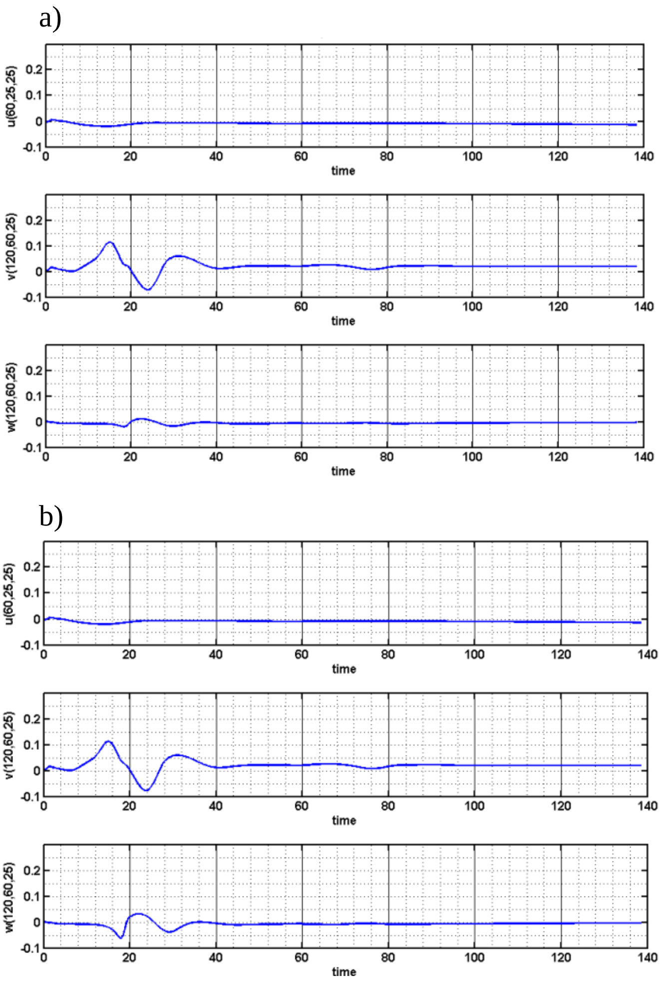

Figure 6.12: Stability of the velocity components with time at Re=1000. (a) Real experimental inflow profile, and (b) Twisted inflow profile.

6.3.2. EFFECTS OF ASYMMETRIC INFLOW BOUNDARY CONDITION ON THE VORTEX LOCATION

As it was shown previously that the main difference concluded from the comparison between experimental and numerical results is the relocation of the center of the recirculation cell (main vortex). The relocation of the vortex is presumably caused by the asymmetric inflow boundary condition or from the perturbation of the flow-rate.

Figure 6.13 shows a comparison between streamlines in the cavity symmetry plane of ideal, actual asymmetry, twisted inflow and experimental results. The comparison shows that, the effect of the asymmetric inflow boundary condition on the vortex position in the cavity symmetry plane is less than 3%. This indicates that the asymmetric inflow condition participates together with the perturbation in the relocation of the recirculation cell center.

From the previous results, the asymmetric inflow boundary conditions are responsible for a difference around 3% between experimental and numerical results. However, the numerical simulations expected a steady flow for isothermal case (Re=1000 and 1500) for all the assumed inflow boundary conditions. Experimentally, we could not generate a fully laminar steady inflow profile because of the perturbations and asymmetry. The perturbations prohibited the flow steadiness and the steady state never reached. Hereby, comparing between a steady flow and unsteady flow is not logic, while comparing with the mean unsteady flow is not accurate. However, the effect of the perturbation was significantly reduced by increasing the velocities in the heated bottom wall configuration.

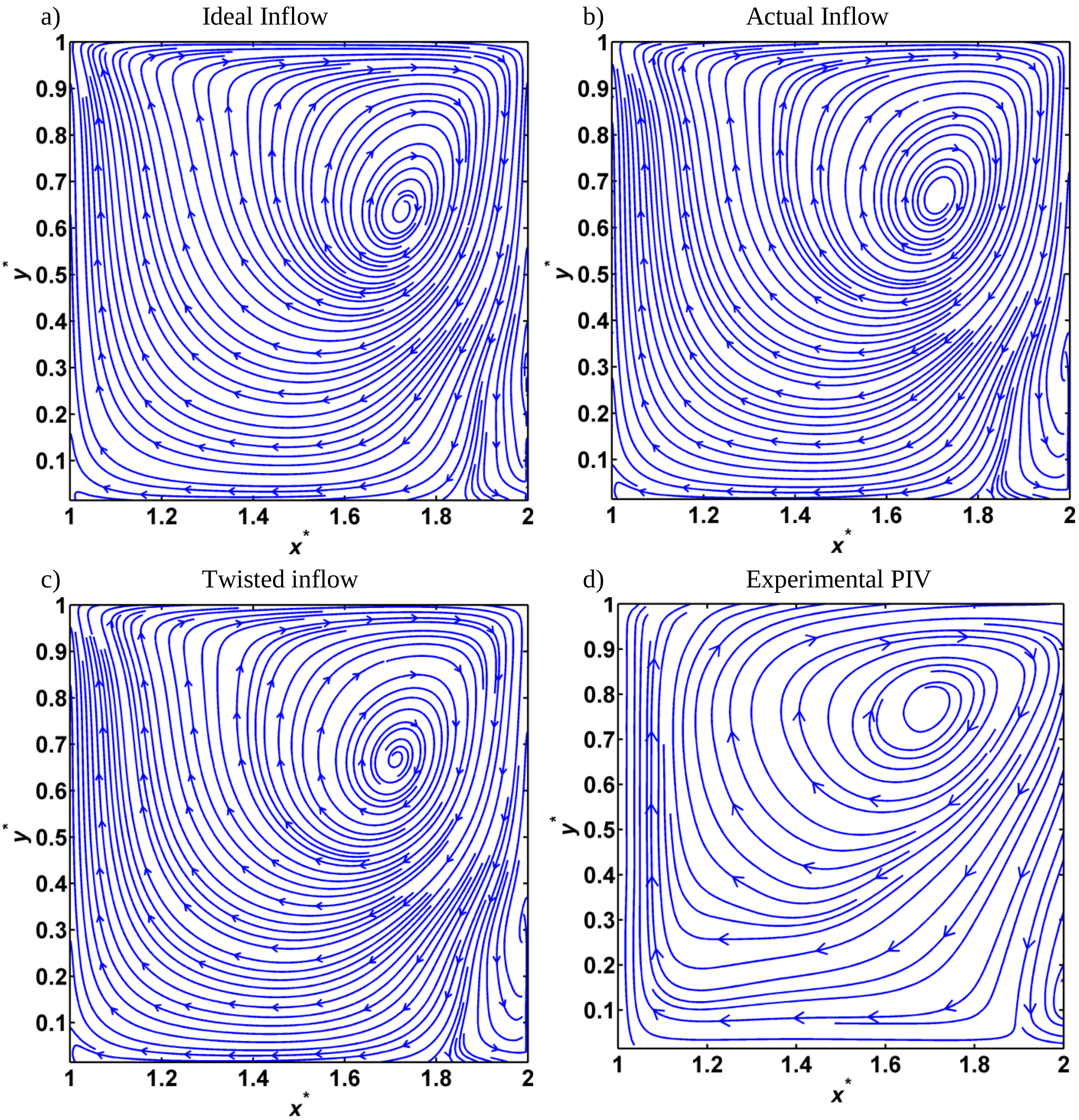

Figure 6.13: Streamlines in the cavity streamwise symmetry plane at Re=1000.

6.4. NUMERICAL RESULTS

The isothermal configuration is considering that no presence of heat transfer and the walls have no-slip conditions. This configuration was studied also for the water flow in the same range of Re in order to track the effect of heating the bottom wall on the flow stability. The list of the studied cases and its states are listed in **Table 6.2**.

Table 6.2. List of the numerical studied cases and its states

Ri *Re*	Isothermal	0.1	1	10
100	Steady state	Steady state	Steady state	Periodic state
500	Steady state	Steady state	Turbulent	Turbulent
1000	Steady state	Steady state	Turbulent	Turbulent
1500	Steady state	Steady state	Turbulent	Turbulent

The flow in the isothermal configuration is steady in all cases through the range of Re≤1500, as demonstrated in **Table 6.2**. In the heated bottom wall configuration, the flow remained steady for all cases of Re at Ri=0.1. The flow becomes unsteady at Re≥100 for Ri≥10, and for Re≥500 with Ri≥1.

The time evolution of the unsteady flow structures has been investigated in order to determine the changes that are introduced on the flow by heating the bottom wall by Ri≥1. The progression patterns of the unsteady flow in the cavity are divided into two main patterns. One of these patterns is periodic which appears at Re=100 with Ri=10. The other pattern is turbulent flow occurs at Re≥500 with heating the bottom wall in the range of Ri≥1.

First, we shall discuss the performance of the steady patterns for both configurations. The discussion will facilitate finding the differences that occur by heating the bottom wall with a small Ri. Then the study of the periodic and turbulent patterns will follow.

6.4.1. STEADY FLOW PATTERN

The steady patterns of Re=100 occur in the isothermal case and also while heating the cavity bottom wall with a small Ri≤1. **Figure 6.14** shows the vertical velocity v^* for Re=100 for the isothermal configuration and heated bottom wall configuration with Ri=1.

Comparison between **Figure 6.14.a** and **Figure 6.14.e** shows that the flow exchange between the cavity and the channel is similar in both cases. The exchange layers move over the vortex top in the streamwise direction. The mixed fluid separates along the shearing edge (the upper right edge) of the cavity. Some layers leave the cavity and others assist the vortex within the cavity.

Figure 6.14.b and **Figure 6.14.f**, show the v^* vertical velocity contours at y^*=0.5 for both configurations. The flow descends near the right half and ascends near the left half of the cavity. The main difference between both cases is found in the intensity of the velocity, which is larger in the mixed convection case because of the assisting effect of the buoyancy term in the vertical momentum equation. The cross-section level exactly cuts the center of the vortex at the heated configuration, but it does not cut the vortex center of the isothermal configuration. However, the heated configuration velocities are higher than the isothermal, **Figure 6.14.c** and **Figure 6.14.g**.

For the heated configuration, the temperature effect on the vertical velocity at the channel is weak (**Figure 6.14.g**). The temperature layers are clustered close to the heated wall and the left wall of the cavity (**Figure 6.14.h**). The vortex in this case is faster and larger. It is located further below within the cavity in comparison with the isothermal case as shown in **Figure 6.14.d**. It is promoted by the temperature layers especially close to the left wall.

Isothermal configuration

a) v^* at y^*=1 *b)* v^* at y^*=0.5

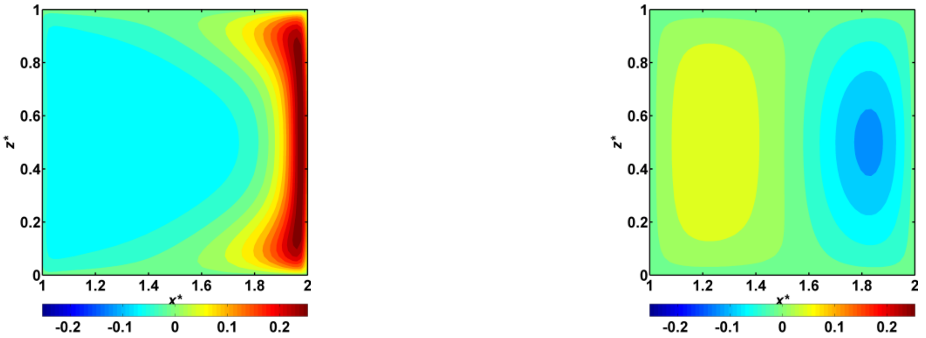

c) v^* at z^*=0.5 d) The streamlines at z^*=0.5

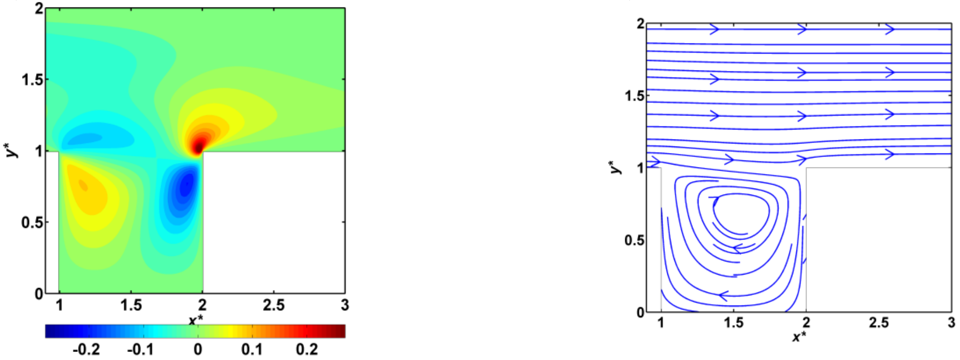

Heated bottom wall configuration

e) v^* at y^*=1 f) v^* at y^*=0.5

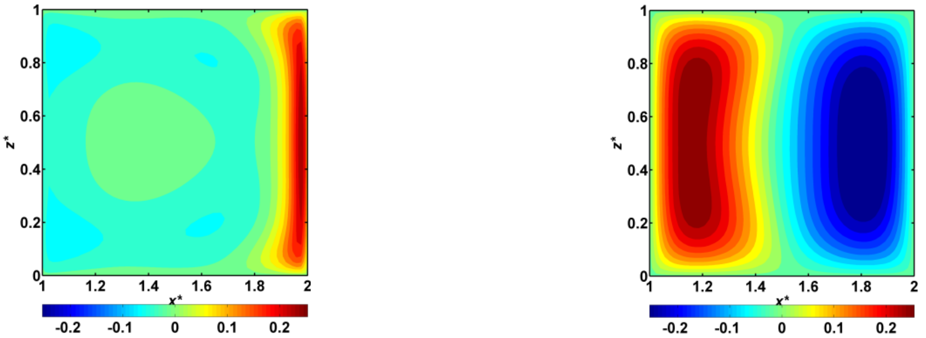

g) v^* at z^*=0.5 h) Temperture/streamlines at z^*=0.5

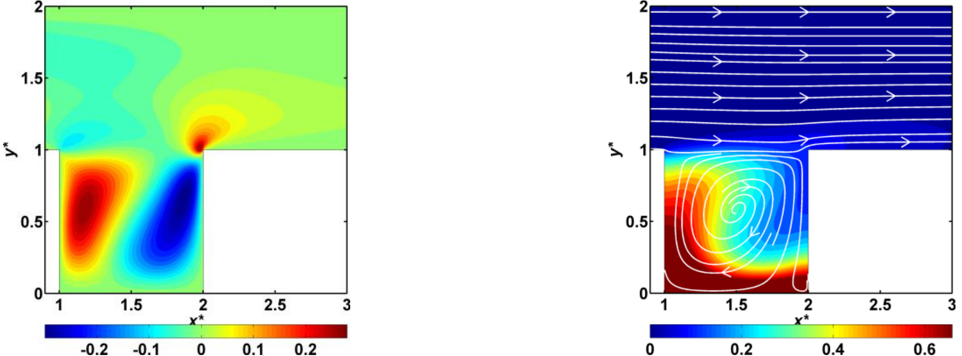

Figure 6.14: Contours of v^* and temperature distribution in several planes at Re=100. (a-d) Isothermal configuration, and (e-h) Heated bottom wall configuration at Ri=1.

The definition of the vortex core location within the cavity is one of the tools of interest to provide a better illustration of the three dimension structure within the cavity and the channel. The λ_2 approach, proposed by Hussain [54] has been used to calculate the vortex core in the incompressible flows. This model is based on specifying a connected region with two negative eigenvalues of the symmetric tensor $S^2 + \Omega^2$. The eigenvalues S and Ω are respectively the symmetric and anti-symmetric parts of the velocity gradient tensor $\overrightarrow{\nabla u}$; i.e. $S_{ij} = \frac{1}{2}(u_{i,j} + u_{j,i})$ and $\Omega_{ij} = \frac{1}{2}(u_{i,j} - u_{j,i})$. Only real eigenvalues are found since $S^2 + \Omega^2$ is symmetric. If λ_1, λ_2 and λ_3 are eigenvalues and $\lambda_1 \geq \lambda_2 \geq \lambda_3$, hence this definition is equivalent to the requirement that $\lambda_2 < 0$ within the vortex core. Three components of the velocity field must be available to plot the structures of the vortex core by means of λ_2 iso-surfaces.

Figure 6.15 illustrate the iso-surfaces of the λ_2 in the entire domain for Re=100. The isothermal configuration is shown in **Figure 6.15.a**, while the bottom heated wall configuration is shown in **Figure 6.15.b**. The flow in each case is steady which means that the flow structure is unchangeable with time and consequently the vortex core is fixed. Only one core of the vortical structure is presented inside the cavity for each case. Each vortex core reflects the size of the recirculation cell within the cavity. The difference is clear since the vortex of the heated configuration is extended to occupy more space than the isothermal configuration vortex. However, increasing the Richardson number to (Ri=10) for the same (Re=100) the flow loses the stability and become periodic.

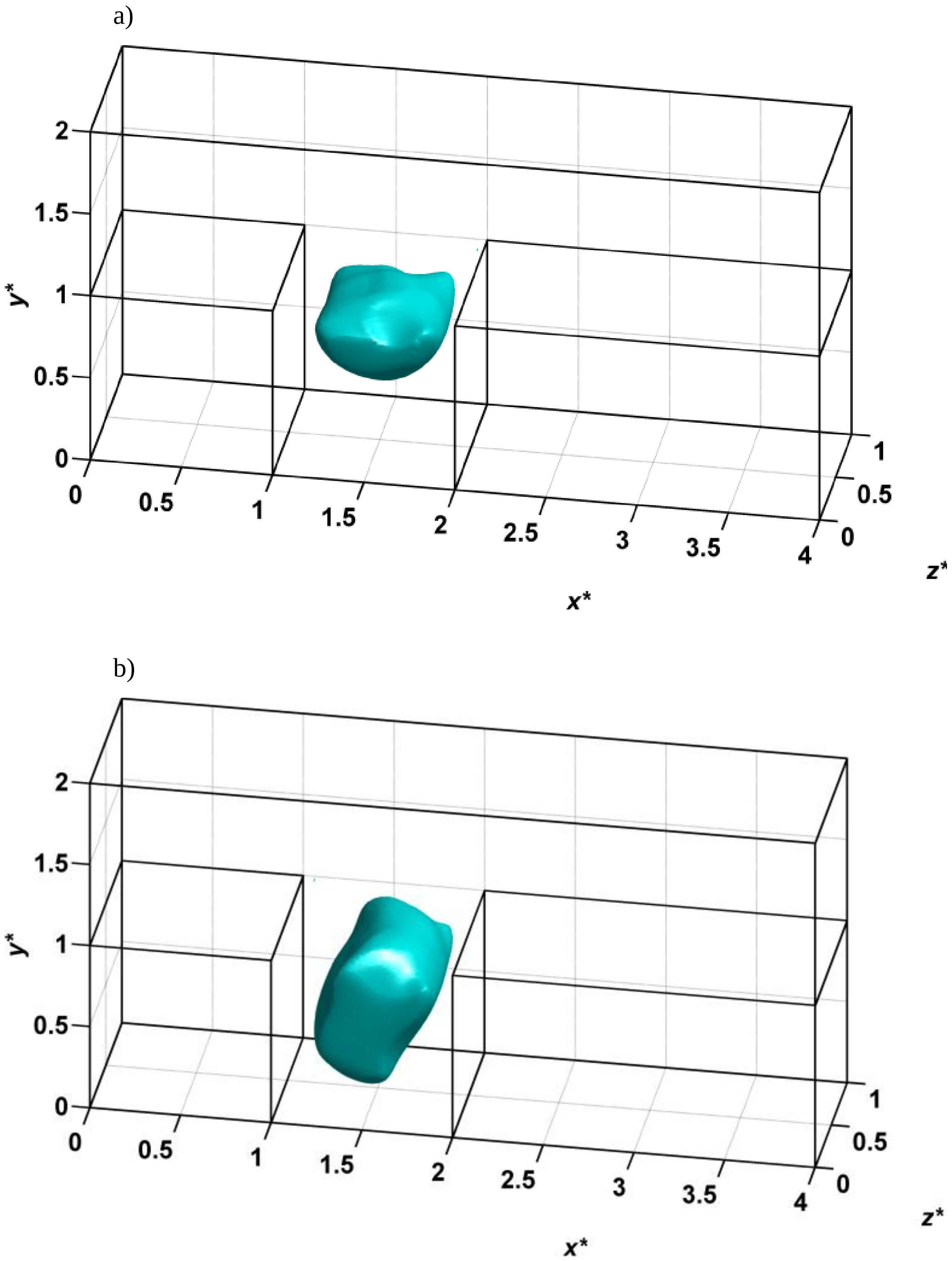

Figure 6.15: The vortex core at Re=100. (a) Isothermal configuration, and (b) Heated wall configuration at Ri=1.

6.4.2. PERIODIC FLOW PATTERN

The periodic flow pattern is observed at Re=100 and Ri=10. The evolution of the *x*-component of the velocity (u^*) at $x^*=1.2$, $y^*=0.5$, $z^*=0.5$, which is located in the symmetry plane close to the leading vertical wall of the cavity, is shown in **Figure 6.16.a**. The power spectrum (**Figure 6.16.b**) shows a non-dimensional main frequency of $f^*=2/7$ and a harmonic at $f^*=1/7$. These frequencies correspond to non-dimensional periods of 3.5 and 7, respectively.

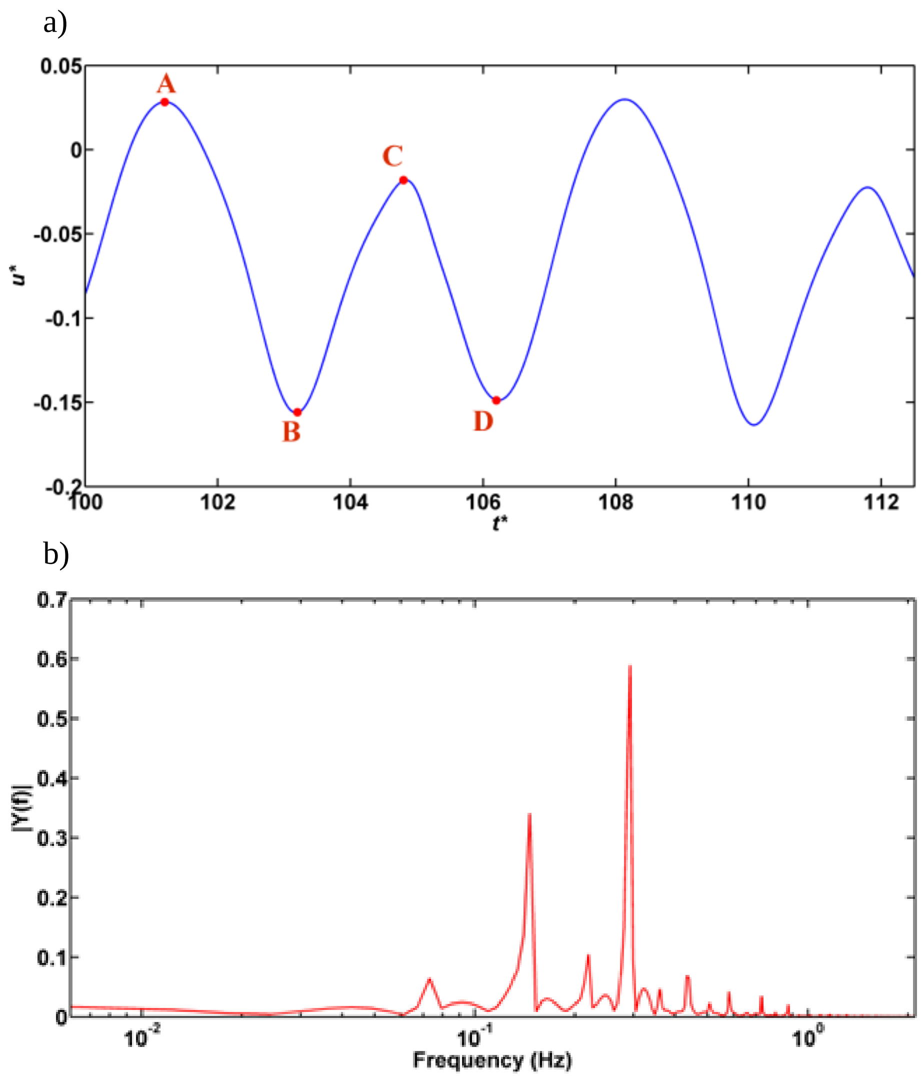

Figure 6.16: Periodic pattern of Re=100 at Ri=10. (a) u^* velocity component, and (b) Power spectrum.

During the period, the hot fluid of the lower part of the cavity has a lower density. It moves up under the buoyancy forces that became more effective by increasing the Richardson number. The hot fluid interacts with the cold fluid closer to the cavity border. Some hot fluid leaves the cavity while the rest mixes again with the main vortex.

The history of the main vortex in the cavity shows that the intense coherent vortex rotates in the streamwise direction, but it moves laterally along z-direction between the front and back walls. This happens even though the maximum downfall velocity value of $v^*$is centered close to (z^*=0.5) during the whole period. The vortex axis moves several times during a single period. It moves with an angle less than ±26.6º from the default axis (z-direction). The rotational and the axial movement of the vortex affect the mixing process between the hot fluid and the clod fluid in the cavity border (y^*=1).

The contours of the instantaneous vertical velocity component at y^*=1 are shown in **Figure 6.17**. This depicts flow evolution in a period at the cavity border. The points on the curve of **Figure 6.16.a** correspond to the frames **A**, **B**, **C** and **D** shown at **Figure 6.17**. The lateral movement along the depth and the interaction that happens in the cavity border between the hot and the clod fluids make the flow penetrates and leaves the cavity from mutual locations during fixed time intervals. It can be seen that the sequence of the flow alternates flow ejections near each one of the two lateral walls of the cavity (see **Figure 6.17 B** and **D**), with an intermediate state that corresponds to a simultaneous symmetric ejections near both lateral walls (see **Figure 6.17 A** and **C**).

The initial structure (**Figure 6.17 A**) has been chosen at a selective initial time t^*_0 in which the vortex rotation matches the x-y streamwise symmetry plane. The fallen flow penetrates the cavity border close to the center of the cavity depth (z^*=0.5) along the length (x-direction) of the cavity. In the same moment, the hot fluid leaves the cavity border from both sides adjacent to the front and back walls.

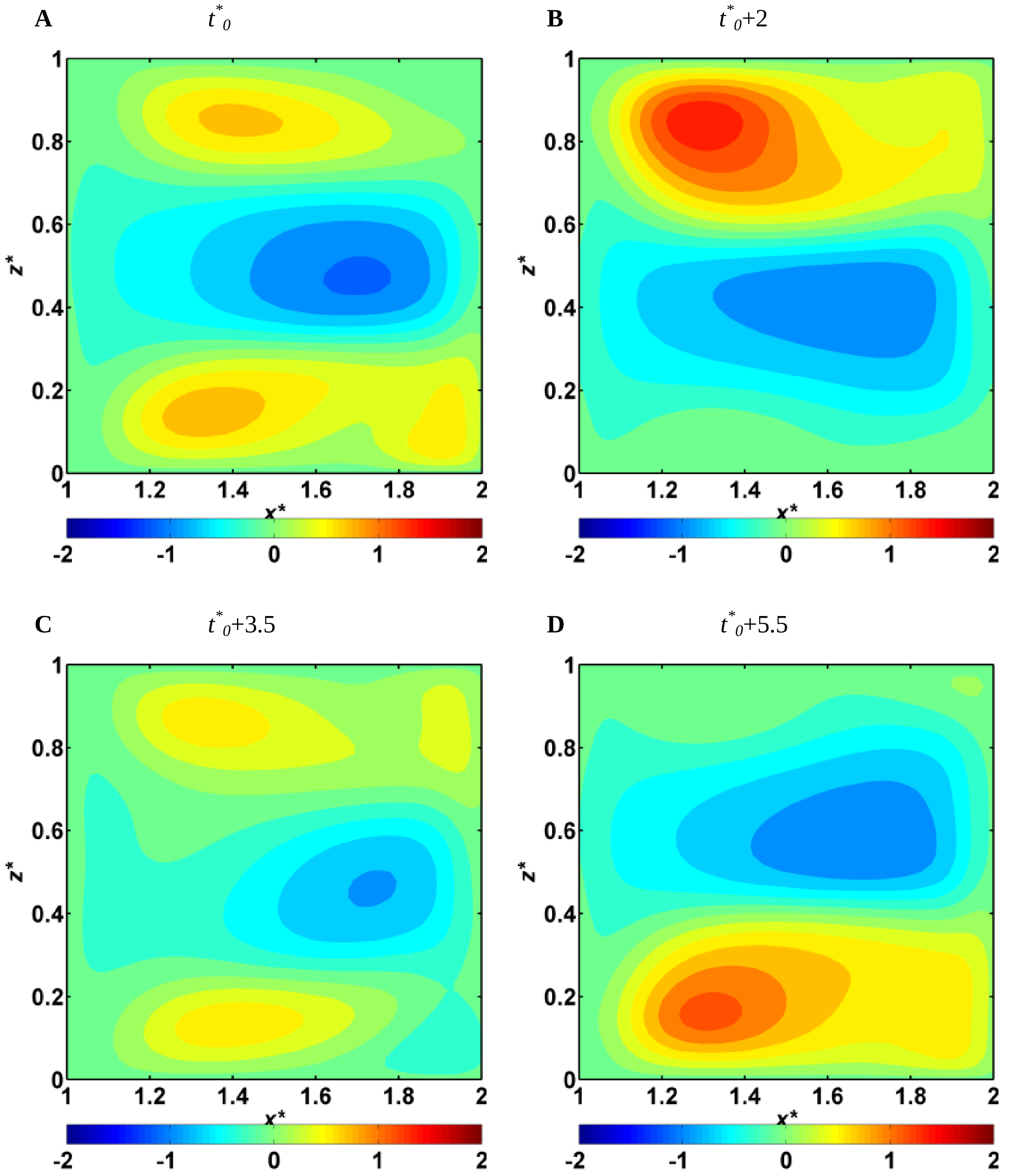

Figure 6.17: Vertical v^* velocity profile at cavity border cross-section ($y^*=1$). (a) v^* velocity at t^*_0, (b) v^* velocity at t^*_0+2, (c) v^* velocity at $t^*_0+3.5$, and (d) v^* velocity at $t^*_0+5.5$.

Shortly after, the vortex moves toward back wall. In the moment that the vortex meets the back wall (**Figure 6.17 B**) the fluid leaves the cavity border close to the back wall ($0.6 \leq z^* \leq 1$); while the cold fluid penetrates the cavity from the front side ($0 \leq z^* \leq 0.6$). After that, the vortex shocks the back wall and reverses its direction toward the front wall.

On the way to the front wall, the vortex transits again the *x*-*y* vertical symmetry plane of the cavity (**Figure 6.17 C**). At this moment, the external fluid returns to penetrate the cavity border from the center of the depth along the whole length, while the fluid leaves the cavity border from both sides as it was in **Figure 6.17 A**.

When the vortex meets the front wall (**Figure 6.17 D**), the fluid leaves the cavity close to the front wall ($0 \leq z^* \leq 0.4$), while the cold fluid penetrates the cavity from the backside ($0.4 \leq z^* \leq 1$). Finally, the vortex reverses its direction again to back to the initial position to start a new period and so on.

Similarly, it is notable that frames **C** and **D** of the cavity border tend to be offsets of **A** and **B**. This indicates that the conditions are reversed along to the depth in *z*-direction during the same period. If we look back to the power spectrum shown in **Figure 6.16.b,** and by comparing its time periods with that of these structures, we find that the period of the highest peak in the spectrum ($t^*=3.5$, $f^*=2/7$), corresponds to the time consumed for repeating condition **A** (which is **C**, too). Also, it was found that the period associated with the second highest peak of the second powerful frequency ($t^*=7$, $f^*=1/7$), agrees with the time needed to complete a full period, which is the time consumed for repeating **B** or **D** condition; see **Figure 6.16**.

Figure 6.18.a and **b** correspond to the instantaneous contours shown in **Figure 6.17 B** and **D**, respectively. Both figures depict a pair of counterotating streamwise vortices connected with the main vortex inside the cavity. It can be observed that a secondary vortex near the bottom of the cavity parallel to the edge located at $x^*=2$ and $y^*=0$ is existing. The pair of large scale counterotating streamwise vortices extracts fluid near the lateral walls of the cavity and introduces fluid from the channel to the cavity between them. The instantaneous flow

structures are not symmetric with respect to z^*=0.5. It can be seen that the different intensities of the vortices is associated with the location of the flow ejection (**Figure 6.17 B** and **D**). The larger vortex induces an important flow ejection near the corresponding lateral wall.

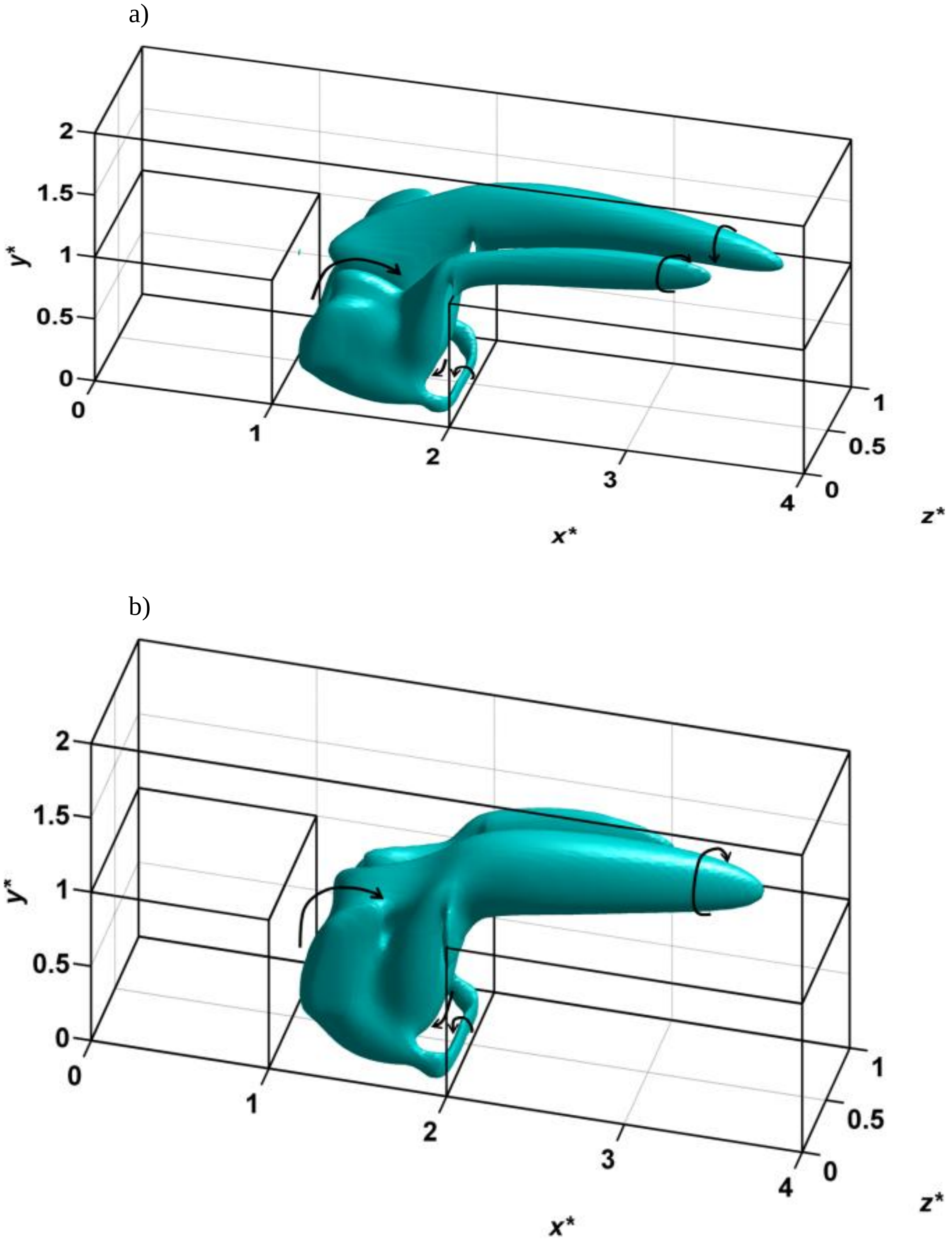

Figure 6.18: Instantaneous flow structures at Re=100 at Ri=10 in terms of an iso-surface of λ_2. (a) Corresponds to the time of **Figure 6.17 B**, and (b) to the time of **Figure 6.17 D**.

6.4.3. TURBULENT FLOW PATTERN

The turbulent pattern, which is for Re≥500 at Ri≥10, is more complicated in comparison with the steady and periodic patterns. Increasing the Reynolds number and the Richardson number increase the inertia of the flow and the buoyancy force and hereby the mixed convection.

The time averaged flow topology at Re=1500 and Ri=10 is shown in **Figure 6.19** in terms of an iso-surface of λ_2. On average, the flow is organized similarly to the periodic flow. A main vortex inside the cavity, a small secondary vortex at the bottom of the cavity and two counter-rotating vortices distributed along the streamwise direction in the channel.

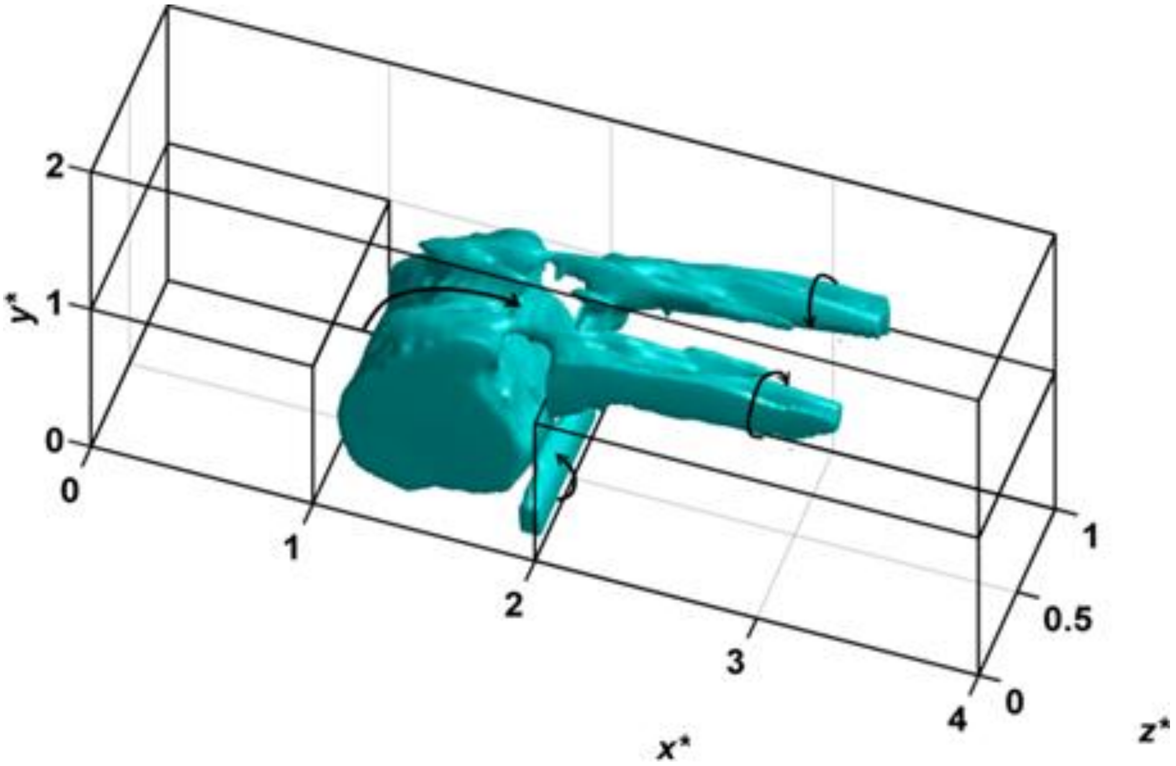

Figure 6.19: The time-averaged vortex core at Re=1500 and Ri=10.

As an example of the flow unsteadiness, **Figure 6.20.a** shows the time evolution of the spanwise velocity component (w^*) at the point x^*=2.2, y^*=1.2 and z^*=0.5, which is located in the channel near the top trailing edge of the cavity. The corresponding power spectrum

(**Figure 6.20.b**) shows a more uniform distribution of energy among a wide range of frequencies than that obtained for the periodic flow at Re=100 and Ri=10 (**Figure 6.16.b**). It can be seen as a marked peak at f^*=1/15 indicating the existence of periodicity in the flow pattern.

a)

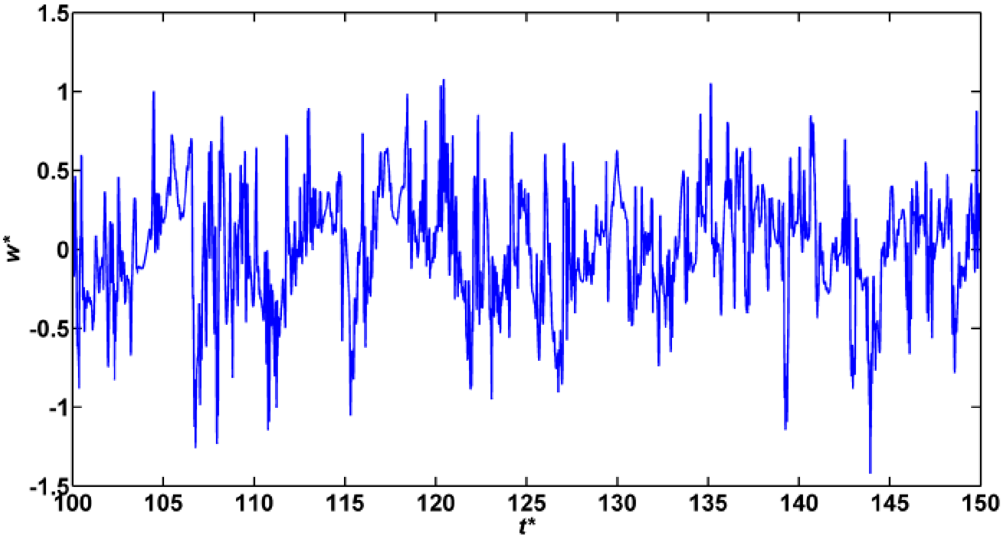

b)

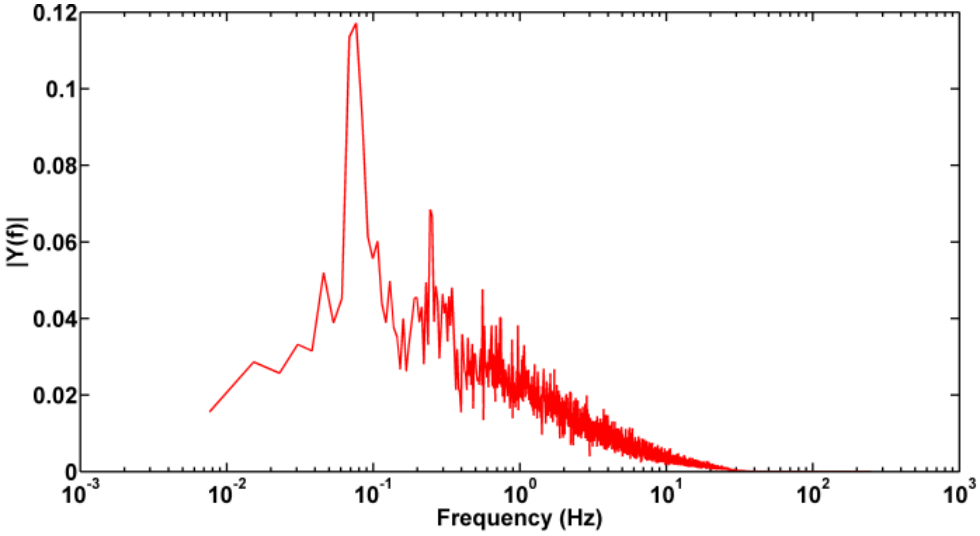

Figure 6.20: (a) The instantaneous w^* velocity in a specific node with time, and (b) Power spectrum of the w^*.

To educe the flow structures responsible for this periodicity a conditional sampling technique has been used. The time evolution of 300 individual samples of the vertical velocity distribution at $y^*=1$ during a period of 150 non-dimensional time units is used to detect the strong flow ejections near lateral walls of the cavity. These events are classified into four different patterns depending on the location of the flow ejection according to the values of the correlation between the instantaneous distributions and each of the four templates. The templates are built with patterns of positive lobes distributed in different locations: one symmetric template with two lobes near the lateral walls (**A**), one template with a single lobe near the wall located at $z^*=1$ (**B**), one symmetric template with a single lobe centered at $z^*=0.5$ (**C**), and one template with a single lobe near the wall located at $z^*=0$ (**D**). A similar technique has been applied successfully in previous studies to obtain flow patterns in turbulent forced [55] and natural [56] convection flows.

Results are shown in **Figure 6.21**. The four ensemble averages of the vertical velocity distribution at $y^*=1$ obtained correspond to the 63% of the flow history analyzed, indicating that these are not the only structures present in the flow. It should be noted that even the important periodicity of the flow (**Figure 6.20.b**) strong fluctuations are present (**Figure 6.20.a**). The individuals used to obtain the ensemble averages in each case are indicated in **Figure 6.21** at the top of each graph.

The most probable structure is depicted in **Figure 6.21 A**, while the other three structures have similar probability. The inspection of the time evolution of the velocity distribution shows the existence of transitions among the four patterns. The numbers of transitions observed are included near the arrows in **Figure 6.21**. It has been found that the main frequency of the flow corresponds to transitions between structures A and B or A and D similarly to the periodic flow case.

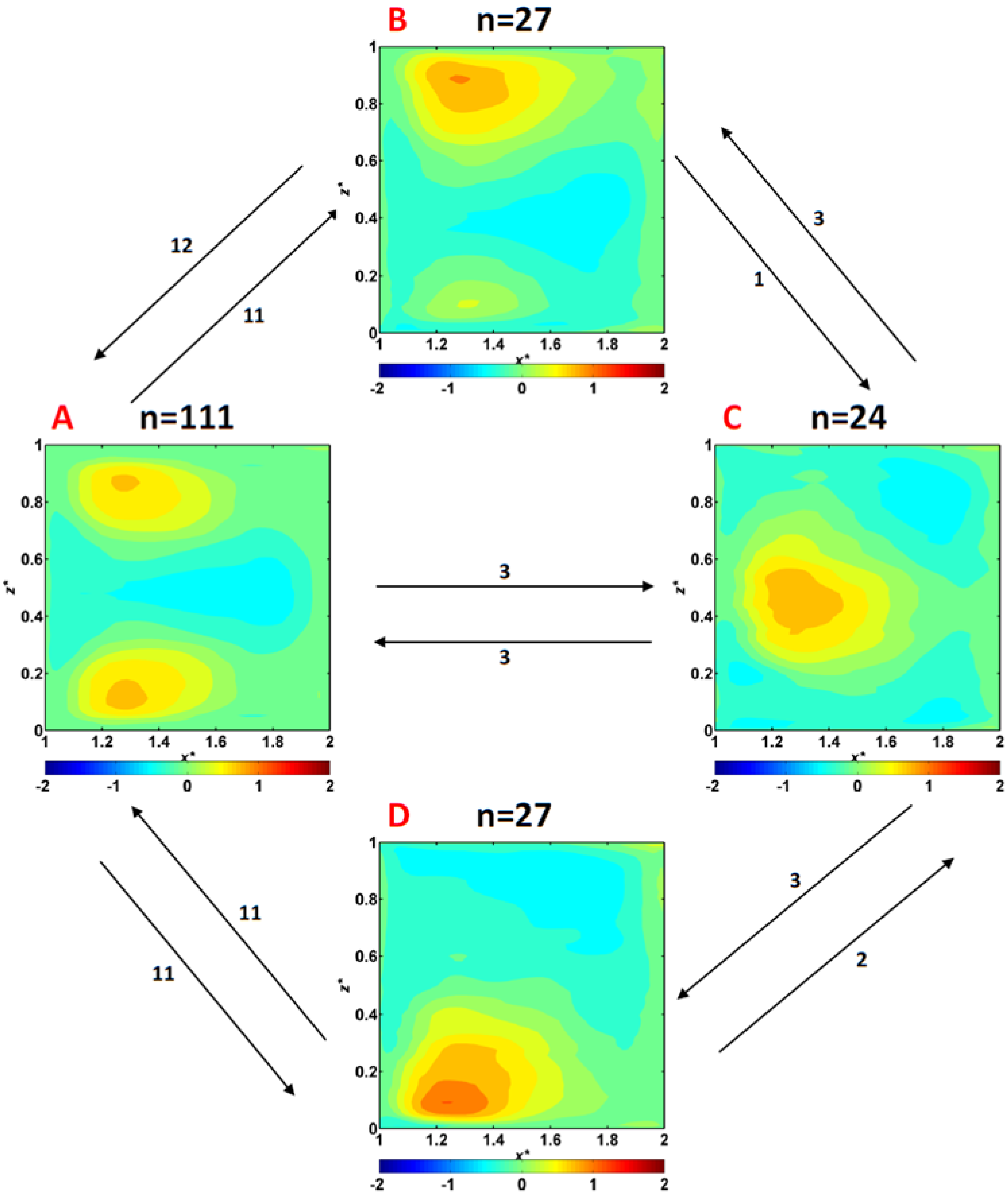

Figure 6.21: Conditional sampling for vertical velocity v^* at the cavity border. The hot flow leaves the cavity border from: (A) Both front and back sides, (B) Back side, (C) Middle of z^*, and (D) Front side.

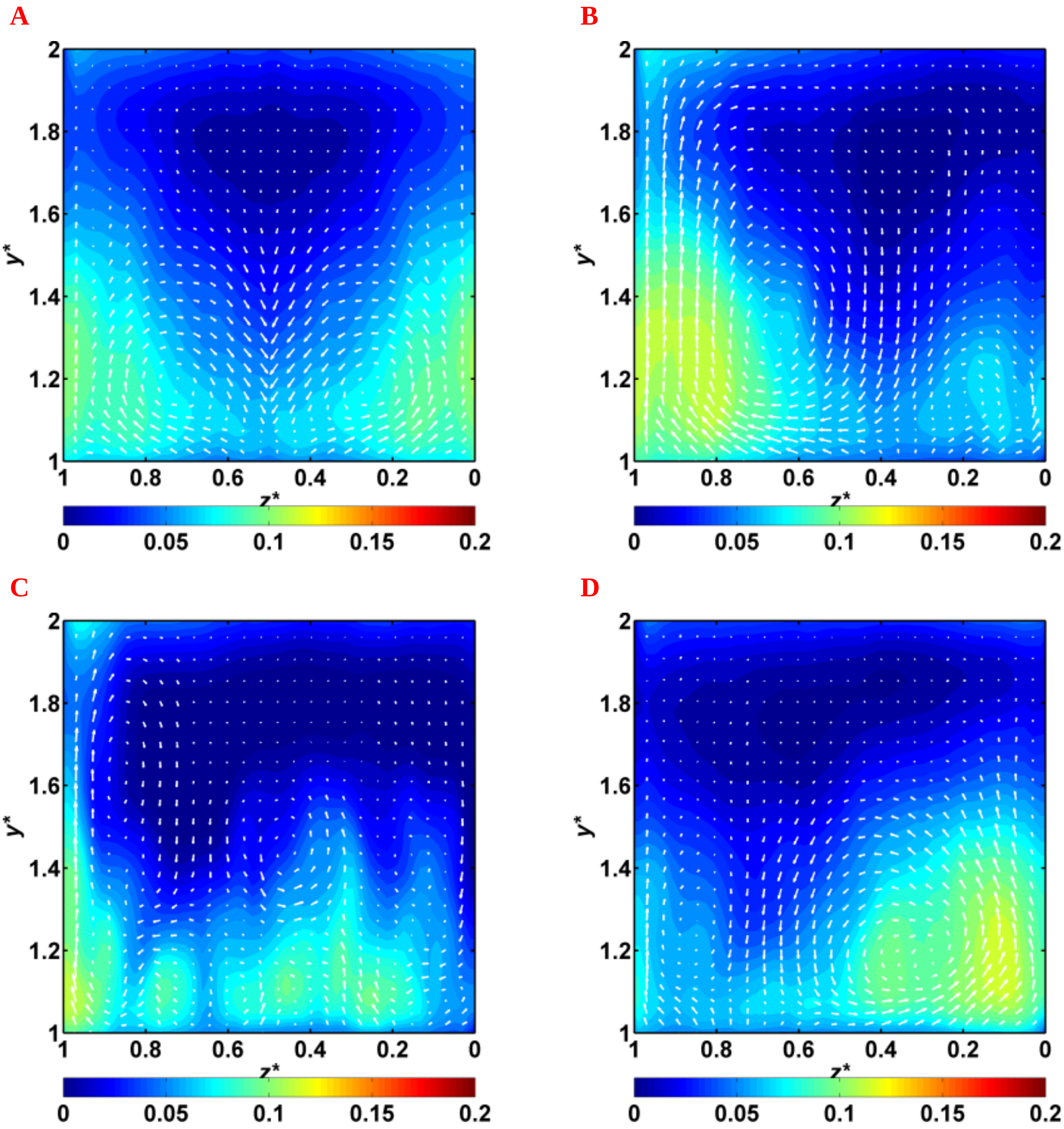

Figure 6.22: Cross-stream vector velocity field with temperature contours at x^*=2 for the conditionally sampled flow patterns.

To illustrate the effect of the detected flow structures on the channel, **Figure 6.22** shows the conditionally averaged temperature and cross-stream velocity field in a vertical plane near the trailing edge of the cavity (x^*=2). It can be seen that the symmetrical distributed flow ejections (**Figure 6.21 A**) produce two hot ascending currents near the lateral walls of the channel. Patterns B and D show an individual stronger ejection of hot fluid near the corresponding lateral wall. Pattern C has more uniformly distributed hot fluid along the spanwise direction.

6.4.4. HEAT TRANSFER RATE

The average Nusselt number at the bottom wall of the cavity is shown in **Figure 6.23**. It can be seen that the heat transfer rate increases with the Richardson and Reynolds numbers. The present curves (Pr=7) are similar to that found previously for air flow (Pr=0.7). The large increase of the Nusselt number at Re=1500 between Ri=1 (Gr=2.25×10^6) and Ri=10 (Gr=2.25×10^7) is produced by the dominant effect of the natural convection inside the cavity that improves the flow exchange between the cavity and the channel.

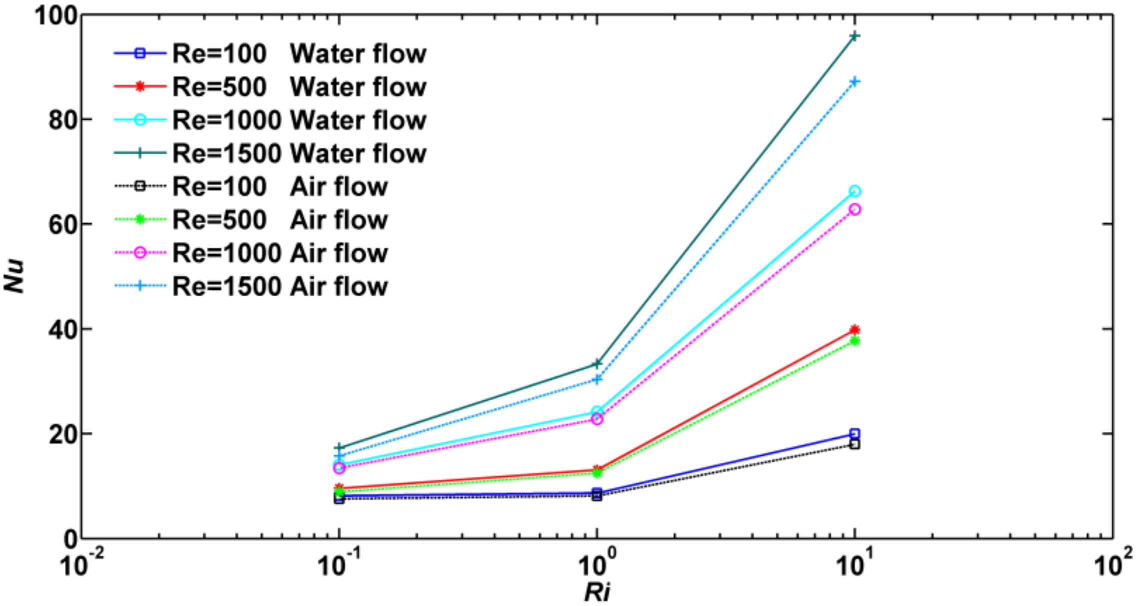

Figure 6.23: Average Nusselt number on the heated wall.

Leong et al. [9] reported a correlation (Eq. 6.1), based on numerical simulations, to predict Nusselt number in two-dimensional cavities for several aspect ratios (AR=1, 2 and 4).

$$\frac{Nu_w}{Re_w^{1/2}} = \left[0.0195 + 0.219\left(\frac{Gr_w}{Re_w^2}\right)\right]^{1/4} \qquad (6.1)$$

where Re_w and Gr_w are Reynolds and Grashof numbers based on the cavity width.

Figure 6.24 compares the present data with those obtained by Leong et al. [9]. The gray zone indicates the scatter of the data used to compute the correlation (two-dimensional results for several aspect ratios), the squares correspond to the three-dimensional air flow simulations, and the triangles to the present three-dimensional water flow results. The agreement between Equation 6.1 and the present results indicates the validity of the correlation to predict heat transfer rates in three-dimensional cavities.

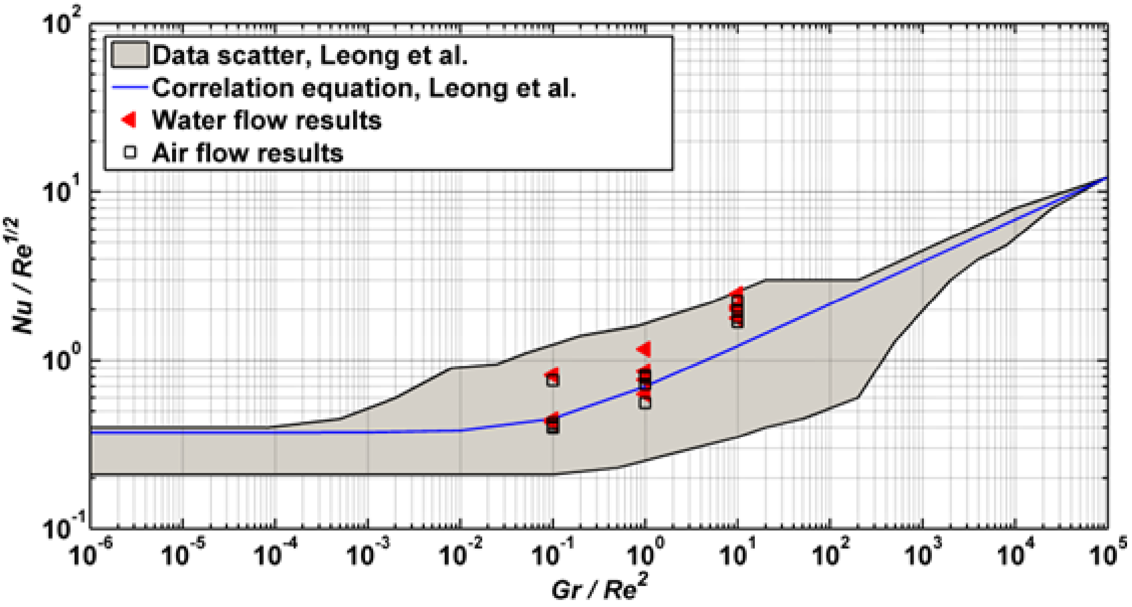

Figure 6.24: Heat transfer correlation of Leong et al. [9] for a cavity bottom heated wall.

Conclusions

The flow structure in a cubical open cavity located at the bottom of a horizontal square channel has been studied in the ranges of Reynolds and Richardson numbers $100 \leq Re \leq 1500$ and $0 \leq Ri \leq 10$, respectively. Air and water were used separately as working fluids. The bottom wall of the cavity was heated with uniform temperature.

Isothermal configuration, where no heat transfer occurs, was also analyzed in the same range of Reynolds number in order to detect the impacts of the mixed convection on the flow structure.

The effect of the temperature dependent fluid properties were studied numerically for the water flow for the considered range of Re and Ri. It was found that, the effect of the temperature dependent fluid properties does not affect the flow topology. Consequently, considering constant physical properties is acceptable. Also, the previous works use constant physical properties for the air flow in these ranges of Re and Ri for the same experimental condition used for water.

Several experiments with water were implemented to validate the numerical results. A good agreement has been found between experimental and numerical results especially for the heated wall configuration.

The flow is steady for the isothermal configuration when using both working fluids (air and water) at $Re \leq 1500$. While the flow becomes unsteady in the heated configuration at $Re=500$ with $Ri \geq 1$.

The phenomenological study shows the existence of a primary recirculation cell structure inside the cavity in all the cases, which is similar to the flow structures found in a lid driven cavity. For the mixed convection, it has been found that the effect of the buoyancy is very weak for low Richardson numbers in the range ($0.001 \leq Ri \leq 0.01$) for all $Re \leq 1500$, while at $Ri \geq 1$ the effect of the buoyancy is important.

- **Air flow conclusions**

For both low $Ri \leq 0.1$ and $Re \leq 1500$, the flow is laminar and steady. When $Ri \leq 0.1$ the buoyancy effect is weak. The flow becomes unsteady and complex for $Re \geq 500$ with $Ri \geq 1$. As the Ri is increased, the buoyancy forces become stronger and more effective. It enhances the recirculating flow. The heat transfer rate increases rapidly by increasing the value of Ri, while the mixed convection dominates the heat transfer mechanism.

The time average flow structure approach is used to study the unsteady flows. It was found that, the velocity components are increasing with Ri for the same value of Re. This is due to the enhancement of the main vortex by the mixed convection. In addition, the Nusselt number increases with Ri for each value of Re.

- **Water flow conclusions**

The effects of Re and Ri on the water flow are very similar to the air flow. Steady flow is found at small Ri ($Ri=0.1$) for the whole range of Reynolds numbers ($Re \leq 1500$), where the buoyancy is weak. At $Ri=1$ the flow is unsteady for $Re \geq 500$, where markable contributions of the buoyancy force in the mixed convection strongly affecting the flow. The unsteady flow shows periodic and turbulent patterns in the range of Reynolds numbers ($100 \leq Re \leq 1500$) and Richardson number ($10^{-3} \leq Ri \leq 10^{1}$).

A periodic flow pattern with a non-dimensional specific period ($t^{*}=7$) appears at $Re=100$ and $Ri=10$. In this case, alternate flow ejections from the cavity to the channel near the lateral walls while the flow enters from the channel to the cavity through the central part.

The turbulent regime is observed for Re≥500 and Ri=1 and 10. In these conditions, the natural convection dominates the heat transfer mechanism within the cavity. A conditional sampling technique was used to analyze the mean flow history of the unsteady flows for Re=1500. The results show four mean flow structures, which are periodically repeatable. The most probable structure consists of two symmetrically distributed flow ejections, from the cavity to the channel, near the lateral walls and a flow inrush at the center of the cavity. The other three structures have a similar probability of occurrence. One consists of a central flow ejection from the cavity and two symmetrically distributed flow inrushes. The other two structures have a single mean lateral flow ejection near a lateral wall.

The computed Nusselt numbers in the present three-dimensional setup are in general agreement with a previously reported correlation, valid for two-dimensional cavities of different aspects ratios.

Bibliography

[1] R. F. Weiss and B. H. Florsheim, "Flow in a Cavity at Low Reynolds Number," *Phys. Fluids*, vol. 8, no. 9, pp. 1631, 1965.

[2] O. R. Burggraf, "Analytical and Numerical Studies of the Structure of Steady Separated Flows," *J. Fluid Mech.*, vol. 24, no. 1, pp. 113-151, 1966.

[3] F. Pan and A. Acrivos, "Steady Flows in Rectangular Cavities," *J. Fluid Mech.*, vol. 28, no. 4, pp. 643-655, 1967.

[4] E. Papanicolaou and Y. Jaluria, "Mixed Convection From an Isolated Heat Source in a Rectangular Enclosure," *Numer. Heat Transf. Part A Appl.*, vol. 18, no. 4, pp. 427–461, 1991.

[5] O. Manca, S. Nardini, K. Khanafer, and K. Vafai, "Effect of Heated Wall Position on Mixed Convection in a Channel With an Open Cavity," *Numer. Heat Transf. Part A Appl.*, vol. 43, no. 3, pp. 259–282, 2003.

[6] E. Papanicolaou and Y. Jaluria, "Mixed Convection from a Localized Heat Source in a Cavity with Conducting Walls: a Numerical Study," *Numer. Heat Transf. Part A Appl.*, vol. 23, no. 4, pp. 463–484, 1993.

[7] H. Yao, R. K. Cooper, and S. Raghunathan, "Simulation of Three-dimensional Incompressible Cavity Flows," *ICAS 2000 Conf.*, pp. 1–8, 2000.

[8] O. Manca, S. Nardini, and K. Vafai, "Experimental Investigation of Opposing Mixed Convection in a Channel with an open Cavity Below," *Exp. Heat Transf.*, vol. 21, no. 2, pp. 99–114, 2008.

[9] J. C. Leong, N. M. Brown, and F. C. Lai, "Mixed Convection from an Open Cavity in a Horizontal Channel," *Int. Commun. Heat Mass Transf.*, vol. 32, no. 5, pp. 583–592, 2005.

[10] O. Manca, S. Nardini, and K. Vafai, "Experimental Investigation of Mixed Convection

in a Channel With an Open Cavity," *Exp. Heat Transf.*, vol. 19, no. 1, pp. 53–68, 2006.

[11] G. a. Brès and T. Colonius, "Three-dimensional Instabilities in Compressible Flow Over Open Cavities," *J. Fluid Mech.*, vol. 599, pp. 309–339, 2008.

[12] L. Carson, "Solar Energy," in *Australian Energy Resource Assessment: Chapter 10 Solar Energy*, AUSTRALI, pp. 261–284, 2014.

[13] G. Abdelmassih, S. Varela, A. Vernet, and J. Pallares, "DPIV Experimental Study of Mixed Convection in an Open Cavity," in *10th International Symposium on Particle Image Velocimetry -PIV13*, pp. 5–10, 2013.

[14] F. Zamzari, Z. Mehrez, A. El Cafsi, A. Belghith, and P. Le Quéré, "Entropy Generation and Mixed Convection in A Horizontal Channel with an Open Cavity," *Int. J. Exergy*, vol. 17, no. 2, pp. 219–239, 2015.

[15] F. Corvaro, M. Paroncini, and M. Sotte, "Experimental PIV and Interferometric Analysis of Natural Convection in a Square Enclosure with Partially Active Hot and Cold Walls," *Int. J. Therm. Sci.*, vol. 50, no. 9, pp. 1629–1638, 2011.

[16] G. Abdelmassih, A. Vernet, and J. Pallares, "Steady and Unsteady Mixed Convection Flow in a Cubical Open Cavity with the Bottom Wall Heated," *Int. J. Heat Mass Transf.*, vol. 101, pp. 682–691, 2016.

[17] G. Abdelmassih, a Vernet, and J. Pallares, "Numerical Simulation of Incompressible Laminar Flow in a Three-dimensional Channel with a Cubical Open Cavity with a Bottom Wall Heated," *J. Phys. Conf. Ser.*, vol. 395, pp. 012099–7, 2012.

[18] T.J. O'Hern; J.R. Torczynski; T.K. Blanchat; T.Y. Chu;, "Shear-Driven Flow in a Square Cavity: A Comparative Study Using PIV, LDV, and Computational Simulations," *Am. Soc. Mech. Eng. Fluids Eng. Div.*, vol. 191, pp. 135–142, 1994.

[19] P. M. R. Huerre, "Hydrodynamic Instabilities in Open Flows," *Cambridge Books Online*, 1998.

[20] J. C. Lin and D. Rockwell, "Organized Oscillations of Initially Turbulent Flow Past a Cavity," *AIAA J.*, vol. 39, no. 6, pp. 1139–1151, 2001.

[21] K. Chang, G. Constantinescu, and S. O. Park, "Analysis Of The Flow And Mass Transfer Processes for the Incompressible Flow Past an Open Cavity with a Laminar

and a Fully Turbulent Incoming Boundary Layer, ” *J. Fluid Mech.*, Vol 561, pp. 113-145, 2006.

[22] X. X. Li, R. E. Britter, and L. K. Norford, “Transport Processes in and above Two-dimensional Urban Street Canyons Under Different Stratification Conditions: Results from Numerical Simulation,” *Environ. Fluid Mech.*, vol. 15, no. 2, pp. 399–417, 2015.

[23] P. S. Zdanski, M. Ortega, and N. G. C. Fico, “Numerical Study of the Flow Over Shallow Cavities,” *Comput. Fluids*, vol. 32, no. 7, pp. 953–974, 2003.

[24] H. Yao, R. K. Cooper, and S. Raghunathan, “Numerical Simulation of Incompressible Laminar Flow over Three-Dimensional Rectangular Cavities,” *J. Fluids Eng.*, vol. 126, no. 6, pp. 919–927, 2004.

[25] T. M. Faure, P. Adrianos, F. Lusseyran, and L. Pastur, “Visualizations of the Flow Inside an Open Cavity at Medium Range Reynolds Numbers,” *Exp. Fluids*, vol. 42, no. 2, pp. 169–184, 2006.

[26] Y. Stiriba, “Analysis of the Flow and Heat Transfer Characteristics for Assisting Incompressible Laminar Flow Past an Open Cavity,” *Int. Commun. Heat Mass Transf.*, vol. 35, no. 8, pp. 901–907, 2008.

[27] Y. Stiriba, F. X. Grau, J. A. Ferré, and A. Vernet, “A Numerical Study of Three-Dimensional Laminar Mixed Convection Past an Open Cavity,” *Int. J. Heat Mass Transf.*, vol. 53, no. 21–22, pp. 4797–4808, 2010.

[28] J. Basley, L. R. Pastur, F. Lusseyran, T. M. Faure, and N. Delprat, “Experimental Investigation of Global Structures in an Incompressible Cavity Flow Using Time-Resolved PIV,” *Exp. Fluids*, vol. 50, no. 4, pp. 905–918, 2010.

[29] D. Ramakrishna, T. Basak, S. Roy, and I. Pop, “A Complete Heatline Analysis on Mixed Convection within a Square Cavity: Effects of Thermal Boundary Conditions via Thermal Aspect Ratio,” *Int. J. Therm. Sci.*, vol. 57, pp. 98–111, 2012.

[30] L. Pastur, Y. Fraigneau, F. Lusseyran, and J. Basley, “From Linear Stability Analysis to Three-dimensional Organisation in an Incompressible Open Cavity Flow,” *Phys. Fluids*, 2012.

[31] Y. Stiriba, J. A. Ferré, and F. X. Grau, “Heat Transfer and Fluid Flow Characteristics

of Laminar Flow Past an Open Cavity with Heating from Below," *Int. Commun. Heat Mass Transf.*, vol. 43, pp. 8–15, 2013.

[32] L. Valencia, J. Pallares, I. Cuesta, and F. X. Grau, "Rayleigh-Bénard Convection of Water in a Perfectly Conducting Cubical Cavity: Effects of Temperature-Dependent Physical Properties in Laminar and Turbulent Regimes," *Numer. Heat Transf. Part A Appl.*, vol. 47, no. 4, pp. 333–352, 2005.

[33] F. Zonta and A. Soldati, "Effect of Temperature Dependent Fluid Properties on Heat Transfer in Turbulent Mixed Convection," *J. Heat Transfer*, vol. 136, no. 2, pp. 022501–12, 2013.

[34] M. M. Rahman, H. F. Öztop, N. a. Rahim, R. Saidur, K. Al-Salem, N. Amin, M. a. H. Mamun, and a. Ahsan, "Computational Analysis of Mixed Convection in a Channel with a Cavity Heated from Different Sides," *Int. Commun. Heat Mass Transf.*, vol. 39, no. 1, pp. 78–84, 2012.

[35] S. M. Aminossadati and B. Ghasemi, "A Numerical Study of Mixed Convection in a Horizontal Channel with a Discrete Heat Source in an Open Cavity," *Eur. J. Mech. - B/Fluids*, vol. 28, no. 4, pp. 590–598, 2009.

[36] A. Pantokratoras, "Fully Developed Laminar Free Convection With Variable Thermophysical Properties Between Two Open-Ended Vertical Parallel Plates Heated Asymmetrically with Large Temperature Differences," *J. Heat Transfer*, vol. 128, no. 4, pp. 405-408, 2006.

[37] F. P. Incropera and D. P. DeWitt, Fundamental of Heat and Mass Transfer, "*Fifth edit*". 2001.

[38] P. H. Gaskell and A. K. C. Lau, "Curvature Compensated Convective Transport: SMART, a New Boundedness Preserving Transport Algorithm," *Int. J. Numer. Methods Fluids*, vol. 8, no. 6, pp. 617–641, 1988.

[39] H. K. Versteeg and W. Malalasekera, "An Introduction to Computational Fluid Dynamics - The Finite Volume Method ", First edit., 1995.

[40] R. J. Adrian, "Scattering Particle Characteristics and their Effect on Pulsed Laser Measurements of Fluid Flow: Speckle Velocimetry vs Particle Image Velocimetry,"

Appl. Opt., vol. 23, no. 11, pp.1690–1691, 1984.

[41] J. Westerweel, “Digital Particle Image Velocimetry - Theory and Application,” *Delft Delft Univ. Press*, 1993.

[42] J. Westerweel, “Optical Diagnostics in Fluid and Thermal Flow,” *Int. Soc. Optical Eng.*, SPIE-2005, pp. 624–635, 1993.

[43] J. Westerweel, “Fundamentals of Digital Particle Image Velocimetry,” *Meas. Sci. Technol.*, vol. 8, no. 12, pp. 1379–1392, 1997.

[44] J. Westerweel, A. A. Draad, J. G. T. Hoeven, and J. Oord, “Measurement of Fully-Developed Turbulent Pipe Flow with Digital Particle Image Velocimetry,” *Exp. Fluids*, vol. 20, no. 3, pp. 165-177, 1996.

[45] A. Lourens, “Measurement of Turbulent Scalar Mixing by Means of a Combination of PIV and LIF,” *Doctoral Thesis*, Delft University, 2002.

[46] R. J. Adrian, “Particle-Imaging Techniques for Experimental Fluid Mechanics,” *Annu. Rev. Fluid Mech.*, vol. 23, no. 1, pp. 261–304, 1991.

[47] R. D. Keane and R. J. Adrian, “Theory of Cross-Correlation Analysis of PIV Images,” *Appl. Sci. Res.*, vol. 49, no. 3, pp. 191–215, 1992.

[48] S. Varela, “Computational and Experimental Modeling of Fluid Flow and Heat Transfer Processes in Complex Geometries,” *Doctoral Thesis*, Rovira i Virgili University, 2012.

[49] N. Ertürk, “Particle Image Velocimetry Applications in Complex Flow Systems,” *Doctoral Thesis*, Rovira i Virgili University, 2012.

[50] G. Usera, A. Vernet, and J. A. Ferré, “Considerations and Improvements of the Analysing Algorithms used for Time Resolved PIV of Wall Bounded Flows,” *Proc. 12th Int. Symp. Appl. Laser Tech. to fluid Mech. Lisbon*, pp. 11–15, 2004.

[51] J. Nogueira, A. Lecuona, and P. A. Rodríguez, “Local Field Correction PIV: On the Increase of Accuracy of Digital PIV Systems,” *Exp. Fluids*, vol. 27, no. 2, pp. 107–116, 1999.

[52] J. Nogueira, A. Lecuona, and P. A. Rodríguez, “Local Field Correction PIV,

Implemented by Means of Simple Algorithms, and Multigrid Versions," *Meas. Sci. Technol.*, vol. 12, no. 11, pp. 1911–1921, 2001.

[53] S. Varela, I. Balagué, I. Sancho, N. Ertürk, M. Ferrando, and A. Vernet, "Functionalised Alginate Flow Seeding Microparticles for Use in Particle Image Velocimetry (PIV)," *J. Microencapsul.*, vol. 33, no. 2, pp. 153–161, 2016.

[54] J. Jeong and F. Hussain, "On the Identification of a Vortex," *J. Fluid Mech.*, vol. 285, no. 1, pp. 69–94, 1995.

[55] J. Pallares, A. Vernet, J. A. Ferré, and F. X. Grau, "Eduction of Near Wall Flow Structures Responsible for Large Deviations of the Momentum-Heat Transfer Analogy and Fluctuations of Wall Transfer Rates in Turbulent Channel Flow," *Comput. Fluids*, vol. 36, no. 8, pp. 1327–1334, 2007.

[56] J. Pallares, A. Vernet, J. A. Ferre, and F. X. Grau, "Turbulent Large-Scale Structures in Natural Convection Vertical Channel Flow," *Int. J. Heat Mass Transf.*, vol. 53, no. 19–20, pp. 4168–4175, 2010.